SOLUBILITY PRODUCT CONSTANTS FOR NATURAL DOLOMITE (0–200°C) THROUGH A GROUNDWATER-BASED APPROACH USING THE USGS PRODUCED WATER DATABASE

H.A. ROBERTSON*, H. CORLETT**, C. HOLLIS***, F.F. WHITAKER*

ABSTRACT. The calculation of a reliable temperature dependent dolomite solubility product constant (K_{sp-dol}) has been the subject of much research over the last 70 years. This study evaluates $\log_{10}({}^{a}Ca^{2+}/{}^{a}Mg^{2+})$ values using PHREEQC (Pitzer approach) for a screened subset (n=11,480) of formation waters in the U.S. Geological Survey National Produced Waters Geochemical Database V2 (PWGD), an extensive inventory of 165,960 formational waters from a range of sedimentary lithologies in North America up to 6.6 km depth (Blondes and others, 2016). Through extensive ground truthing against datasets sourced from Texas Gulf Coast basin and the Mississippi Salt Dome basin we establish both the geochemical data from the PWGD and a new geothermal model of the US that is used to determine temperatures at-formation-depth to be reliable data sources.

The vast majority (90%) of PWGD samples have $\log_{10}({}^{a}Ca^{2+}/{}^{a}Mg^{2+})$-temperature values that are interpreted to be indicative of calcite-dolomite equilibrium and buffering by the bulk mineral solubilities. Using statistical models with different parameterisations (different Maier-Kelly formulas, mixed-effects models with various random effects and linear models) $\log_{10}({}^{a}Ca^{2+}/{}^{a}Mg^{2+})$ values are regressed against the estimated at-formation-depth temperatures to determine K_{sp-dol} between 0–200°C. This process relies on the well constrained calcite solubility product constant (K_{sp-cal}).

Local effects that modify $\log_{10}({}^{a}Ca^{2+}/{}^{a}Mg^{2+})$ values are evaluated through the addition of random effects to the mixed model which both improves the statistical reliability of the K_{sp-dol} model and enables the determination of K_{sp-dol} values for local dolomite phases. The nature of these local effects is open to interpretation, but we suggest the primary influence on $\log_{10}({}^{a}Ca^{2+}/{}^{a}Mg^{2+})$ values is the stoichiometry of the dolomite phase systematically modifying $\log_{10}({}^{a}Ca^{2+}/{}^{a}Mg^{2+})$ values. We discount the influence on $\log_{10}({}^{a}Ca^{2+}/{}^{a}Mg^{2+})$ values of dolomite order, the solution ionic strength, equilibration with anhydrite and chlorite group minerals, illitization of smectite and albitization of feldspar.

For the dolomite solubility equation;

$$CaMg(CO_3)_{2\,(s)} \leftrightarrow {Ca^{2+}}_{(aq)} + {Mg^{2+}}_{(aq)} + 2{CO_3}^{2-}_{(aq)} \quad (1)$$

the mixed-effects model (model J23) chosen as most representative yields a pK_{sp-dol} ($\log_{10}K_{sp-dol}$);

$$pK_{sp\text{-}dol} = 1.47545 \times 10^{1} - 6.24959 \times 10^{-2} \cdot T(K) - 3.99350 \times 10^{3} \cdot \frac{1}{T(K)} \quad (2)$$

*University of Bristol, UK – *corresponding author:* fiona.whitaker@bristol.ac.uk
**Memorial University, Canada
*** University of Manchester, UK

We determine $pK_{sp^\circ-dol}$ to be -17.27±0.35 (25°C, 1 atm) which is close to prior estimates, including the most recent experimental value reported by Bénézeth and others, 2018 ($pK_{sp^\circ-dol}$ = -17.19±0.3) validating the groundwater regression analysis approach of this study.

INTRODUCTION

The solubility product constant (K_{sp}) is defined as 'the product of the ion activities raised to appropriate powers of an ionic solute in its saturated solution, expressed with due reference to the dissociation equilibria involved and the ions present' (McNaught, 1997). Ideally K_{sp} is determined analytically using a saturated solution under the temperature/pressure conditions for which the constant is desired (Hefter and Tomkins, 2003). However, even with high degrees of supersaturation, it has proved difficult to unequivocally precipitate well-ordered, stoichiometric dolomite near standard state conditions (25°C, 1 atm) that coincide with conditions near which significant volumes of dolomite formed (Land, 1998; Warren, 2000). This necessitates a K_{sp} extrapolation from higher temperatures, where equilibrium is achieved within the timescales of laboratory experiments, using a Maier-Kelley regression (Maier and Kelley, 1932). Whilst pragmatic, this approach suffers from increased uncertainty for conditions outside the experimental range. An alternative to the experimental method for determining K_{sp-dol} is the groundwater method, which assumes calcite-dolomite equilibrium has been attained based on the substantial residence times of subsurface fluids.

This study reviews the complexities in evaluating K_{sp-dol} and determines K_{sp-dol} using the groundwater method by evaluating $\log_{10}({}^{a}Ca^{2+}/{}^{a}Mg^{2+})$-temperature relationships for a subset (n=11,480) of fluids from the PWGD (Blondes and others, 2016). Temperatures at-formation-depth are estimated by interpolating and merging subsurface geothermal gradients from the SMU Heatflow database (Blackwell and others, 2011) and mean annual land surface temperatures across North America (Bechtel, 2015). The thermal conditions under which most sedimentary dolomites form overlap with the range of temperatures (0–200°C) for which this study proposes a K_{sp-dol} suggesting a wide applicability for this regression analysis. For a given temperature, a deviation in $\log_{10}({}^{a}Ca^{2+}/{}^{a}Mg^{2+})$ away from the average value is interpreted to reflect a variation in the composition of the equilibrium dolomite phase.

SUMMARY OF PAST WORK

The Ca-Mg-CO_2-H_2O-Calcite-Dolomite System

There are two dominant mechanisms through which dolomite forms. The first is primary precipitation from a dolomite-supersaturated fluid;

$$CaMg(CO_3)_{2\,(s)} \leftrightarrow Ca^{2+}{}_{(aq)} + Mg^{2+}{}_{(aq)} + 2{CO_3}^{2-}{}_{(aq)} \quad (3)$$

with the solubility product constant for dolomite;

$$K_{sp\text{-}dol} = ({}^{a}Ca^{2+})({}^{a}Mg^{2+})\left({}^{a}{CO_3}^{2-}\right)^2 \quad (4)$$

Primary dolomites are found cementing sandstone lithologies (Spötl and Pitman, 1998), in metamorphic rocks (Bucher and Grapes, 2011) and as dolocretes (Khalaf, 2007). In natural

systems primary dolomite is much less volumetrically significant than secondary (diagenetic) dolomite mostly found replacing limestones (Warren, 2000). Secondary dolomite forms via a dissolution-reprecipitation mechanism whereby a Mg-rich fluid enters a calcite bearing formation, calcite dissolves, the fluid becomes dolomite supersaturated and precipitates dolomite;

$$2CaCO_{3(s)} + Mg^{2+}{}_{(aq)} \leftrightarrow CaMg(CO_3)_{2(s)} + Ca^{2+}{}_{(aq)} \quad (5)$$

The molar ratio of dissolved calcite to precipitated dolomite is a function of both the (temperature dependent) solubility and stoichiometry/order of all equilibrium solid phases (including any common-ion effects), and the unbuffered original fluid composition (particularly with respect to ${}^{a}Ca^{2+}$, ${}^{a}Mg^{2+}$ and ${}^{a}CO_3{}^{2-}$). Calcite-dolomite equilibrium exists for given conditions at a unique $\log_{10}({}^{a}Ca^{2+}/{}^{a}Mg^{2+})$ value which is directly related to K_{sp-dol} through the relatively well-constrained K_{sp-cal}. Equation (5) can be rewritten as simultaneous solubility equations for the dissolution of dolomite (eq 3) and of calcite;

$$CaCO_{3(s)} \leftrightarrow Ca^{2+}{}_{(aq)} + 2CO_3{}^{2-}{}_{(aq)} \quad (6)$$

with the solubility product constant for calcite;

$$K_{sp\text{-}cal} = ({}^{a}Ca^{2+})({}^{a}CO_3{}^{2-}) \quad (7)$$

The equilibrium constant ($K_{sp\text{-}dz}$) of equation (5) can also be stated in terms of solubility constants;

$$\frac{K_{sp\text{-}dol}}{K_{sp\text{-}cal}{}^{2}} = \frac{{}^{a}Mg^{2+}}{{}^{a}Ca^{2+}} = K_{sp\text{-}dz} \quad (8)$$

which can be rearranged to determine pK_{sp-dol};

$$\log_{10} K_{sp\text{-}dol} = 2 \log_{10} K_{sp\text{-}cal} - \log_{10}\left(\frac{{}^{a}Ca^{2+}}{{}^{a}Mg^{2+}}\right) \quad (9)$$

Improvements in estimates of K_{sp-cal}, and to a lesser extent ion activity models, lead to progressive refinement of K_{sp-dol} models. For example, early work by Hsu (1963) estimated $pK_{sp°-dol}$ to be -16.69 using a $pK_{sp°-cal}$ of -8.29 (Garrels and Drever, 1952). Recalculating (supplementary table 1) the data from Hsu (1963) using a $pK_{sp°-cal}$ from SUPCRT92 (table 1; slop07.dat database - Johnson and others, 1992) of -8.48 results in a decrease of $pK_{sp°-dol}$ to -17.07. Sherman and Barak (2000) and Bénézeth and others (2018) both collate and recalculate K_{sp-dol} values using different reference thermodynamic data and these studies form the basis for our review (supplementary table 2). Utilising K_{sp-cal} to determine K_{sp-dol} from the perspective of calcite-dolomite equilibrium has been employed for both experimental studies (Rosenberg and Holland, 1964; Baker and Kastner, 1981; Morrow and others, 1994; Usdowski, 1994; see 'Solubility (experimental)' supplementary table 2) and groundwater studies (Hsu, 1963; Barnes and Back, 1964; Hyeong and Capuano, 2001; Vespasiano and others, 2014; Blasco and others, 2018; see 'Solubility (groundwater)' supplementary table 2).

Complicating matters, Möller and De Lucia (2020) argue that because calcite and dolomite dissolve and precipitate incongruently, then $\log_{10}({}^{a}Ca^{2+}/{}^{a}Mg^{2+})$ and by extension equation (9), cannot be used to determine the thermodynamic properties of either bulk mineral. Specifically Möller and De Lucia (2020) state that equilibrium is maintained with non-stoichiometric magnesian calcite and calcian dolomite surface phases;

$$2Ca_yMg_{1-y}CO_{3_{(s)}} + (2y - x)Mg^{2+}_{(aq)} \leftrightarrow Ca_xMg_{(2-x)}(CO_3)_{2_{(s)}} + (2y - x)Ca^{2+}_{(aq)} \quad (10)$$

such that the $pK_{sp\text{-}dol_x}$ for the non-stoichiometric dolomite surface phase is;

$$pK_{sp\text{-}dol_x} = 2\ pK_{sp\text{-}cal_y} - (2y - x)p\left(\frac{{}^{a}Ca^{2+}}{{}^{a}Mg^{2+}}\right) \quad (11)$$

Assuming that the composition of neither surface carbonate phase is known the use of a single value of $\log_{10}({}^{a}Ca^{2+}/{}^{a}Mg^{2+})$ generates an inherently non-unique solution. Bulk mineral calcite and dolomite compositions deviating from ideality, both with respect to stoichiometry and order, pose similar non-uniqueness problems. We review the current understanding of the potential bulk and surface mineral contributions to solution chemistry.

Dolomite Ordering and Stoichiometry

Ordering.—The crystallographic structure of ideal dolomite consists of alternating layers of covalently bonded Ca^{2+}, Mg^{2+} and CO_3^{2-} ions (fig. 1) (Gregg and others, 2015; Deelman, 2003 *and references therein*). The level of homogeneity within individual cation monolayers is described as the degree of substitutional order (s) for the dolomite phase, with unity representing total order (s = 1) and zero total disorder (s = 0). The different sizes and Coloumbic attraction profiles of Ca^{2+} and Mg^{2+} ions mean disordered locations of either ion result in thermodynamically unfavourable (lattice strain) tilting and rotation of carbonate anions (Althoff, 1977; Deelman, 2003; Antao and others, 2004).

There exists a dynamic equilibrium with cations constantly swapping locations with overall ordering remaining constant. This is the mean-field assumption (ordering parameter homogeneity across an infinite lattice) that is the basis of the Bragg-Williams model (Bragg and Williams, 1934; Chaikin and others, 1995) seminally applied to dolomite by Navrotsky and Loucks (1977). The Bragg-Williams model enables both thermodynamic and kinetic components of dolomite ordering to be considered. Order (s) is described by the relationship (Navrotsky and Loucks, 1977);

$$s = \tanh\left(\frac{T_c s}{T}\right) \quad (12)$$

where T_c is the critical temperature at which there is zero order.

Higher temperatures decrease the difference in the potential energy between any two sites and the locations of Ca^{2+} and Mg^{2+} ions tend towards randomness, with the probability of an ion occupying a lattice location proportional to stoichiometry. Disordering is therefore endothermic (positive ΔH_{dis}) and disorder increases up to the T_c (T_c = 1373K–1473K, Goldsmith and Heard, 1961; Luth, 2001; Antao and others, 2004) whereupon there is total disorder ($s \rightarrow 0$ as $T \rightarrow T_c$; fig. 2). The loss of XRD-peaks (lattice-plane reflections) 101,

015 and 021 at T_c is also interpreted to reflect a second-order phase change to very-high magnesium calcite (VHMC) associated with a space group transformation from $R\bar{3}$ (dolomite) to $R\bar{3}c$ (calcite) (Antao and others, 2004; Gregg and others, 2015). For a synthetic ideal dolomite with a T_c of 1473K (Goldsmith and Heard, 1961), Helgeson and others (1978) determined the enthalpy of complete disordering ($\Delta H^{\circ}_{\mathrm{dis}}$) at reference state conditions to be $12.25\mathrm{kJ\ mol^{-1}}$, whilst Navrotsky and others (1999) determine the average $\Delta H^{\circ}_{\mathrm{dis}}$ for a suite of dolomites (natural and synthetic) is even higher at $33 \pm 6\ \mathrm{kJ\ mol^{-1}}$. High enthalpies of disorder are thought to correlate to substantial increases in dolomite solubility (Helgeson and others, 1978).

Based on solutions to equation (12) derived by Chaikin and others (1995), for the Bragg-Williams model well-ordered dolomite ($s \geq 0.96$) is the most stable state at temperatures $\leq$ 500°C (fig. 2). Helgeson and others (1978) suggested the thermodynamics of natural dolomites, that have (metastable) cation disorder acquired at low-temperatures, could be approximated by extrapolating high-temperature measurements of disorder to reference state conditions. This model yields $pK_{sp^{\circ}-dol}$ values of -18.14 and -16.60 for the ordered and disordered dolomite phases respectively (supplementary table 2). Helgeson and others (1978) observed that prior estimates of $pK_{sp^{\circ}-dol}$ ranged from -16.4 to -19.3, though most were close to -17 (see supplementary table 2) and interpreted that this value corresponded to a partially ordered dolomite with an s of 0.7. The ordered, disordered and naturally-ordered ($s = 0.7$) dolomite phases from Helgeson and others (1978) are included in a number of thermodynamic databases valid between 0–300°C, particularly those derived from SLOP databases (Shock and Helgeson, 1988). Most thermodynamic datasets are in some way derived from the SLOP databases including EQ3/6 which is the source of many TOUGHREACT and PHREEQC compatible databases and slop07.dat which, in conjunction with SUPCRT92, generates the solubility data for the disordered and ordered dolomite phases used by this study (Wolery and others, 1990; Parkhurst and Appelo, 1999; Xu, 2008). The ordered, disordered and naturally-ordered dolomite phases have been extensively used in a variety of simulations (André and others, 2007; Whitaker and Xiao, 2010; Al-Helal and others, 2012; Gomez-Rivas and others, 2014; Blasco and others, 2017; Hirani and others, 2018; Benjakul and others, 2020).

The metastable naturally-ordered ($s = 0.7$) phase Helgeson and others (1978) interpreted to be "*probably typical of modern sedimentary dolomite"* is confusing. Most work on what is now considered to be 'modern' (Holocene) dolomite was conducted after Helgeson and others (1978) and pre-Holocene dolomites typically have an $s > 0.7$ (see below). The range of $K_{sp^{\circ}-dol}$ values referenced by Helgeson and others (1978) encompasses both experimental studies and groundwater studies; the groundwater studies are primarily comprised of samples from the Floridan aquifer which is not modern, being Eocene to Miocene in age (Hsu, 1963; Barnes and Back, 1964). We discuss the relationships between, and the complexity of, dolomite ordering and compositions arguing that the later is the most significant property influencing the solubility of (pre-Holocene) dolomites.

Holocene dolomites are found with an $s << 1$, though in many cases the $s > 0.7$. For a near surface sediment core Gregg and others (1992) determined through Rietveld analysis that the youngest, nearest surface, calcian (60–54% $CaCO_3$) dolomites had an s of 0.7 and s increased with depth to a maximum of 0.9 (30cm beneath the surface). Rietveld structural analysis iteratively refines a mineralogy to fit XRD data whilst, the simpler more commonly

applied technique of Goldsmith and Graf (1958) determines *s* using the ratio of the intensities of the $(10\bar{5})$ and (110) reflections. Fang and Xu (2019) account for variations in stoichiometry and suggest that evaluations made using the Goldsmith and Graf (1958) methodology underestimate the *s* for calcian dolomites finding Holocene dolomite *s* values to be mostly between 0.5 and 0.8.

Stoichiometric pre-Holocene dolomites are typically completely ordered (i.e. $s \sim 1$) and have, though not always (*see* Miser and others, 1987), homogenous microstructures observed by transmission electron microscopy (TEM) (Reeder and Wenk, 1983; Reeder, 1992; Reeder, 2000). Complete ordering is unsurprising as the thermodynamic drive for order at diagenetic temperatures (0 – 300°C) is high (Helgeson and others, 1978; Navrotsky and others, 1999). Where cation disorder is interpreted it is often associated with calcian dolomite compositions, though Fang and Xu (2019) conclude that, regardless of stoichiometry, a dolomite with an $s > 0.5$ will have a $(10\bar{5})$ diffraction peak in XRD analysis. This is supported by experimental evidence of a close correlation between cation disorder and calcian dolomite compositions (Kaczmarek and Thornton, 2017; Kell-Duivestein and others, 2019).

For pre-Holocene dolomites, from a wide variety of compositions, Pina and others (2020) observe all samples to have a $(10\bar{5})$ diffraction peak suggesting at a minimum all pre-Holocene dolomites have an $s > 0.5$, though they also note a range of disorder in stoichiometric dolomite. For Cretaceous calcian dolomites (~54.5 – 53.5% $CaCO_3$) Manche and Kaczmarek (2019) determine, using the Goldsmith and Graf (1958) technique, a high degree of disorder (mean of facies $0.43 < s < 0.56$; total range $0.32 < s < 0.84$). We argue that the calculated disorder for these calcian dolomites would likely increase if reanalysed using the Fang and Xu (2019) methodology and that significant cation disorder, defined as $s < 0.5$, resolves on short (Holocene) timescales regardless of stoichiometry.

Hyeong and Capuano (2001), Vespasiano and others (2014), and Blasco and others (2018) interpolate between the Helgeson and others (1978) ordered and disordered dolomite phases to determine the *s* value (and K_{sp-dol} value) for the equilibrium dolomite phase (supplementary table 2). All three studies interpret high levels of disorder; Hyeong and Capuano (2001) determine *s* to be 0.4, whilst reported thermodynamic properties suggest the dolomites in the studies of Vespasiano and others (2014) and Blasco and others (2018) are marginally more ordered. Respectively the dolomites sampled are interpreted to be Oligocene (Hyeong and Capuano, 2001), Mesozoic (Vespasiano and others, 2014), and Triassic-Upper Jurassic (Blasco and others, 2018) in age and these values, particularly that of Hyeong and Capuano (2001), do not appear to be consistent with the aforementioned interpretations of *s* values for pre-Holocene dolomites being typically > 0.5. Instead, we interpret that these dolomites, and the Floridian aquifer dolomite evaluated by Helgeson and others (1978), reflect equilibrium with a natural dolomite phase of an unknown *s*, though with a minimum value of 0.5, and a potentially non-stoichiometric composition.

Stoichiometry.— Many dolomites have microstructural heterogeneity (typically lamellar-like modulations with wavelengths ~100–200Å observed by TEM) and XRD signals that are attenuated and diffuse, and are interpreted to reflect the presence of lattice disorder (Gregg and others, 1992; Navrotsky and others, 1999; Gregg and others, 2015). The degree of this

apparent disorder and microstructural heterogeneity is most significant in calcian dolomites albeit with unique signatures respectively for Holocene and pre-Holocene suggesting that some level of disorder resolves during short timescales (Reeder, 1992; Reeder, 2000). In contrast, although also metastable, calcian dolomite is present throughout the Phanerozoic (Lumsden and Chimahusky, 1980, Sperber and others, 1984).

The full range of natural dolomite stoichiometries is limited ($Ca_{1.16}Mg_{0.84}(CO_3)_2$ – $Ca_{0.96}Mg_{1.04}(CO_3)_2$; Land, 1985) and bimodally distributed (fig. 3) with the largest mode centred on ideality and a smaller mode at 54 – 56% $CaCO_3$ (Lumsden and Chimahusky, 1980; Sperber and others, 1984; Reeder, 2000; Deelman, 2003). To account for the overall mineral stoichiometry the presence of proportionally small, high-Ca zones within a stoichiometric well ordered ABABAB... (alternating (A) Ca and (B) Mg monolayers) dolomite lattice has long been interpreted (Van Tendeloo and others, 1985) and more recently observed (Fang and Xu, 2018). There are two competing theories surrounding the exact structural incorporation of (excess) Ca into dolomite;

1) Ca is hosted in an ordered, dolomite-like, structure consisting of either variations in the sequence of basal cation layers (otherwise known as stacking disorder, stacking faults or mixed-layer effects) or mixed cation (Ca:Mg 1:1) monolayers (Reeder, 2000; Deelman, 2003 *and references therein*). Both structures destroy $R\bar{3}$ symmetry but computer simulations favor stacking disorder (Wright and others, 2002). For the regular ABABAB... dolomite lattice structure the main proposed stacking disorder is the δ structure ABAAABA... with the Ca:Mg ratio for the unit cell rising from 1:1 to 2:1 (Van Tendeloo and others, 1985; Reeder, 1992).

2) For an Ordovician Ca-rich (55% $CaCO_3$) dolomite Fang and Xu (2018) observe TEM modulations to be comprised of alternating thick, well ordered (s = 0.9) stoichiometric dolomite, and thin, Ca-rich, zones. However, whilst Fang and Xu (2018) do not fully resolve the crystallographic structure, they characterise these Ca-rich zones as Mg-calcite nanoprecipitates as they lack apparent order. Shen and others (2013) propose Mg-calcite nanoprecipitates in dolomite form through exsolution of separate lamellae of Mg-calcite and stoichiometric ordered dolomite. However, substantial solid state lattice diffusion generating exsolution lamellae typically only occurs during high-temperature cooling as it obeys a temperature-dependent exponential kinetic rate function; for example, pyroxene exsolution occurs at ~800 − 1000°C (Bragg and Williams, 1934; Grove, 1982). At diagenetic temperatures (< 300°C) solid state lattice reordering is by far the slowest mechanism through which dolomite could achieve a more ordered state, with recrystallization (fastest) and surface diffusion (slightly slower) operating several orders of magnitude faster (Usdowski, 1994) suggesting that the Ca-rich zones form aqueously.

Small Ca-rich zones not only significantly affect XRD and TEM signals, so generating misleading estimates of s, but also cause lattice strain modifying solubility (Chai and others, 1995). The transition from stoichiometric to calcian dolomite is energetic; for example a 56% $CaCO_3$ dolomite requires a ΔH_f° of 15kJ mol^{-1}(Chai and others, 1995) which is of a similar magnitude to the enthalpy change associated with disorder (Helgeson and others, 1978; Navrotsky and others, 1999). Comparatively the ΔH_f° of incorporating 6% $MgCO_3$ into calcite is only 1.2kJ mol^{-1} (Navrotsky and Capobianco, 1987).

Metastability summary.— In the context of an Ostwald-step model the overall reaction of the precipitation of stoichiometric ordered dolomite remains equation (3), but metastable and increasingly insoluble intermediary phases provide a catalytic pathway (Nordeng and Sibley, 1994; Kaczmarek and Sibley, 2007). A wide variety of intermediary metastable phases are suggested, including magnesite (Chou and others, 1989; Sherman and Barak, 2000), amorphous phases (Kaczmarek and Sibley, 2007; Rodriguez-Blanco and others, 2015), VHMC (Gregg and others, 2015), protodolomite (Graf and Goldsmith, 1956) and calcian/disordered dolomite (Goldsmith, 1983; Reeder, 1992; Kaczmarek and Sibley, 2007; Kaczmarek and Thornton, 2017; Kell-Duivestein and others, 2019). Of these calcian dolomite is the most stable and therefore potentially consequential to natural subsurface dolomite thermodynamics.

The concept of dolomite metastabilty was incorporated by Graf and Goldsmith (1956) into their definition of protodolomite; 'single phase rhombohedral carbonates which deviate from the composition of the dolomite that is stable in a given environment, or are imperfectly ordered, or both, but which would transform to dolomite if equilibrium were established'. Protodolomite is commonly used to describe Holocene dolomites with significant cation disorder, though Land (1980) and Gregg and others (2015) reject the term 'protodolomite' on the basis that any phase without order is not considered dolomite. Instead, they define rhombohedral Ca–Mg carbonates with near-dolomite stoichiometry, but lacking cation ordering, as VHMC. Dolomite in contrast must have (XRD) evidence of 'ordering reflections' (Bradley and others, 1953; Graf and Goldsmith, 1956) that cannot occur in the $R\bar{3}c$ space group.

For pre-Holocene dolomites, the vast majority of which have ordering reflections, the present dolomite definition arguably focuses too narrowly on order. Gregg and others (2015) permit a dolomite to have a 'near-dolomite stoichiometry' continuum, stemming from Land (1980)'s assertion that *'Ideal, stoichiometric dolomite is the exception, not the rule'*. This statement conflicts with the observation that the modal natural dolomite composition is stoichiometric (fig. 3). Undoubtedly there is complexity in the relationship between cation ordering and stoichiometry but for the purposes of this study we consider natural pre-Holocene dolomite to either be stoichiometric (and well-ordered) or calcian (with an indeterminate, though probably high, level of cation order).

Calcite Stoichiometry

The incorporation of a variable amount of Mg into the calcite structure is typically described as a non-ideal solid solution between the $CaCO_3$ and $MgCO_3$ end-members (see Deelman (2003) for an alternative mixed crystal theory). The dissolution of $MgCO_3$;

$$\mathrm{MgCO_{3(s)}} \leftrightarrow \mathrm{Mg^{2+}_{(aq)}} + \mathrm{2CO_3^{2-}_{(aq)}} \tag{13}$$

has the solubility product constant;

$$\mathrm{K_{sp\text{-}mag}} = (\,{}^{a}\mathrm{Mg^{2+}})(\,{}^{a}\mathrm{CO_3^{2-}}) \tag{14}$$

where $pK_{sp°-mag} = -8.035$ (table 1). The dissolution of an arbitrary non-stoichiometric calcite ($Ca_xMg_{(1-x)}CO_3$) is described as;

$$\mathrm{Ca_xMg_{(1-x)}CO_{3(s)}} \leftrightarrow (1-x)\mathrm{Ca^{2+}_{(aq)}} + x\mathrm{Mg^{2+}_{(aq)}} + \mathrm{CO_3^{2-}_{(aq)}} \tag{135}$$

with the solubility product constant;

$$K_{sp-cal(x)} = {}^{a(1-x)}Ca^{2+}{}_{(aq)}\ {}^{ax}Mg^{2+}{}_{(aq)}\ {}^{a}CO_3{}^{2-}{}_{(aq)} \quad (16)$$

For any value of x, equation (16) can be satisfied by many different combinations of ${}^{a}Ca^{2+}$, ${}^{a}Mg^{2+}$ and ${}^{a}CO_3^{2-}$ such that any saturated solution fulfilling equation (16) is said to be at stoichiometric saturation (see Lippmann, 1977; Gresens, 1981a; Gresens, 1981b; Gamsjäger and others, 2000). However metastable or stable thermodynamic equilibrium only occurs at a singular ${}^{a}Ca^{2+}$:${}^{a}Mg^{2+}$:${}^{a}CO_3^{2-}$ ratio and when there is thermodynamic equilibrium between every component (end-member) in every phase. The solubility of Mg-calcite solid solutions of varying compositions was first evaluated by Thorstenson and Plummer (1977) through a reinterpretation of the Mg-calcite solubility data of Plummer and Mackenzie (1974); this reinterpretation was notably critiqued by Gresens (1981a) for generating too great a range in equilibrium ${}^{a}Ca^{2+}/{}^{a}Mg^{2+}$ values. The use of the erroneously reinterpreted data from Thorstenson and Plummer (1977) by Möller and De Lucia (2020) is detrimental to their critique of Bénézeth and others (2018) (see below). For reference the solubility of non-ideal solid solutions, such as Mg-calcite, is now estimated using Equal-G methods developed by Lippmann (1980) and Königsberger and Gamsjäger (1992).

Mg-calcite is either described as low-Mg calcite (LMC ~ 1–4% - $MgCO_3$ though commonly around 2%), high-Mg calcite (HMC 4–30% $MgCO_3$) or, typically observed only during experimental synthesis, very high-Mg calcite (VHMC ~ 30 to 51 % $MgCO_3$ including dolomitic calcite ~ 50% $MgCO_3$), and huntitic calcite (75% $MgCO_3$) compositions (Gregg and others, 2015; Möller and De Lucia, 2020). HMC, in contrast to LMC, is only produced by biogenic processes and is poorly preserved, commonly undergoing recrystallisation to LMC (Bischoff and others, 1993). HMC typically loses ≥ 50% of the initial Mg content within a relatively short time ($10^1 - 10^4$ years; Dickson, 1995 *and references therein*). Thus, the vast majority of subsurface lithologies that contain calcite, are likely to be primarily composed of LMC, and typically we consider pure calcite a good approximation for LMC. However in the discussion we do evaluate the effect of LMC on calcite-dolomite equilibrium $\log_{10}({}^{a}Ca^{2+}/{}^{a}Mg^{2+})$ values; specifically we assume LMC to be an ideal solid solution as the difference between calcite and magnesite solubility is small, LMC compositions are close to the calcite end-member, and the difference between non-ideal and ideal solid solutions decreases as the composition tends towards an end-member (Königsberger and Gamsjäger, 1992). For the ideal solid solution model equation (16) reduces to;

$$pK_{sp\text{-}cal(x)} = (1-x)pK_{sp\text{-}cal} + x\ pK_{sp\text{-}mag} \quad (17)$$

Surface Complexities

The dissolution of Mg-calcite should be incongruent; the more soluble magnesite end-member is predicted to dissolve first until no Mg remains whereupon pure calcite dissolves. Due to slow ionic lattice diffusion this does not occur, and instead both $[Ca^{2+}]$ and $[Mg^{2+}]$ increase suggesting that calcite and magnesite end-members dissolve congruently. This

phenomena of non-equilibrium apparent congruent dissolution is described by two competing models (Gresens, 1981a);

1) Congruent dissolution; the solid solution dissolves congruently, behaving as a pure one component phase of a fixed stoichiometry. The point at which no further dissolution occurs is known as stoichiometric saturation (which may or may not also be thermodynamic equilibrium).

2) Incongruent dissolution; a thermodynamic equilibrium between the bulk and solution is maintained by an intermediary surface coating of incongruent dissolution products. This model is favoured by Möller and De Lucia (2020) for the dissolution of both Mg-calcite and dolomite.

The experiments of Möller (1973), reinterpreted by Möller and De Lucia (2020), involved monitoring (^{45}Ca) Mg-absorption on a calcite surface in a calcite saturated variable-$MgCl_2$ solution. In response to the addition of $MgCl_2$, the $\log_{10}({}^{a}Ca^{2+}/{}^{a}Mg^{2+})$ decreases and the Mg content of the surface phase increases linearly across a range of Mg-calcite compositions ($0 < x < 50\%$ $MgCO_3$). This suggests that the surface can buffer $\log_{10}({}^{a}Ca^{2+}/{}^{a}Mg^{2+})$ values. However, across a wide range of low $\log_{10}({}^{a}Ca^{2+}/{}^{a}Mg^{2+})$ values surface compositions were discrete, being either dolomitic calcite (50% $MgCO_3$) or huntitic calcite (75% $MgCO_3$). This indicates that the $\log_{10}({}^{a}Ca^{2+}/{}^{a}Mg^{2+})$ buffering capacity is limited by both the thickness of the reactive surface layer and by the compositional constraints of the surface Mg-calcite phases.

There are outstanding questions surrounding the interplay between bulk mineral composition, reactive surface layers, and the solution during times of significant mass transfer between phases. These relationships have been extensively explored for LMC (Sinclair, 2011; Sinclair and others, 2012). At one extreme, if the entire bulk mineral completely dissolves in a closed system $[Ca^{2+}]/[Mg^{2+}]$ (and the $\log_{10}({}^{a}Ca^{2+}/{}^{a}Mg^{2+})$ value) equals the bulk mineral [Ca]/[Mg]. As mass transfers between phases increase, it seems reasonable to conclude that 1) $\log_{10}({}^{a}Ca^{2+}/{}^{a}Mg^{2+})$ values will increasingly reflect equilibrium with the bulk composition and 2) the composition of the thin surface phases will respond (irrelevantly) to the solution $\log_{10}({}^{a}Ca^{2+}/{}^{a}Mg^{2+})$ value maintaining a role as a catalytic intermediary phase.

Möller and De Lucia (2020) suggest that the Möller (1973) $\log_{10}({}^{a}Ca^{2+}/{}^{a}Mg^{2+})$ value in equilibrium with a dolomitic-composition surface phase on bulk calcite is the *same* as the $\log_{10}({}^{a}Ca^{2+}/{}^{a}Mg^{2+})$ value determined to reflect equilibrium with the Bénézeth and others (2018) dolomite phase (fig. 4a). Möller and De Lucia (2020) use this to argue that the determination of dolomite solubility is impossible by classic experimental methods. However the two values are not the same; specifically the $\log_{10}({}^{a}Ca^{2+}/{}^{a}Mg^{2+})$ values for the Bénézeth and others (2018) dolomite phase at 25°C in 0.1M NaCl and the maximum value observed by Möller (1973) for a dolomitic surface composition (49.5–50.5% $CaCO_3$) are -0.01 and -0.30 respectively (fig. 4a). These values appear to be of a similar order of magnitude as Möller and De Lucia (2020) compare to the (erroneous) Thorstenson and Plummer (1977) data.

Equilibration with the Mg-calcite surface phase may be of greater significance to K_{sp-dol} measurements when mass transfers between the bulk and solution are low. Surface phases could therefore be more consequential for experimental, rather than groundwater,

K_{sp-dol} methods due to sluggish kinetics. Using XPS data Bénézeth and others (2018) confirmed the surface dolomite precipitate to have near ideal dolomite stoichiometry, similar to the bulk. However, in contrast to XRD data, XPS does not give information on order and thus whether the surface phase is dolomite, and not VHMC, is equivocal.

Möller and De Lucia (2020) argue that the surface phases of calcite or dolomite are Mg-rich compared to the bulk since Mg^{2+} is more strongly bound to the surface than Ca^{2+}. With respect to the experiments of Plummer and Mackenzie (1974) where biogenic calcite consisting of an average bulk $HMC_{(18.4\%MgCO_3)}$ transitions to $HMC_{(11.7\%MgCO_3)}$ (fig. 4b) Möller and De Lucia (2020) interpret the end state solution with a $\log_{10}({}^{a}Ca^{2+}/{}^{a}Mg^{2+}) = 0.95$ is in equilibrium only with a $HMC_{(30\%MgCO_3)}$ surface phase and that $\log_{10}({}^{a}Ca^{2+}/{}^{a}Mg^{2+})$ values cannot be used to identify bulk carbonate compositions. There appear to be two problems with this interpretation, which Möller and De Lucia (2020) state has wide implications for determining carbonate solubility;

1-Solution non-uniqueness.— The interpretation by Plummer and Mackenzie (1974) that the calcite composition initially dissolving is $HMC_{(23.8\%MgCO_3)}$ and the end stage precipitating phase is $HMC_{(11.7\%MgCO_3)}$ derives from modelling the rates of change of $[Ca^{2+}]$ and $[Mg^{2+}]$. Without this temporal data analysis, we agree the single $\log_{10}({}^{a}Ca^{2+}/{}^{a}Mg^{2+})$ value of 0.95 could not be used to identify either the $HMC_{(23.8\%MgCO_3)}$ *or* $HMC_{(11.7\%MgCO_3)}$ compositions as this represents a non-unique solution. Supporting the interpretation of Plummer and Mackenzie (1974) that $\log_{10}({}^{a}Ca^{2+}/{}^{a}Mg^{2+})$ values can be directly correlated to the composition of the bulk phase, spot EMPA/XRD determined compositions of unreacted and reacted carbonate grains correspond well to the estimated $HMC_{(23.8\%MgCO_3)}$ and $HMC_{(11.7\%MgCO_3)}$ phases (Plummer and Mackenzie, 1974).

Assuming a steady state reaction between the $HMC_{(23.8\%MgCO_3)}$ and $HMC_{(11.7\%MgCO_3)}$ phases a mass balanced solution can fix $[Ca^{2+}]/[Mg^{2+}]$, and $\log_{10}({}^{a}Ca^{2+}/{}^{a}Mg^{2+})$ values in early reaction stages where activities approximate concentrations, to 0.95;

$$a\mathrm{Ca_{0.762}Mg_{0.238}CO_3} \leftrightarrow b\mathrm{Ca_{0.883}Mg_{0.117}CO_3} + c\mathrm{Ca^{2+}} + d\mathrm{Mg^{2+}} + e\mathrm{CO_3^{2-}};\ \frac{c}{d} = 0.95 \quad (18)$$

which results in a solution for e = 1 of a = 3.27, b = 2.27, c = 0.49 and d = 0.51.

2- Observations of Mg-fractionation into the solution phase.— Multiple measurements of the Mg partition coefficient (Kd_{Mg}) for Mg-calcite during both dissolution or precipitation find Mg heavily fractionates into solution ($Kd_{Mg} \sim 0.014 - 0.06$; Huang and Fairchild, 2001 *and references therein*). Such extreme fractionation is consistent with the incongruent precipitation of a nearly pure calcite early in the Plummer and Mackenzie (1974) experiment. The final incongruent steady state $HMC_{(11.7\%MgCO_3)}$ precipitate that accounts for the bulk of the mass transfer results from the increasing ${}^{a}Mg^{2+}$ in the closed system. Möller and De Lucia's (2020) suggestion of a thin $HMC_{(30\%MgCO_3)}$ intermediary phase seems at odds with these Mg fractionation observations, though can be reconciled through mineral surface processes including electrostatic interactions.

The surface buffering capacity of $\log_{10}({}^{a}Ca^{2+}/{}^{a}Mg^{2+})$ not only reflect changes in the surface monolayer composition but also changes in the electrical double layer. The surface potential derives from 'potential determining ions' (PDIs). PDIs are absorbed dehydrated ions with adjacent vacancies caused by preferential dissolution of surrounding ions, adsorbed hydrated surface complexes, and adsorbed charged ions (Prédali and Cases, 1973; Derkani and others, 2019). The surface potential is notably sensitive to;

1) Changes in background ionic strength (*I*). The accumulation of 'indifferent' ions such as Na^{+} and Cl^{-} in the electric double layer leads to effective electrostatic screening, such that the zeta potential tends towards zero with increasing *I* (Strand and others, 2006; Derkani and others, 2019). As such at high *I* surface absorption/adsorption would be increasingly irrelevant in buffering $\log_{10}({}^{a}Ca^{2+}/{}^{a}Mg^{2+})$. As the Möller (1973) experiment only evaluates equilibrium using distilled water, we suggest the purported $\left(\frac{Ca}{Mg}\right)_{surface} - \left(\frac{Ca}{Mg}\right)_{solution}$ relationship maybe extremely sensitive to changes in *I*.

2) The bulk crystal composition. Ca^{2+} and Mg^{2+} are interpreted as PDIs for calcite whilst they are probably not PDIs for dolomite (see Derkani and others (2019) *and references therein*). This suggests that the dolomite surface has no potential to buffer $\log_{10}({}^{a}Ca^{2+}/{}^{a}Mg^{2+})$ through adsorption/absorption and that only recrystallisation (or ion-exchange with the monolayer) can modify $\log_{10}({}^{a}Ca^{2+}/{}^{a}Mg^{2+})$.

During early stages of dolomite dissolution there is an initial spike in $\log_{10}({}^{a}Ca^{2+}/{}^{a}Mg^{2+})$ and thus, the rate limiting step is interpreted to be the dissolution of Mg-surface complexes (Pokrovsky and Schott, 2001; Gautelier and others, 2007). This is likely to also be the case for (Mg-)calcite even though calcite dissolution kinetics are less well constrained (Pokrovsky and others, 2009). The reason for the lower solubility of Mg-surface complexes is interpreted to be the larger enthalpy of hydration for Mg^{2+} relative to Ca^{2+} (Busenberg and Plummer, 1982; Pokrovsky and Schott, 2001; Gautelier and others, 2007). However, for dolomite immediately after the initial release of Ca^{2+}, steady state quickly establishes and the overall dissolution and equilibrium $\log_{10}({}^{a}Ca^{2+}/{}^{a}Mg^{2+})$ values appear to reflect congruent dissolution of stoichiometric dolomite, and the surface [Ca]/[Mg] remains broadly constant (Pokrovsky and Schott, 2001). This assertion of a constant surface [Ca]/[Mg] is critiqued by Möller and De Lucia (2020) who argue that the Pokrovsky and Schott (2001) XPS measurements sample 20 – 25 layers whilst the Möller (1973) Ca^{45} measurements record compositional variation in a single monolayer, albeit of Mg-calcite (Möller and Sastri, 1974; Möller and De Lucia, 2020). As mixed cation layers are not found in dolomite the surface mechanism for buffering $\log_{10}({}^{a}Ca^{2+}/{}^{a}Mg^{2+})$ is likely to be different to a mixed cation calcite surface. We acknowledge calcite surfaces may have potential to buffer $\log_{10}({}^{a}Ca^{2+}/{}^{a}Mg^{2+})$ though suggest this is mitigated by significant mass transfers. We support the view of Pokrovsky and Schott (2001) that dolomite dissolution is congruent and surface compositions are comparable to the bulk.

Möller and De Lucia (2020) interpret that equilibrium with a wide variety of differently composed Mg-calcite surface phases has resulted in the scattered range of $\log_{10}({}^{a}Ca^{2+}/{}^{a}Mg^{2+})$ values in their meta-analysis (n=242) of groundwaters. This study

adopts a similar big data approach and focusses intensely on scatter to evaluate whether surface phases or bulk compositions are buffering $\log_{10}({}^{a}Ca^{2+}/{}^{a}Mg^{2+})$.

Determination of $K_{sp\text{-}dol}$

There are two contrasting approaches to calculating K_{sp-dol};

1) Indirectly determining K_{sp-dol} by combining free energies of ions and compounds (fig. 5a; see 'Thermal decomposition\Database' in supplementary table 2). For example reaction enthalpies (e.g. dolomite-pyroxene equilibria at 700°C from Chai and Navrotsky, 1993) can be extrapolated to lower T/P conditions and combined with other data, such as ionisation/hydration enthalpies for Ca^{2+} and Mg^{2+}, to determine K_{sp-dol}. Similarly, refinements to the mineral data (Holland and Powell, 1990; Holland and Powell, 1998) and aqueous models (Miron and others, 2017) can lead to updates to K_{sp-dol} models.

2) Direct experimental determination of K_{sp-dol} in aqueous solutions near conditions of interest is thought to be comparatively more accurate and applicable than the indirect approach (Hefter and Tomkins, 2003). Experimental solubility observations are ideally made over a wide temperature range and determined from both conditions of undersaturation via dissolution and supersaturation *via* precipitation so demonstrating thermodynamic reversibility. Unfortunately sluggish kinetics inhibit the attainment of equilibrium, particularly via precipitation, at lower temperatures (< 50°C) within reasonable experimental time frames (< 10 years) (Gregg and others, 2015).

The groundwater approach assumes that the residence time of subsurface fluids is sufficient for the attainment of calcite-dolomite equilibrium enabling a direct determination of K_{sp-dol} over a wide temperature range (fig. 5a; see 'Solubility (groundwater)' in supplementary table 2). We further review the direct experimental and groundwater methods for deriving K_{sp-dol} below.

Solubility.— A secondary effect of determining the temperature dependence of the solubility product using a (Maier-Kelley) regression is that the difference between the undersaturation and supersaturation approaches is averaged. This is termed the quasi-static method, and the smaller the difference between the two approaches the more precise the measurement (Hefter and Tomkins, 2003). Most experimental estimates of pK_{sp-dol} are based only on approaching equilibrium from conditions of undersaturation because of the difficulty in precipitating *unequivocally* ordered stoichiometric dolomite on realistic experimental timescales, particularly at lower temperatures.

Dolomite equilibrium has been measured at 80°C by Gautelier and others (2007) and at 53°C by Bénézeth and others (2018). However, Gautelier and others (2007) only evaluate equilibrium via dissolution, and there remains uncertainty (see Möller and De Lucia, 2020) around the composition of the precipitated phase in Bénézeth and others (2018). Bénézeth and others (2018) suggest that, aside from Gautelier and others (2007) at 80°C, no other single-phase (dolomite-only) experimentally derived values for K_{sp-dol} have been reported for temperatures > 25°C. However this ignores the work of Rosenberg and Holland (1964), Baker and Kastner (1981), Morrow and others (1994), and Usdowski (1994) (fig. 5a; see 'Solubility (experimental)' in supplementary table 2) who determined K_{sp-dol} by evaluating

calcite-dolomite equilibrium (60 – 420°C) in $CaCl_2$-$MgCl_2$ solutions. These studies unequivocally (XRD) precipitated ordered dolomite from a calcite seed.

Groundwater.—The groundwater approach presents an opportunity to 1) evaluate K_{sp-dol} at near-equilibrium conditions due to long residence times and 2) understand natural variations in calcite-dolomite equilibrium. However, whilst in an experiment both the solute and solvent can be analysed, for the groundwater approach these parameters are often less well-constrained. Nevertheless most prior studies applying the groundwater approach (Hsu, 1963; Barnes and Back, 1964; Hyeong and Capuano, 2001; Vespasiano and others, 2014; Blasco and others, 2018) are site specific and establish *a priori* the presence of both calcite and dolomite in host aquifers (fig. 5a; see 'Solubility (groundwater)' supplementary table 2). This contrasts with the big data approaches of Möller and De Lucia (2020) and this study that seek to interpret the presence of calcite-dolomite equilibrium from $\log_{10}({}^{a}Ca^{2+}/{}^{a}Mg^{2+})$-temperature relationships alone.

Defining K_{sp-dol} assuming the system is only-dolomite buffered (eq 4) is complicated by sample degassing and/or equilibration with atmospheric CO_2 which compromises the quality of pH and HCO_3^- measurements (Hyeong and Capuano, 2001). The primary advantage of assuming calcite-dolomite equilibrium (eq 8) is the independence from pCO_2 and pH measurements (Hyeong and Capuano, 2001). Comparing approaches we note a two order of magnitude difference in the estimated K_{sp-dol} (supplementary table 1). Moreover, by multiplying the activities for the dolomite-only system (eq 4) the errors on each term are cumulated, whereas if calcite-dolomite equilibrium (eq 8) is assumed the errors on each term are reduced and compensatory (Hsu, 1963).

Through regression analysis we interpret that bulk calcite-dolomite equilibrium is extremely common in subsurface fluids and evaluate K_{sp-dol}. Variations in $\log_{10}({}^{a}Ca^{2+}/{}^{a}Mg^{2+})$-temperature relationships are speculated to relate primarily to the composition of the equilibrium dolomite phase.

METHODOLOGY

To evaluate the dolomitizing potential of subsurface fluids, geochemical data is sourced from the U.S. Geological Survey National Produced Waters Geochemical Database V2 (PWGD; Blondes and others, 2016). This is an extensive database of formation waters from a range of sedimentary lithologies across North America to a maximum 6.6 km depth. The PWGD has previously been used for a variety of purposes including investigating the potability of produced water (Aines and others, 2011), hydrogeological analysis of formational fluids (Engle and Blondes, 2014), and mineral exploration (Ray, 2016).

The PWGD dataset of 165,960 waters is filtered using a set of criteria (supplementary table 3) adapted from Hitchon and Brulotte (1994) and Blondes and others (2016), leading to the rejection of 93% of samples. The remaining 11,846 samples are categorized into 5 lithological groups; Sandstone, Dolomite, Limestone, Mixed Carbonate and Shale (supplementary table 4).

The PWGD includes the temperature at which the pH was recorded, albeit very rarely (3% of samples with an average of 24°C) and we set this temperature to 25°C if not provided. Of more critical importance the PWGD lacks data on temperatures at-formation-depth. Similar to Shope and others (2012) at-formation-depth temperatures are calculated from

sample depth measurements (PWGD) using the corrected geothermal gradients (SMUH) and the mean annual surface temperature.

We use the Southern Methodist University Heat Flow (SMUH) database to estimate temperature at-formation-depth. This database contains both geothermal observations and calculated thermal gradients for 99,044 records (fig. 6b) of drilled wells across North America (Blackwell and others, 2011). The database is filtered to include only records that have bottom hole temperature-Harrison correction (BHT-Harrison) geothermal gradients between 0°C/km and 200°C/km (Harrison and others, 1983). Geothermal gradients are down-sampled to 0.1°x0.1° Lat/Long areas then interpolated (SciPy griddata linear method) to generate local geothermal gradients across the US (fig. 6a).

Surface temperatures are derived from mean annual land surface temperature (MAST) measurements for North America between 2003–2014 (Bechtel, 2015) and down-sampled to a 0.1°x0.1° Lat/Long resolution (fig. 6e). The combined 0.1°x0.1° surface temperature (MAST) and corrected geothermal gradient (SMUH) datasets are referred to as the geothermal model. Of the filtered PWGD samples, 11,480 samples (96.9%) are coupled to the geothermal model generating an at-formation-depth temperature for each sample. The geochemical composition and lithological classification of samples in this dataset used in the PHREEQC modelling are summarised in supplementary tables 4 and 5. The majority of unmatched samples are from locations outside the contiguous continental states.

Using PHEEEQC with the Pitzer database (Plummer and others, 1988; Parkhurst and Appelo, 1999), which is valid up to 200°C and halite saturation, fluids are driven from the temperature at which the pH was measured (or 25°C) to their estimated at-formation-depth temperature. The Pitzer database is appropriate here as the median (P50) total dissolved solids is 42,745 mg/l and the median (P50) Pitzer calculated I is 0.85 mol/kg (supplementary table 5). The data (n=11,480) is then filtered such that the subset of samples with $\log_{10}({}^{a}Ca^{2+}/{}^{a}Mg^{2+})$-temperature values outside of the range between SUPCRT92 (slop07.dat) calcite - ordered dolomite & calcite - disordered dolomite equilibriums (termed hereafter the 'SUPCRT92-filter') are excluded as they are determined unlikely to be at calcite-dolomite equilibrium. The remaining samples (n=10,343) constitute the main dataset for the principal regression analysis (supplementary table 4).

Both generalized linear mixed-effects models that use fixed and random effects (lme4; Bates and others, 2014), and linear models that contain only fixed effects, were constructed using R (Team, 2000) to evaluate the relationship between fluid temperature (fixed effect) and $\log_{10}({}^{a}Ca^{2+}/{}^{a}Mg^{2+})$ (outcome variable) (table 2). The relationship is evaluated using variations of the Maier-Kelley thermodynamic regression formula;

$$\log \mathrm{K} = a + bT + \frac{c}{T} + d \log T + \frac{e}{T^2} \tag{19}$$

Models utilising the full five term Maier-Kelley thermodynamic regression formula are found to produce sizeable spurious changes, particularly at temperatures < 25°C, and are not presented. For most analyses in this study a three-term (a, b and c) expansion, as used by Bénézeth and others (2018), is supported by goodness of fit tests, in particular the Akaike information criterion (AIC) (see below). Typically, a three-term model generates very similar

results to a two-term model but also enables the estimation of the heat capacity coefficient $\left(C_p^{\circ}\right)$ and hence is the primary equation used for most models presented.

The application of a mixed-effect model evaluates the variation in the fixed effects for each 'group' of samples which share an identical descriptive attribute such as a commonality in the field or the type of lithology. These descriptive attributes are modelled as random effects. This study evaluates up to 7 different attribute-level random effects present in the majority of all samples; the depth, the formation, the field, the basin, the lithology and the age (broken down into period and series) of a sample. Note that for mixed modelling some missing descriptive attribute data is inconsequential.

As an example, the representative mixed model (J21) that utilises all 7 random effects is coded into R as follows;

$$\begin{aligned}\text{lmer}\Bigg(\log_{10}\left(\frac{{}^{a}\text{Ca}^{2+}}{{}^{a}\text{Mg}^{2+}}\right) \sim 1 + \text{T} \; + \text{I}\left(\text{T}^{-1}\right) + (1|\text{DepthID}) + (1|\text{Field}) \\ + (1|\text{Formation}) + (1|\text{Basin}) + (1|\text{Lithology}) + (1|\text{Period}) \\ + (1|\text{Series}), \text{data} = \text{dataset}\Bigg)\end{aligned} \tag{20}$$

where lmer is the mixed modelling package used (Bates and others, 2014).

For a single sample in the PWGD there is a 3-level (nested) hierarchical structure for spatial data. This is implemented in the mixed model as a series of nested random effects at a dataset level, not needing to be explicitly included in equation (20). The 10,343 samples from different wells share 2,168 unique common fields and these fields are nested together by shared basin (n=53). Similarly for the temporal data the time series (n=35) is nested within a geological period (n=13) (i.e. the Tournasian is in the Carboniferous).

Random effects are described as completely crossed if samples possess every combination of random effect attribute, whilst they are partially crossed if there is some degree of nesting. Typically the attributes of lithology, time-period/series and formation operate as partially crossed random effects. For example, in some cases the formation random effect will be substantially crossed against the basin and field random effects; e.g. the Tensleep Fm. (n=659) spans 7 different basins. In other cases local formations, particularly those related to production, are completely nested within a single field.

An additional attribute is created by collating samples from the same field into groups of similar depth under the assumption that they share a common formation/fluid. The assumption is most reliable where, at an intrafield scale, the subsurface geology is laterally homogenous and hydrologically connected. There are 9,049 unique depth groups which suggests that there are 1,294 (10,343-9,049) repeat measurements of the same depth in the same well. By collating samples taken from similar depths the number of groups is significantly reduced. For example, for a 300m depth interval grouping (e.g. all samples from 600 – 900m) the total number of groups reduces to 3,296.

For the representative model (model J21) the simplified (i.e. presenting all random effects as crossed random effects) formal statistical notation of this 3-term Maier-Kelly regression, 7 random effect model is as follows;

$$\log_{10}\left(\frac{{}^{a}Ca^{2+}}{{}^{a}Mg^{2+}}\right)_{ijklmnpq} = \beta_0 + \beta_1.T_{ijklmnpq} + \beta_2.T^{-1}{}_{ijklmnpq} + U_j + U_k + U_l + U_m + U_n + U_p + U_q + \in_{ijklmnpq} \quad (21)$$

Where $\log_{10}\left(\frac{{}^{a}Ca^{2+}}{{}^{a}Mg^{2+}}\right)_{ijklmnpq}$ represents the i^{th} value of the response variable $\log_{10}({}^{a}Ca^{2+}/{}^{a}Mg^{2+})$, β_0 is the global intercept, $\beta_1$and β_2 are the coefficients for the temperature (K) which is modelled as a fixed effect and $U_{(j\ldots p)}$ are the 7 random intercepts with the subscripts denoting depth(j), field(k), basin(l), formation(m), lithology(n), period(p) and series(q). $\in_{ijklmnpq}$ is the residual or error term for the i^{th} value after accounting for the random effect terms.

The mixed model returns three sets of results that are of interest. At the global-level, the model generates a global intercept (β_0) and global fixed effect coefficients (β_1 and β_2) which effectively describe the properties of the average sample. At the attribute-level the mixed model returns information that describes how much of the model variance can be attributed to each random effect (e.g. 'field' or 'formation') that is implemented. As each random effect is implemented the residual variance ($\in_{ijklmnpq}$) typically reduces.

For each individual group, for example all samples from the Soso field, the model returns coefficients that describe the deviation of the group away from the global-level model. Mixed models that only evaluate the deviation of group data away from the global-level model by generating a new (β_0) intercept for each group are termed random intercept (RI) models. By inserting RI values for different groups into the place of the global intercept, with the global fixed effect coefficients remaining constant, separate local solubility models for different groups can be created. Random slope models further this by incorporating the dependence of the fixed effect coefficients (β_1 and, though not used in this study, β_2) on the random effects such that each group has both an RI value and a random gradient (β_2 and/or β_1) for the $\log_{10}({}^{a}Ca^{2+}/{}^{a}Mg^{2+})$-temperature profile.

A primary feature of mixed modelling is partial pooling. Partial pooling stands in contrast to the alternative strategies of complete and no pooling. Complete pooling models all data as a single group; for example the linear model (model K1) of the entire PWGD represents a complete pooling approach. The main problems with complete pooling are that 1) between-group variations are suppressed and 2) both attribute-level and group-level information, which may be of interest, is lost. Moreover suppressing grouping information can have deleterious effects on uncertainty estimates (German and Hill, 2006). A no-pooling approach models each group separately; for example, for the PWGD this would comprise several thousand linear models of each group of samples with a common attribute. A no-pooling approach overstates the between-group variation with significant, though unreliable, differences between individual groups appearing. The partial pooling approach represents a compromise and a significant advance. All three levels of mixed model results (global-, attribute- and group-level) are informed by both the data contained within each group and group size. Low sample size groups possess less information so both influence the attribute-/global-level results less and have group-level coefficients similar to the attribute-level/global-level results (Gelman and Hill, 2006).

The application and statistical validity of mixed models for datasets with small numbers of observations and groups is an active area of research as applied research is frequently data limited (Bell and others, 2010, Hox and others, 2017). For mixed models there are group and sample size guidelines; Hox and others (2017) suggest that the ratio of the number of groups to the number of individuals in each group be on the order of 100/10 (100 groups of 10 individuals), 50/20 or 30/30. The mixed models (A1 – I1) presented in the ground truthing section below fail these rules of thumb and linear models for these cases are arguably more statistically valid. However the small sample size mixed models correlate well with linear models illustrating the lack of sensitivity of mixed model global-level fixed effect coefficients to limited data (Bell and others, 2010). The primary reason these models are included is because they demonstrate important features of mixed models at a relatable smaller scale. The models for the PWGD (n=10,343 or 11,480) easily surpass minimum group and sample size requirements. The PWGD contains many small sample size groups (n < 5) though this is not thought to significantly affect fixed and random coefficients (Hox and others, 2017).

Model selection aims for the simplest model to describe the relationship between temperature and $\log_{10}({}^{a}Ca^{2+}/{}^{a}Mg^{2+})$, and whilst guided by statistical tests remains an inherently subjective exercise. The AIC, the R^2, 95% confidence intervals (2σ), and the intraclass correlation coefficient (ICC) are statistical tests that assist selection by evaluating goodness of fit and model uncertainty. In particular the AIC compares differently parameterized models, utilizing identical datasets, with the model possessing the lowest AIC value (AIC_{min}) regarded as the best fitting. AIC differences between models smaller than 10 are not regarded as sufficient criteria for model rejection whilst differences smaller than 2 suggest support for both models (Burnham and Anderson, 2002).

We frequently observe that samples from an individual group (e.g. all samples from a single field or formation) appear to have strong within-group similarities, but there are significant differences between-groups often including when the groups are closely linked (for example immediately adjacent fields). The intraclass correlation coefficient (ICC) describes how strongly within-group samples resemble each other or, more specifically by extension, the fraction of total variation of a dataset that can be accounted for by between-group variation (Gelman and Hill, 2006). The ICC is implemented using the method of Nakagawa and others (2017) and (as is typical) we report only the adjusted ICC value, which is the percentage of total variance explained by groups (excluding fixed effect variance). In essence adjusted ICC reflects the reproducibility of replicate measurements from each group. ICC values < 0.4 indicate poor reproducibility, $0.4 \leq ICC < 0.75$ indicate fair to good reproducibility and $ICC \geq 0.75$ indicates excellent reproducibility. For an ICC of zero, observations within-groups are no more similar than observations between-groups and there is no difference between a mixed model (partial pooling) and a linear model (complete pooling). As such the ICC is used as a discriminator for determining whether to apply a mixed model technique. Whilst the fixed effects may change little if moving from a linear to a mixed model, as is the case in many instances in this study, the larger the ICC the greater the impact on the standard error of a regression term and other measures of model uncertainty such as 95% confidence intervals. It is widely recognised that mixed modelling more

accurately quantifies uncertainty for clustered datasets over linear models (Gelman and Hill, 2006).

For linear models only, the adjusted R^2 value is reported. For mixed models, the method of Nakagawa and others (2017) is used to determine the marginal and conditional R^2. The marginal R^2 describes the variance explained by the model that is a product of only the fixed effects and is generally similar to the R^2 of a comparative linear model. The conditional R^2 of a mixed model describes the variance explained by both fixed and random effects and is typically higher than the marginal R^2 as random effects account for some of the variance.

RESULTS

The PWGD samples (n = 11,480) come from a wide range of locations and depths across 30 of the contiguous US continental states, though historically prolific oil producing states such as Wyoming (n = 2,946) and Texas (n = 2,495) are heavily represented (fig. 6d). The range in annual surface temperatures is small (-5 – 21°C) compared to the range of geothermal gradients (11 – 88°C/km) (supplementary table 5; fig. 6a and e). With a median formation depth of 1.9km, the contribution to the estimated at-formation-depth temperature (and uncertainty) from the geothermal gradient ($\sigma = 6$°C/km) is typically twice that of the surface temperature ($\sigma = 6$°C).

The relationship between $\log_{10}({}^{a}Ca^{2+}/{}^{a}Mg^{2+})$ and temperature is initially evaluated for two areas where prior studies demonstrate pore waters are at calcite-dolomite equilibrium, allowing ground truthing of the approach. The areas are the north-eastern section of the Texas Gulf Coast (TGC) basin, studied by Hyeong and Capuano (2001) and to a lesser extent by Morton and Land (1987), and the Mississippi Salt Dome (MSD) basin studied by Kharaka and others (1987). To evaluate the reliability of this study's geochemical and geothermal methodology within these areas we compare both groundwater chemistry data in the PWGD and the at-formation-depth temperatures derived by this study's geothermal model with the published geochemical and temperature data.

Ground Truthing: Thermal Gradients in the Texas Gulf Coast

Datasets from the north-eastern TGC primarily include samples from two formations; the Oligocene Frio Fm. and the Miocene Fm.. The Frio Fm. is comprised of sand-rich fluvio-deltaic sediments that have a variable mineral composition (Loucks and others, 1984), including both detrital carbonate grains (caliche clasts) and diagenetic carbonate cements (Loucks and others, 1980). The Miocene Fm., otherwise known as the Miocene Major Stratigraphic Unit, is comprised of similar fluvio-deltaic sandstones. Both formations are locally cemented by carbonate which comprise ≤ 15% of the total rock volume (Land, 1984; Hyeong and Capuano, 2001). Carbonate cements are primarily calcite, ankerite and dolomite; dolomite constitutes 10 – 15% of the cement and therefore ≤ 0.8% of the total rock volume (Land, 1984; Hyeong and Capuano, 2001).

Within the Frio Fm. Morton and Land (1987) define four regions of typically distinct end-member water compositions, thought to reflect local geochemical processes, influx of waters from deeper aquifers, and structural discontinuities (faults and diapirs) that restrict regional fluid flow. Our Test Area A (bounding box W94°48' – W96°00'/N28°48' – N29°30' totalling some 9,059km^2) lies within the most northerly of Morton and Land's (1987) sub-regions, referred

to here as the 'north-eastern TGC' (fig. 7a and b) and includes the three fields from the seminal high-resolution study of Hyeong and Capuano (2001); the West Columbia, Chocolate Bayou and Halls Bayou fields. Hyeong and Capuano (2001) collated the latter two into the 'Chocolate/Halls Bayou field' presumably due to the small sample size for the Halls Bayou field (n=2), proximity between the fields and the stratigraphic equivalence of the two fields.

For the 21 PGWD samples from 9 different fields within Test Area A the geothermal model yields a mean surface temperature of 16°C (range 15 – 16°C) and a mean geothermal gradient of 33°C/km (range 29 – 35°C/km) (fig. 8a). This is steeper than the geothermal gradient of 25.7°C/km determined using the 16°C surface temperature and the subsurface temperature observations of Morton and Land (1987) for the Chocolate Bayou field. In contrast, using the 16°C surface temperature, the more recent and detailed subsurface temperature observations of Hyeong and Capuano (2001) for the Chocolate Bayou field yield a mean local geothermal gradient of 31°C/km (range 27 – 34°C/km) which is consistent with both Hyeong and Capuano's (2001) interpretation of the mean local gradient (30°C/km) and the estimate for Test Area A PGWD samples (33°C/km).

Both Hyeong and Capuano (2001) and Morton and Land (1987) suggest the presence of significant local vertical variations in geothermal gradients. Hyeong and Capuano (2001) samples from the West Columbia field have a high local gradient of 39°C/km (range 32 – 51°C/km). This is attributed primarily to high temperature samples (43 – 58°C) from the shallow Miocene Fm. (651 – 921m) which, assuming a 16°C surface temperature, have a geothermal gradient range of 40 – 51°C/km. These high gradient values are significantly outside the range generated by the geothermal model for Test Area A (29 – 35°C/km). This suggests that the methodology adopted here generates at-formation-depth temperatures broadly consistent with *in situ* observations, but also highlights limitations when applying simple linear geothermal gradients in areas of complex geothermal regimes.

Ground Truthing: Calcite-Dolomite Equilibrium in the Texas Gulf Coast Frio Formation-Test Area A

All 21 samples from Test Area A in the PWGD are from the Frio Fm. (fig. 7b). These samples are compared with Hyeong and Capuano (2001) data from the West Columbia (43 – 85°C; n=16) and Chocolate/Halls Bayou fields (94 – 150°C; n=35), the majority (88%) of which are also from the Frio Fm.. This area lies within the north-eastern TGC that is characterized by NaCl-type waters derived primarily from the dissolution of salt diapirs (Morton and Land, 1987). It is for these NaCl-type waters (Ca 1,490 mg/l, $[Ca^{2+}]/[Mg^{2+}] \sim 10$) that Hyeong and Capuano (2001) interpret $\log_{10}({}^{a}Ca^{2+}/{}^{a}Mg^{2+})$-temperature trends to be consistent with prior estimations of the calcite-dolomite equilibrium.

A primary concern of Hyeong and Capuano (2001) is evaluating the extent to which the $\log_{10}({}^{a}Ca^{2+}/{}^{a}Mg^{2+})$-temperature relationship reflects either fluid mixing processes or water-rock reactions. Hyeong and Capuano (2001) identify near identical $\log_{10}({}^{a}Ca^{2+}/{}^{a}Mg^{2+})$-temperature relationships in both fields consistent with calcite-dolomite equilibrium and, after also comparing Ca^{2+} and Mg^{2+} against conservative ions Cl^{-} and Br^{-}, conclude $\log_{10}({}^{a}Ca^{2+}/{}^{a}Mg^{2+})$ values in both fields are unlikely to have resulted from mixing. Any mixing that may have occurred is now irrelevant as calcite-dolomite equilibrium is (re)established. This interpretation would be inaccurate if mixing

were to generate a calcite and/or dolomite undersaturated fluid within a host formation that lacks sufficient material or time to enable the attainment of, yet serendipitously has $\log_{10}({}^{a}Ca^{2+}/{}^{a}Mg^{2+})$-temperature values coincident with, calcite-dolomite equilibrium. This situation may theoretically occur in very clean clastic formations. However, as the number of brine samples and sampled locations increases, there seems a low probability that mixing can result in sizeable numbers of samples with $\log_{10}({}^{a}Ca^{2+}/{}^{a}Mg^{2+})$-temperature values coincident with prior estimations of calcite-dolomite equilibrium yet out of equilibrium with either mineral. By extension, as the sample population size/diversity increases and the $\log_{10}({}^{a}Ca^{2+}/{}^{a}Mg^{2+})$-temperature relationship becomes more pronounced, so does the confidence that $\log_{10}({}^{a}Ca^{2+}/{}^{a}Mg^{2+})$-temperature profiles can reliably be used and converted into K_{sp-dol} models.

Combining data from the two fields Hyeong and Capuano (2001) construct a 2-term Maier-Kelley linear model (herein termed model A1) to determine the thermodynamic properties, including the ordering parameter (s = 0.4), of the local dolomite over a wide temperature range (43 – 150°C). Key model information for this literature model and all models constructed by this study are summarized in table 2 and fully reported in supplementary table 6.

Hyeong and Capuano (2001) use the following Maier-Kelly regression;

$$\log_{10} \frac{{}^{a}Ca^{2+}}{{}^{a}Mg^{2+}} = a + b\ \frac{T(°C)}{1000} \tag{142}$$

to determine the relationship between temperature and $\log_{10}({}^{a}Ca^{2+}/{}^{a}Mg^{2+})$ (as calculated by SOLMNEQ88-Pitzer) evaluating a as -0.22 and b as 7.21 (model A1). We recalculate the Hyeong and Capuano (2001) dataset using a PHREEQC-Pitzer approach and (as with all models in this study) use a 2-term eq (19) Maier-Kelly regression formula (replacing the $\frac{T(°C)}{1000}$ term with T(K)). This linear model (model A2) is almost identical to model A1 (fig. 9a) indicating that a) PHREEQC-Pitzer determined activities are largely consistent with those determined by SOLMNEQ88-Pitzer analysis (supplementary figure 1), and b) the usage of different statistical packages and regression formulas generates consistent results, including for goodness of fit (model A1 $R^2 = 0.94$ and model A2 $R^2 = 0.86$).

Comparing mixed models of the recalculated Hyeong and Capuano (2001) dataset, a three-term Maier-Kelly expansion (model A3, AIC = -107.4) provides a better fit to the dataset than a two-term expansion (model A4, AIC = -84.4). However, given the small size of the dataset (n = 51), three-term models (such as model A3) generate spurious extrapolations beyond the data range (fig. 9a). A two-term expansion is the regression formula used for small (n < 400) datasets. There are minimal differences between the random intercept mixed model A4 and a random slope mixed model A5 (fig. 9a) including for group level results, and AIC favors model A4 (A4 = -84.4 and A5 = -77.1). Random slope models such as model A5 are likely to be a better representation of variations in $\log_{10}({}^{a}Ca^{2+}/{}^{a}Mg^{2+})$-temperature relationships as, for example, fields are likely to see different local effects (e.g. the dolomite composition/order) at distinct depths. However, at present the causes for variations in $\log_{10}({}^{a}Ca^{2+}/{}^{a}Mg^{2+})$-temperature gradients are poorly constrained and random slope models are not evaluated further.

Using linear models to separately evaluate (no-pooling approach) the

Chocolate/Halls Bayou (model B1, n = 35) and West Columbia (model C1, n = 164) fields reveals significant variations between the $\log_{10}({}^{a}Ca^{2+}/{}^{a}Mg^{2+})$-temperature profiles (fig. 8b). At 25°C $\log_{10}({}^{a}Ca^{2+}/{}^{a}Mg^{2+})$ is 0.31 higher for the West Columbia field (model C1) whilst the $\log_{10}({}^{a}Ca^{2+}/{}^{a}Mg^{2+})$-temperature gradient is steeper for the Chocolate/Halls Bayou field (model B1). This reflects the inclusion of samples from the Miocene Fm. within the West Columbia field dataset. Comparing linear models of the separate formations (fig. 9c) suggests that Frio Fm. samples from both fields (model D1) are similar. Samples from the Miocene Fm. have a different $\log_{10}({}^{a}Ca^{2+}/{}^{a}Mg^{2+})$ trend with temperature (model E1), but the significance of this is limited (R^2 of -0.24) due to the small number (n = 6) and limited temperature range (43 – 58°C) of Miocene Fm. samples.

Hyeong and Capuano (2001) established a complete pooling approach precedent of combining observations from different fields and formations to increase the temperature range of a K_{sp-dol} model. Application of the mixed model approach to the Hyeong and Capuano (2001) dataset (n=51) (model A4) generates an adjusted ICC value of 0.441, indicating that grouping explains a significant amount of the variance (44.1%; good to fair reproducibility for grouped data – Rosner (2015)). As is expected for grouped data, the conditional R^2 of the mixed model A4 (0.90) is larger than the marginal R^2 (0.83), indicating that the application of random effects improves model fit; note the marginal R^2 of model A4 also approximates the R^2 of the linear model A2 (0.84). Model A4 and model A2 have very similar profiles (fig. 9a) however the uncertainty is substantially larger for model A4. The standard error on the intercept $\log_{10}({}^{a}Ca^{2+}/{}^{a}Mg^{2+})$ value rises from 1.49×10^{-1} log unit for model A2 to 2.44×10^{-1} log unit for model A4. Similarly, the width of the 95% confidence interval at 25°C rises from 0.13 (model A2) to 0.39 (model A4) (fig. 9a). This is consistent with uncertainties determined by linear models being erroneous underestimates for clustered data (Gelman and Hill, 2006). However, AIC indicates that the linear model A2 (-107.1) is better than the mixed model A4 (-84.4), reflecting the overparameterization (limited numbers of group/sample size) of the mixed model. For only marginally larger datasets, AIC values favor mixed models over linear models though the statistical validity/reliability of mixed models may not be assured until group/sample size criteria are met (Hox and others, 2017).

Had Hyeong and Capuano (2001) would have observed significant disparities between-groups had they adopted a no-pooling approach (compare linear models C1, B1, D1 and E1; fig. 9b and c). Mixed modelling clearly reduces the disparities between-groups yet retains group-level information. For example the difference in $\log_{10}({}^{a}Ca^{2+}/{}^{a}Mg^{2+})$ values between the B1 (Chocolate/Halls Bayou) and C1 (West Columbia) linear models is 0.31 log unit at 25°C. In contrast the difference between the RI values (model A4) of the Chocolate/Halls Bayou and West Columbia fields, and by extension $\log_{10}({}^{a}Ca^{2+}/{}^{a}Mg^{2+})$ values at all temperatures, is a more reasonable 0.04 (log unit) (fig. 9b).

This study reports only the mixed model random intercept values for individual groups (supplementary table 7). These are not combined straightforwardly if a group-level result is required for multiple attributes/random effects but the (supplementary) R code is capable of generating such models. For example, the Chocolate/Halls Bayou field only contains Frio Fm. samples, however the profiles of the A4 mixed model results for the group with a single random effect of 'Chocolate/Halls Bayou field' (fig. 9b) and the group result for 'Chocolate/Halls Bayou field - Frio Fm.' (fig.9b and 9c) are noticeably different. This is

due to Frio Fm. samples from the West Columbia field having high $\log_{10}({}^{a}Ca^{2+}/{}^{a}Mg^{2+})$ values affecting all group-level models incorporating a Frio Fm. attribute.

As is commonly found in the PWGD, samples from Test Area A (n = 21) do not sample multiple depths in each of the 9 fields. Instead there is high representation from a few individual fields and from a narrow range of production related depths (for example see the discussion of Frio Fm. below). This contrasts with the wide range of sampled depths within closely spaced fields in the Hyeong and Capuano (2001) dataset. The typically more limited coverage in the PWGD means it is poorly suited to such single field analyses. However we demonstrate consistency between the $\log_{10}({}^{a}Ca^{2+}/{}^{a}Mg^{2+})$- temperature profiles/models of the PWGD samples in Test Area A (n = 21; model F1) and the Hyeong and Capuano (2001) samples (n = 51; model A4) (fig. 9d). The global-level fixed effect coefficients of the F1 and A4 models are similar with the difference between $\log_{10}({}^{a}Ca^{2+}/{}^{a}Mg^{2+})$ values at 25°C just 0.01 log unit. This $\log_{10}({}^{a}Ca^{2+}/{}^{a}Mg^{2+})$-temperature consistency between the PWGD and the Hyeong and Capuano (2001) dataset supports the reliability of the PWGD data. Note the PWGD contains a significant amount of data from published studies, but the samples contained within the PWGD are all different to those present in the Hyeong and Capuano (2001) dataset (fig. 7b).

Expanding upon Hyeong and Capuano (2001) this study interprets that $\log_{10}({}^{a}Ca^{2+}/{}^{a}Mg^{2+})$ values for all waters within Test Area A are buffered by calcite-dolomite equilibrium. Moreover, as $\log_{10}({}^{a}Ca^{2+}/{}^{a}Mg^{2+})$ values for all fields are comparable, the local effects across all fields in Test Area A are interpreted to be similar suggesting related geological and hydrological histories for these proximal fields.

Ground Truthing: Calcite-Dolomite Equilibrium in the Texas Gulf Coast Frio Formation – Southern Texas to Central Louisiana

In comparison to samples taken solely from Text Area A, a larger sample set encompassing all PWGD Frio Fm. samples from southern Texas to central Louisiana (n=117, including 21 samples from Test Area A; fig.7a) records higher $\log_{10}({}^{a}Ca^{2+}/{}^{a}Mg^{2+})$ values at lower temperatures and considerable scatter (fig. 9d). The large scatter suggests significant local effects which may include variations in the local dolomite composition, or potentially relate to the heterogeneity of Frio Fm. water compositions (Morton and Land, 1987).

The Frio Fm. dataset (n = 117) covers 48 fields but 35 fields have 2 or less samples, and the largest single field dataset (n = 21 from the Seeligson field) only spans a narrow 15°C temperature range (66 – 81°C). Combined with the substantial scatter these two population characteristics preclude using only Frio Fm. samples to conduct a single field type analysis, similar to Hyeong and Capuano (2001), that aims to reduce local effect impacts on $\log_{10}({}^{a}Ca^{2+}/{}^{a}Mg^{2+})$ through spatial constraints. Despite the scatter we argue the vast majority (92%) of PWGD Frio Fm. samples could be interpreted as being at calcite-dolomite equilibrium. Only nine samples (8% of Frio Fm. samples) have $\log_{10}({}^{a}Ca^{2+}/{}^{a}Mg^{2+})$ values greater than SUPCRT92 calcite-ordered dolomite equilibrium and are deemed unlikely to be at calcite-dolomite equilibrium. These samples, which are all in the southern TGC, are compositionally similar to the CaCl-type Frio Fm. waters (Ca = 22,260 mg/l, $[Ca^{2+}]/[Mg^{2+}]$ >100) identified by Morton and Land (1987).

The $\log_{10}({}^{a}Ca^{2+}/{}^{a}Mg^{2+})$ value for the mixed model (G1) of the PWGD Frio Fm.

dataset is, at 25°C, a substantial 0.46 log unit higher than model A4 for Test Area A samples (fig. 7d). The question is therefore whether high $\log_{10}({}^{a}Ca^{2+}/{}^{a}Mg^{2+})$ values are consistent with, and by extension the range of $\log_{10}({}^{a}Ca^{2+}/{}^{a}Mg^{2+})$ values indicative of, calcite-dolomite equilibrium. High equilibrium $\log_{10}({}^{a}Ca^{2+}/{}^{a}Mg^{2+})$ values are supported by Hyeong and Capuano's (2001) interpretation that the formational brines in the Cretaceous Edwards group of south-central Texas (Land and Prezbindowski, 1981) are at calcite-dolomite equilibrium (fig. 9d). For these brines (49 – 176°C) Hyeong and Capuano (2001) note a similar $\log_{10}({}^{a}Ca^{2+}/{}^{a}Mg^{2+})$-temperature gradient to that observed in the West Columbia and Chocolate/Halls Bayou fields, but with $\log_{10}({}^{a}Ca^{2+}/{}^{a}Mg^{2+})$ values shifted ~ 0.1 log unit higher. The Edwards group primarily consists of dolomitized limestones and Hyeong and Capuano (2001) interpret that a more ordered dolomite phase, than that found in the West Columbia and Chocolate/Halls Bayou fields, is buffering $\log_{10}({}^{a}Ca^{2+}/{}^{a}Mg^{2+})$ to high values. As such Hyeong and Capuano, (2001) state that their reference model (model A1) is not valid for equilibrium between calcite and more ordered dolomite phases.

Ground Truthing: Thermal gradients in the Mississippi Salt Dome Basin

The Mississippi Salt Dome (MSD) basin is mostly located in central Mississippi and is separated from the TGC basin to the south by the Wiggins, South Mississippi, and La Salle uplifts. Kharaka and others (1987) sample (n = 17) a range of clastic and carbonate Upper Cretaceous (Stanley Fm.) to Upper Jurassic (Norphlet Fm.) reservoirs (70 – 120°C) in 7 MSD basin fields. The Kharaka and others (1987) dataset is much lower resolution than that of Hyeong and Capuano (2001) and only the Reedy (1920 – 3485m; 68 – 102°C; n = 5) and Soso (1965 – 2875m; 68 – 89°C; n = 3) fields sample a wide depth/temperature range.

Test Area B, which encompasses the 7 fields sampled by Kharaka and others (1987), spans the Alabama-Mississippi border and has an area of 13,224km^2 (fig. 7c, bounding box W88°12' – W90°00'/N31°30' – N32°12'). For the 204 PGWD samples, from 35 different oil fields, contained within Test Area B the geothermal model yields a mean surface temperature of 13°C (range 12 – 14°C) and a mean geothermal gradient of 27°C/km (range 22 – 34°C/km) (fig. 8b). Assuming a 13°C surface temperature, the mean geothermal gradient for the Kharaka and others (1987) dataset is calculated to be 26°C/km (25 – 29°C/km) which is comparable to the mean gradient predicted by this study's geothermal model. Moreover, in both datasets samples from the Soso field are present but critically non-identical. Interestingly the most similar Soso samples from depths of 2031m in the PWGD and 1965m in Kharaka and others (1987) dataset have predicted (PWGD) and observed (Kharaka and others, 1987) temperatures of 69°C and 68°C respectively.

At-formation-depth temperatures predicted for Test Area B have a greater range than those for Test Area A (fig. 7a). This probably reflects both a wider sampling area and the substantial faulting and salt tectonics that characterize the MSD basin. In particular salt domes can dramatically increase the lateral heterogeneity of local geothermal gradients (Daniilidis and Herber, 2017). In Test Area B several fields, including the well represented Raleigh and Soso fields, are proximal (< 5km) to salt domes whilst in Test Area A the majority of fields are ≥ 15km away from a salt dome.

Ground Truthing: Calcite-Dolomite Equilibrium in the Central Mississippi Salt Dome Basin

For a given water analysis the presence of calcite-dolomite equilibrium has been interpreted using two separate standards.

1) Most commonly calcite-dolomite equilibrium is interpreted through evaluating saturation indices for both minerals. Kharaka and others (1987) interpreted all samples (n = 17) to be at (SOLMINEQ.87) calcite-dolomite equilibrium (-0.5 < SI < 0.5) and attribute this to relate to the substantial dolomitization of the limestone Smackover Fm. (Carpenter and Trout, 1978; Kharaka and others, 1987).
2) Calcite-dolomite equilibrium can also be interpreted if the $\log_{10}({}^{a}Ca^{2+}/{}^{a}Mg^{2+})$ *or* $[Ca^{2+}]/[Mg^{2+}]$-temperature relationship is consistent with prior estimates (Land and Prezbindowski, 1981; Dutton, 1987; Hyeong and Capuano, 2001; Vespasiano and others, 2014; Blasco and others, 2018). This method of interpretating the presence of calcite-dolomite equilibrium has typically only been applied whilst evaluating K_{sp-dol} and/or the order of the natural dolomite phase (see 'Solubility (groundwater)' supplementary table 2). Within the Kharaka and others (1987) dataset the increase in $\log_{10}({}^{a}Ca^{2+}/{}^{a}Mg^{2+})$ with temperature for both the Reedy and Soso fields are consistent with calcite-dolomite equilibrium (fig. 9d).

Comparing PWGD data from Test Area B (n = 204) to the Kharaka and others (1987) dataset they are compositionally similar further validating the PWGD dataset. The mixed model of both the Test Area B dataset (model I1) and the linear model (H1) of the Kharaka and others (1987) dataset have high $\log_{10}({}^{a}Ca^{2+}/{}^{a}Mg^{2+})$ values, most similar to those in the Frio Fm. (model G1) and the Edwards group (fig. 9c and d). Test Area B samples are most different to the Test Area A samples, though interestingly the models for these datasets (models A4 and I1) and others discussed intersect around ~120°C suggesting differences are more pronounced at low temperatures.

Expanding upon Kharaka and others (1987) and Hyeong and Capuano (2001) this study interprets that the high $\log_{10}({}^{a}Ca^{2+}/{}^{a}Mg^{2+})$ waters present within the Edwards group, Test Area B and most, but not all, of the Frio Fm. are consistent with calcite-dolomite equilibrium. The range of $\log_{10}({}^{a}Ca^{2+}/{}^{a}Mg^{2+})$ values at a specific temperature that can be considered consistent with an interpretation of calcite-dolomite equilibrium is therefore wide, the width being further evaluated below, and attributed to local effects.

Distribution of samples in the PWGD

Geothermal model.—The highest spatial resolution of this study's geothermal model (fig. 6a) is in hydrocarbon-producing basins as oil and gas wells are the primary data source for the SMUH dataset (fig. 6b; Blackwell and others, 2011). Ground truthing for two such data-rich areas (Test Areas A and B) established the reliability of the geothermal model.

Blackwell and others (2011) produced two interpolated maps (fig. 6c) for heat flow and temperature at two specific depths (6.5km and 9.5km). Comparing this study's interpolation with that of Blackwell and others (2011), we find them to be mostly similar, though note a small number of disparities. For example, in parts of northern Virginia, this study's geothermal model and the Blackwell and others (2011) model respectively resolve opposing high and low geothermal anomalies. However, disparities between the interpolated models are typically in data poor areas, such as Virginia, where interpolations are less reliable. In comparison, more marginal differences are observed in higher data density areas,

such as in south Texas, where the Blackwell and others (2011) interpolation resolves geothermal features to a much finer spatial resolution than this study's geothermal model suggesting the lateral resolution could be increased further.

As discussed for the Miocene Fm. samples in Test Area A, linear geothermal gradients over-simplify vertical thermal heterogeneities. Significantly more processing, outside the scope of this study, would be needed to generate an interpolated 3D temperature model. However, as established for Test Areas A and B, we interpret that the geothermal model generates robust at-formation-depth temperatures for most samples.

Geochemistry.— For the entire temperature range the $\log_{10}({}^{a}Ca^{2+}/{}^{a}Mg^{2+})$-temperature frequency distribution is leptokurtic (kurtosis > 3) for all PWGD samples (n = 11,480; kurtosis = 8.0). The sandstone, dolomite, and limestone lithologies, that together account for 94% of PWGD samples (supplementary table 4), have kurtosis values of 7.5, 8.4 and 8.6 respectively.

Binning PWGD samples into 10°C intervals, between 20 – 120°C, leptokurtic distributions of $\log_{10}({}^{a}Ca^{2+}/{}^{a}Mg^{2+})$ values are observed in each bin, including for each of the three common lithologies (fig. 10d). For the bins containing the small proportion (7%) of samples outside the 20 – 120°C range kurtosis values are significantly lower (fig. 10g). However low kurtosis values could be an artifact as small datasets are rarely consistent with a normal distribution, a necessary assumption for the kurtosis and skewness parametric tests (Rosner, 2015). Kurtosis reflects little about the distribution of samples within 1 σ from the mean and is a poor descriptor of the 'peakedness' of the data (Westfall, 2014). Leptokurtic distributions instead reflect the presence of significant numbers of outliers which is consistent with 10% (n=1,137/11,480) of PWGD samples having $\log_{10}({}^{a}Ca^{2+}/{}^{a}Mg^{2+})$ values above or below the upper and lower bounds of the SUPCRT92-filter. The σ is a better quantitative descriptor for the peakedness. For each 10°C bin typically the σ of $\log_{10}({}^{a}Ca^{2+}/{}^{a}Mg^{2+})$ values is ~ 0.3 log unit which represents a surprisingly narrow interval and a peaky distribution. Moreover, as the equilibrium $\log_{10}({}^{a}Ca^{2+}/{}^{a}Mg^{2+})$ value rises across a 10°C bin the 0.3 σ value is an overestimate.

All PWGD samples are further binned into equal interval bins of dimensions 0.05 $\log_{10}({}^{a}Ca^{2+}/{}^{a}Mg^{2+})$ x 10°C to evaluate the frequency distribution of $\log_{10}({}^{a}Ca^{2+}/{}^{a}Mg^{2+})$ values (fig. 10a). The $\log_{10}({}^{a}Ca^{2+}/{}^{a}Mg^{2+})$ value of the modal $\log_{10}({}^{a}Ca^{2+}/{}^{a}Mg^{2+})$ bin for each 10°C range, through which the mixed models of the entire PWGD presented below typically intersect (fig. 5b), increases with temperature in a manner consistent with prior evaluations of calcite-dolomite equilibrium (fig. 10b). This consistency combined with the peaky distribution is interpreted as reflecting that the majority of PWGD groundwaters are at bulk calcite-dolomite equilibrium. Were the $\log_{10}({}^{a}Ca^{2+}/{}^{a}Mg^{2+})$-temperature relationship less pronounced we may have interpreted buffering by surface phases. Moreover as the majority (90%, n=10,343/11,480) of PWGD samples have $\log_{10}({}^{a}Ca^{2+}/{}^{a}Mg^{2+})$ values between the upper and lower bounds of the SUPCRT92-filter the application of the SUPCRT92-filter, to remove samples unlikely to be at calcite-dolomite equilibrium, does appear to be an appropriate statistical filter to increase the reliability of the $K_{\psi^{\circ}-dol}$ model.

For the dolomite, limestone and sandstone lithologies the $\log_{10}({}^{a}Ca^{2+}/{}^{a}Mg^{2+})$ frequency distributions appear to be largely unimodal with similar modal values (fig. 10b).

As we interpret the primary control on $\log_{10}({}^{a}Ca^{2+}/{}^{a}Mg^{2+})$ values is the dolomite composition this may reflect a broad similarity of dolomite compositions in very different lithologies. Closely examining frequency distributions there is some evidence for the presence of additional modes. The clearest potentially multimodal distribution, the sandstone 80 – 90°C bin, appears to be bimodal with identical (n=40) peaks at $0.35 < \log_{10}({}^{a}Ca^{2+}/{}^{a}Mg^{2+}) \leq 0.4$ and $0.6 < \log_{10}({}^{a}Ca^{2+}/{}^{a}Mg^{2+}) \leq 0.65$ (fig. 10i). Nevertheless support for the presence of systematic additional modes is weak and meaningful identification of additional modes is also challenged by the presence of repeat samples from a single depth/formation. Note that replicate measurements are well accounted for by mixed models where they strengthen group weightings.

In contrast to modal $\log_{10}({}^{a}Ca^{2+}/{}^{a}Mg^{2+})$ values, which are mostly similar, mean $\log_{10}({}^{a}Ca^{2+}/{}^{a}Mg^{2+})$ values (fig. 10c) for the limestone population are systematically higher than the dolomite population, particularly between 50 – 100°C (which contains 44% of all limestone-hosted and 25% of all dolomite-hosted samples). This disparity is primarily due to the skewed distribution of the limestone population, which for 50 – 100°C is categorised (Bulmer, 1979) as either moderately (skewness between -1 and -0.5 or +1 and +0.5) or heavily (skewness < -1 or > 1) skewed, with values up to +2.73 for the 60 – 70°C temperature bin (fig. 10e). A positive skew indicates that the tail of the frequency distribution of $\log_{10}({}^{a}Ca^{2+}/{}^{a}Mg^{2+})$ values is thicker on the side with higher $\log_{10}({}^{a}Ca^{2+}/{}^{a}Mg^{2+})$ values and that the modal $\log_{10}({}^{a}Ca^{2+}/{}^{a}Mg^{2+})$ value < median < mean. For all limestone samples the skewness is +0.57, which is significant in comparison to the approximately symmetric values (skewness between -0.5 and +0.5, Bulmer, 1979) of +0.11 and +0.18 for the sandstone and dolomite lithologies respectively and +0.25 for all the PWGD data. Tentatively, we infer the presence of a systematic local effect that causes a positive skew in the limestone population. From the perspective of dolomite composition we can interpret the modal equilibrium dolomite composition in the limestone-hosted population to be somewhat calcian. Compared to the modal composition few limestone-hosted dolomites are significantly more calcian (low $\log_{10}({}^{a}Ca^{2+}/{}^{a}Mg^{2+})$ values), whilst a higher number of limestone-hosted dolomites have significantly more stoichiometric compositions (high $\log_{10}({}^{a}Ca^{2+}/{}^{a}Mg^{2+})$ values).

PWGD Mixed Modelling

Mixed modelling for the entire PWGD focuses on developing both a representative statistical model between $\log_{10}({}^{a}Ca^{2+}/{}^{a}Mg^{2+})$ and temperature, and a K_{sp-dol} model. All models below utilize the SUPCRT92-filtered dataset (n=10,343) and a 3-term Maier-Kelly mixed model unless otherwise stated. To appropriately parameterize the mixed model of PWGD data the number of random effects utilized is incrementally increased. The extent to which a particular model over- or under-fits data is evaluated using goodness of fit measures so justifying modelling decisions. For example, we refine the classification scheme by which samples are categorized into different depth groups.

Grouping by depth.— We compare a series of mixed models of the PWGD dataset utilizing only the depth random effect (models J2 – J9) but with varying depth interval widths. Beginning with a model with no depth-dependent grouping of samples (no. of depth groups

= 8201; AIC = -2754; model J2) increasing the depth interval width results in AIC values decreasing up to 300m (no. of depth groups = 3,296; AIC = -3197; model J7). Thereafter as the grouping interval increases so also do AIC values, to a maximum reported here of 500m (no. of groups=3,040; AIC=-3153; model J9). The minimum AIC value for the 300m grouping interval suggests this is an optimal balance between over- and under-parameterization.

From a hydrogeological perspective a 300m grouping interval seems to be toward the upper end of a reasonable depth range. However, the vast majority of depth groups contain samples from a relatively narrow range of depths (typically <50m) which correspond to particular production zones. The primary purpose of the depth random effect is to incorporate the variance attributable to repeat sampling of similar formational fluids over a narrow range of depths. A secondary purpose is the potential to evaluate variations in $\log_{10}({}^{a}Ca^{2+}/{}^{a}Mg^{2+})$ values at different depths in a field, by using group-level RI values. This may be particularly useful in fields where there is either a lack of detail about the formations present or the formations are thick and discretely stratified into isolated reservoirs with potentially different fluid compositions. In comparison to other models that utilize only a single random effect (models J10–J15) the 300m depth-only random effect model is clearly the best model.

We exemplify the relevance and applicability of the depth grouping with the example of the Seeligson field, Texas (n=51). Seeligson field samples come from 2 recognised formations, the Frio Fm. (n=20) and the Vicksburg Fm. (n=1), with the remainder (n=30) from one of 13 less informative production-related formational names such as '3300 Water Sand' (n=7) and 'A' (n=1). In contrast to grouping by one of 15 different formations, the 300m interval grouping generates 8 different groups which appear to reasonably collate samples from similar production horizons. The Frio Fm. samples are primarily split into two groups; depth groups 'AT4' (n = 5; depth of all samples identical at 1.44km) and 'AT5' (n = 13; sampled from depths between 1.79 – 1.86 km) which respectively correspond to the Seeligson production zones '14' (channel-fill deposits) and '20' (floodplain deposits with carbonate nodules noted) (Ambrose and others, 1992).

Below we construct the main reference mixed model of this study (model J21). In comparison to the global-level intercept (-1.91) the model J21 group-level RI value(s) for the Seeligson field is -1.81 and for the 'AT4' and 'AT5' depth groups are -1.58 and -1.89 respectively. As is commonly encountered by this study a lack of detailed mineralogical/lithological information for the Seeligson field makes it hard to interpret the causes of differences in RI values. Nevertheless and as an example, based solely on RI values we would interpret that the dolomite composition corresponding to the 'AT5' depth group is more calcian than that corresponding to the 'AT4' group.

Combining random effects.—In comparison to a linear model (AIC = -1455; model J1) of the PWGD data, all single random effect mixed models (models J10 – J15) have lower AIC values affirming both the use of mixed models and the inclusion of these specific attributes.

There is only limited support for the time-period-only (AIC = -1457; model J14) and time-series-only (AIC = -1501; model J15) models. The PWGD subset possesses time-series and time-period information for only 55 and 59% of samples respectively, contrasting with

other attributes where completeness is either a criterion for inclusion (such as the sample lithology) or are near complete (e.g. n = 10,308/10,343 samples have formational information). This may be a significant contributing factor in the observed statistical weakness of the time-period and time-series models.

A general trend is observed that model AIC values decrease as the spatial resolution of the grouping attribute, and by extension the number of groups that describe the data, increases. In decreasing order of AIC values the single random effect models are ranked; time-period model (13 period groups; AIC = -1457; model J14), time-series model (35 series groups; AIC = -1457; model J15), lithology model (5 lithology groups; AIC = -1524; model J13), basin model (53 basin groups; AIC = -1815; model J11), formation model (1228 formation groups; AIC = -2640; model J12), field model (2,168 field groups; AIC = -2828; model J10), and the 300m interval depth model (3,296 depth groups; AIC = -3197; model J7). There are three exceptions to this 'more groups better model' trend. As aforementioned the depth-only model with no sample groupings (model J2) has a higher AIC value than other depth-only models that group samples by a depth range. Similarly model J2 has a higher AIC than the field-only model (model J10) and this highlights the overparameterization in model J2 and the benefit of using depth interval groupings. Lastly we speculate data completeness may explain why the lithology model (model J13) has a lower AIC than the time-period (model J14) and time-series (model J15) models.

Systematically combining multiple random effects, both model fit and the capability to reliably describe a wide variety of sample attributes are progressively improved. As determined by AIC the best fitting model, the reference model (AIC = -3595; model J21), utilizes all 7 random effects (depth, field, basin, formation, lithology, time-period and time-series). AIC values are only marginally (< 5) higher for the 4-random effect (Depth-Field-Basin-Formation; -3591; model J18) and 5-random effect (Depth-Field-Basin-Formation-Lithology; -3590; model J19) mixed models indicating some support for these models. The inclusion of lithology and time-period/time-series random effects have a minimal effect on both the global/attribute/group-level results, but the inclusion of these random effects is clearly not penalized by AIC for overparameterization. As such the 7-random effect model (model J21) is selected as the representative model.

Global-level model results are relatively similar for all models; the linear model (model J1) and the reference model (model J21) have $pK_{sp^{\circ}\text{-}dol}$ values of -17.24±0.02 and -17.27±0.35 respectively. The width of the confidence intervals typically reduces as mixed models incorporate increasing numbers of random effects; the maximum uncertainty is shared by the lithology and time-period single random effect models (±0.45; models J13 and J14). Note again the narrow uncertainty for the linear model (±0.02) which reflects the erroneous underestimation of uncertainty for clustered data (Gelman and Hill, 2006). The ICC value for the reference model J21 is 46.6% (good to fair reproducibility for grouped data – Rosner, 2015), which indicates that grouping is indeed significant for PWGD data and a mixed modelling approach is appropriate.

Reference model J21/J23: Global level results.— We present two closely related 7-random effect 3-term Maier-Kelly reference models in terms of the fixed effects (see supplementary

table 7 for RI values). Firstly the representative model (model J21) for the observed $\log_{10}({}^{a}Ca^{2+}/{}^{a}Mg^{2+})$ values;

$$\log_{10}\left(\frac{{}^{a}Ca^{2+}}{{}^{a}Mg^{2+}}\right) = -1.90790 + 5.84297 \times 10^{-3} \cdot T(K) + 1.40778 \times 10^{2} \cdot \frac{1}{T(K)} \quad (23)$$

Secondly for every sample the $\log_{10}({}^{a}Ca^{2+}/{}^{a}Mg^{2+})$ value is converted to a pK_{sp-dol} value using the SUPCRT92 pK_{sp-cal} model (table. 1; eq 9). A reference model (model J23) is constructed using these pK_{sp-dol} values;

$$pK_{sp\text{-}dol} = 1.47545 \times 10^{1} - 6.24959 \times 10^{-2} \cdot T(K) - 3.99350 \times 10^{3} \cdot \frac{1}{T(K)} \quad (24)$$

Converting back to calcite-dolomite equilibrium $\log_{10}({}^{a}Ca^{2+}/{}^{a}Mg^{2+})$ values, using pK_{sp-cal} values from SUPCRT92, the model J23 values are largely identical to model J21 (table 2; fig. 5a) up to temperatures of ~200ºC; hence the purported validity (0 – 200ºC) of model J23 (equations 2 and 24). More broadly the attribute/group-level results of both models J23 and J21 correlate well.

DISCUSSION

The primary observation from this study is an overall increase in $\log_{10}({}^{a}Ca^{2+}/{}^{a}Mg^{2+})$ values with temperature for most subsurface fluids in the contiguous continental states (fig. 10A). Between 25 – 200°C the representative model (model J21) determines that fluids with $\log_{10}({}^{a}Ca^{2+}/{}^{a}Mg^{2+})$ values between the SUPCRT92-filter (n=10,343), have a +0.85 log unit increase in $\log_{10}({}^{a}Ca^{2+}/{}^{a}Mg^{2+})$ values consistent with previous estimates of the calcite-dolomite equilibrium (fig. 5b). Model K1 is identically parameterized to the reference model (model J21) but includes samples outside the range of the SUPCRT92-filter (n=11,480). Between 25 – 200°C model K1 determines a +0.52 log unit increase in $\log_{10}({}^{a}Ca^{2+}/{}^{a}Mg^{2+})$ values (fig. 5a) suggesting that there is a real and significant increase in $\log_{10}({}^{a}Ca^{2+}/{}^{a}Mg^{2+})$ values with temperature that is not simply an artifact of the implementation of the SUPCRT92-filter.

Calcite is the most common and ubiquitous carbonate phase in rocks and exhibits retrograde solubility. In the absence of dolomite and assuming any Mg present in the fluid is conservative and constant, equilibrium only with calcite could generate a $\log_{10}({}^{a}Ca^{2+}/{}^{a}Mg^{2+})$ response with temperature due changes primarily in ${}^{a}Ca^{2+}$. We simulate $\log_{10}({}^{a}Ca^{2+}/{}^{a}Mg^{2+})$ values between 25 – 200°C using PHREEQC (Pitzer database) of a calcite-only buffered solution with a constant initial $[Mg^{2+}]$ (0.01 mol/kgw) and *I* (0.85 mol/kgw – NaCl buffered); these values reflects the PWGD median Mg concentration and *I* (supplementary table 5). The model determines that equilibrium $\log_{10}({}^{a}Ca^{2+}/{}^{a}Mg^{2+})$ values increase by an insignificant 0.10 log unit over this temperature range from -1.34 to -1.23 log unit which contrasts with the model J21/J23 0.85 log unit increase (fig. 5b).

We evaluate other suggested mechanisms, aside from calcite-dolomite equilibrium, that could buffer fluids to the observed $\log_{10}({}^{a}Ca^{2+}/{}^{a}Mg^{2+})$ - temperature profile. Firstly, we critique the interpretations of Möller and De Lucia (2020) who suggest that $\log_{10}({}^{a}Ca^{2+}/{}^{a}Mg^{2+})$ values are reflective only of buffering by Mg-calcite surface phases. Secondly, we address other potential sources of error and local variations that could affect

$\log_{10}({}^{a}Ca^{2+}/{}^{a}Mg^{2+})$ - temperature profiles. Finally we compare this study's K_{sp-dol} model, and derived thermodynamic properties, with prior studies.

Comparison to the Möller and De Lucia (2020) meta-analysis.— The largest previous meta-/regression analysis of groundwater $\log_{10}({}^{a}Ca^{2+}/{}^{a}Mg^{2+})$ values is that of Möller and De Lucia (2020) who consider 242 samples from 17 regions around the world. They similarly find these fluids have $\log_{10}({}^{a}Ca^{2+}/{}^{a}Mg^{2+})$ values that are intermediate with respect to the SUPCRT92-filter. However, for the majority of data subsets they observe $\log_{10}({}^{a}Ca^{2+}/{}^{a}Mg^{2+})$-temperature profiles to be non-parallel to the SUPCRT92 calcite-dolomite equilibria suggesting this indicates buffering by Mg-calcite surface phases. Möller and De Lucia (2020) also recognise that a minority of samples have $\log_{10}({}^{a}Ca^{2+}/{}^{a}Mg^{2+})$-temperature profiles parallel to the SUPCRT92 calcite-dolomite equilibria. These include datasets from the Red Sea, Meizar Wells/Yarmouk Gorge (Israel/Jordan), and the MSD basin. Nevertheless the presence of calcite-dolomite equilibrium is discounted, with an alternative interpretation for these sites invoking unspecified differences in environmental conditions and chemical reactions. The MSD basin dataset is from Kharaka and others (1987) and our expanded analysis of Test Area B samples arguably strengthens an interpretation of calcite-dolomite equilibrium.

The Meizar Wells/Yarmouk gorge dataset is from Siebert and others (2014) and Siebert and others (in prep). The dominant lithology in the Yarmouk gorge is limestone and, though Siebert and others (2014) mention that limestones are altered and interpret calcite-dolomite equilibrium for springs at the Shamir Artesian location, diagenetic information for the local carbonate aquifers is limited. Most wells in the Siebert and others (2014) database appear to sample the Turonian-Cenomanian Ajloun group, which further south is described as primarily being composed of fine-grained dolomitized shallow/restricted marine mudstone/wackestones (Khalifa and Abed, 2010). Locally, dolomitization is identified (well Mukheibeh 4) in the upper part of the Ajloun group (Inbar and others, 2019). Evaluating the Meizar Wells/Yarmouk gorge dataset the $\log_{10}({}^{a}Ca^{2+}/{}^{a}Mg^{2+})$-temperature profile does appear to be consistent with calcite-dolomite equilibrium (fig. 9f). However, samples with temperatures < 25°C have scattered $\log_{10}({}^{a}Ca^{2+}/{}^{a}Mg^{2+})$ values. For simple 2-term (Maier-Kelly) linear models including samples < 25°C the R^2 is 0.05 and the p-value is 0.08 (model L1; n = 42) whilst removing six < 25°C samples results in an improvement in goodness of fit measurements with the R^2 rising to 0.38 and the p-value falling to 4.23×10^{-5}(model M1; n = 36). Unlike model L1, model M1 accounts for much of the variation in the dataset (high R^2) and is significant (low p-value).

Generally there is a divide in the Möller and De Lucia (2020) dataset whereby regional subsets with sample temperatures > 30°C have $\log_{10}({}^{a}Ca^{2+}/{}^{a}Mg^{2+})$-temperature trends largely parallel to the SUPCRT92 calcite-dolomite equilibria, whilst those with temperatures < 30°C are non-parallel. Only 22% of the samples (n = 54) in the Möller and De Lucia (2020) dataset have recorded depths, with the majority derived from surface springs. This is reflected in a mean sample temperature of 32°C (σ = 24°C) which is substantially lower than the 62°C (σ = 29°C) mean of PWGD at-formation-depth temperatures.

In contrast to this study, Möller and De Lucia (2020) utilise the recorded sample temperature and do not thoroughly evaluate the temperature at-formation-depth. For example, for the North East German basin Möller and De Lucia (2020) determine $\log_{10}({}^{a}Ca^{2+}/{}^{a}Mg^{2+})$ values

for samples from Tesmer and others (2007). However we find a significant number of temperatures from Tesmer and others (2007) to be anomalous when compared against a representative geothermal model comprised of a linear geothermal gradient of 32°C/km (Agemar and other, 2012) and an average surface temperature of 4°C (supplementary figure 2). An exemplar anomaly is from the Rheisberg well where the $\log_{10}({}^{a}Ca^{2+}/{}^{a}Mg^{2+})$ is determined at 16.6°C for a sample taken from 1600 m which seems improbably low. Inaccurate equilibrium temperatures have a minimal effect on the calculated $\log_{10}({}^{a}Ca^{2+}/{}^{a}Mg^{2+})$ values, as these are primarily dependent on the solution composition, but are extremely consequential when contextualising $\log_{10}({}^{a}Ca^{2+}/{}^{a}Mg^{2+})$ values to interpret calcite-dolomite equilibrium.

In contrast, sample temperatures from Hyeong and Capuano (2001) and this study's geothermal model appear to be reliable. Specifically Hyeong and Capuano (2001) measure temperatures at the well perforation during the formation shut in test or, lacking that data, derive temperatures from corrected well log measurements. All borehole data is interpreted to have a good control on the sample depth, which is by extension assumed to be the depth at which equilibrium is established.

The samples in the Möller and De Lucia (2020) meta-analysis are derived from both surface springs and boreholes which have separate methods of estimating/observing at-formation-depth temperatures. For spring water samples, where the equilibrium temperature is less well known, prior analyses have adopted a geothermometrical approach as exemplified by Chiodini and others (1995), Vespasiano and others (2014), and Blasco and others (2018) (supplementary table 2). These studies have evaluated the equilibrium temperature and dolomite order using both isotope data and compositional analysis with respect to multiple reference minerals (such as calcite, dolomite, anhydrite and quartz).

There is a strong similarity (fig. 5b) between the reference model (model J21) $\log_{10}({}^{a}Ca^{2+}/{}^{a}Mg^{2+})$-temperature profile and prior globally distributed groundwater (borehole and spring water) observations (Hsu, 1963; Hyeong and Capuano, 2001; Vespasiano and others, 2014; Blasco and others, 2018). This supports both the study methodology and a widespread applicability of the reference models J21 and J23. Notably the difference between model J21 and the spring water studies of Vespasiano and others (2014) and Blasco and others (2018) are remarkably small at 0.01 and 0.05 log unit respectively. Using model J21 as the reference geothermometer for the Vespasiano and others (2014) and Blasco and others (2018) observations we find the equilibrium temperatures to be 71±72°C and 101±72°C respectively; note the very wide uncertainties reflect the confidence intervals of model J21. For Blasco and others (2018) the new estimate agrees well with their equilibrium temperature estimate (93±14°C) derived using CO_2 degassing reconstruction highlighting a potential for $\log_{10}({}^{a}Ca^{2+}/{}^{a}Mg^{2+})$ values/model J21 to be used as a geothermometer.

Sources of Local Effects

We further evaluate the mechanisms that could control $\log_{10}({}^{a}Ca^{2+}/{}^{a}Mg^{2+})$-temperature profiles both at a local and more global scales. This includes the presence of any common ion equilibria, kinetic effects, *I*, the solution composition, composition of the equilibrium calcite and dolomite phases, and conceivable sources of error.

A) Equilibrium with additional minerals.— The addition of any other minerals bearing Ca, Mg or CO_3 could conceivably generate substantial changes to the solubility of either calcite or dolomite due to the common-ion effect. For the common ion effect to be of significant concern the additional mineral must have a solubility somewhat comparable to either calcite or dolomite.

The illitization of smectite and albitization of feldspar, processes which release Mg and Ca respectively, have been variably discounted as significant in modifying $\log_{10}({}^{a}Ca^{2+}/{}^{a}Mg^{2+})$ values by both Hyeong and Capuano (2001) and Kharaka and others (1987). Specifically, at diagenetic temperatures these processes are irreversible and, therefore, cannot buffer $\log_{10}({}^{a}Ca^{2+}/{}^{a}Mg^{2+})$ values. The addition of Mg or Ca to the solution through illitization or albitization should therefore be buffered by calcite-dolomite equilibrium maintaining a constant $\log_{10}({}^{a}Ca^{2+}/{}^{a}Mg^{2+})$. Furthermore, as neither illite, smectite, albite or anorthite are very soluble, there is a negligible common ion effect.

Chlorite group minerals such as clinochlore ($Mg_5Al_2Si_3O_{10}(OH)_8$) are more soluble. However, Hyeong and Capuano (2001) conclude chlorite is unlikely to be a significant buffer in Frio Fm. sediments as, though chlorite is abundant, it is only found in samples with at-formation-depth temperatures >90°C and there is no divergence in $\log_{10}({}^{a}Ca^{2+}/{}^{a}Mg^{2+})$ values above and below 90°C. Nevertheless to evaluate the common ion effect we have simulated the solubility of various chlorite group members at 25, 50, 75 and 150°C using PHREEQC with the LLNL and the Thermoddem (Blanc and others, 2012) databases for 0.1 mol/kgw NaCl buffered solutions in equilibrium with both calcite and dolomite. Hereafter, unless otherwise stated, we model dolomite in PHREEQC using model J23. Clinochlore is present in both the Thermoddem and the LLNL database, but the latter contains two separate variants, clinochlore-14A and clinochlore-7A, which have identical formulae but slightly different solubility constants. The phase clinochlore-14A was determined to be broadly similar in solubility to chlorite from Flagstaff Hill, California termed 'Chlorite (CCa-2)' (Zhang and others, 2015). Thermoddem also includes the chlorite mineral sudoite ($Mg_2Al_4Si_3O_{10}(OH)_8$).

In solutions buffered solely by calcite and dolomite, all of the aforementioned chlorite phases are very insoluble. For the most soluble chlorite phase, sudoite, each kg of water dissolves 1.056×10^{-4} moles of calcite, 1.062×10^{-4} moles of dolomite, and just 2.095×10^{-7} moles of sudoite at 25°C (at higher temperatures sudoite is also relatively insoluble compared to calcite and dolomite). In the absence of sudoite the amounts of calcite (1.051×10^{-4} moles) and dolomite (1.065×10^{-4} moles) that dissolve are similar and this explains the constant $\log_{10}({}^{a}Ca^{2+}/{}^{a}Mg^{2+})$ of 0.31 log unit for both simulations with and without sudoite.

Ca-sulphates such as anhydrite ($CaSO_4$) are common in the subsurface and more soluble than either calcite or dolomite and thus potentially could affect $\log_{10}({}^{a}Ca^{2+}/{}^{a}Mg^{2+})$. Again, we evaluate equilibrium conditions at 25, 50, 75 and 150°C using PHREEQC with the Thermoddem database in a 0.1 mol/kgw NaCl buffered solution. At 25°C, for every kg of water 1.205×10^{-2} moles of dolomite and 3.775×10^{-2} moles of anhydrite dissolve. Meanwhile 2.407×10^{-2} moles of calcite precipitate due to the common ion effect as anhydrite is more soluble. However $\log_{10}({}^{a}Ca^{2+}/{}^{a}Mg^{2+})$ values remain at

0.31, which suggests that the common ion effect has no impact on the ability of calcite-dolomite equilibrium to buffer $\log_{10}({}^{a}Ca^{2+}/{}^{a}Mg^{2+})$.

Cation exchange with mixed-layer illite/smectite could also buffer $\log_{10}({}^{a}Ca^{2+}/{}^{a}Mg^{2+})$. Hyeong and Capuano (2001), though noting the presence of mixed-layer illite/smectite, dismiss this geochemical process modifying $\log_{10}({}^{a}Ca^{2+}/{}^{a}Mg^{2+})$ in the Frio Fm.. However, Dutton (1987) and Engle and Blondes (2014) suggest that the variable release of Ca^{2+} and Mg^{2+} ions, as Na^{+} is adsorbed, is a key mechanism modifying brines in the San Andres Fm. of the Permian basin and results in low $[Na^{+}]/[Cl^{-}]$ values. Variation in the clay composition results in differences in the release Ca^{2+} and Mg^{2+} and could therefore buffer $\log_{10}({}^{a}Ca^{2+}/{}^{a}Mg^{2+})$ values to a wide range. However whilst this process is challenging to model using thermodynamic codes the main argument against clay minerals buffering $\log_{10}({}^{a}Ca^{2+}/{}^{a}Mg^{2+})$ values is similar to that given for illitization/albitization; there appears to be a unidirectionality in clay mineral ion exchange as the binding energies and ion sites for Na^{+}, Mg^{2+} and Ca^{2+} are different (Underwood and others, 2016).

B) Kinetic considerations and approach to equilibrium.— The approach to calcite-dolomite equilibrium from either conditions of supersaturation or undersaturation results in $\log_{10}({}^{a}Ca^{2+}/{}^{a}Mg^{2+})$ values varying in a quasi-static equilibrium distribution (Hefter and Tomkins, 2003). The distribution/scatter of $\log_{10}({}^{a}Ca^{2+}/{}^{a}Mg^{2+})$ values primarily reflects the balance between disequilibrium, kinetics and the groundwater residence time.

The systematic positive skew observed in the PWGD dataset (fig. 10e) could indicate that equilibrium is more frequently approached from conditions of dolomite undersaturation. This may reflect a systematic decrease in equilibrium temperatures during basin uplift. As temperature increases during burial, to maintain calcite-dolomite equilibrium $\log_{10}({}^{a}Ca^{2+}/{}^{a}Mg^{2+})$ increase and this, being a function of K_{sp-dol} and K_{sp-cal}, typically corresponds to dolomitization. Peak burial temperatures correspond to a peak dolomite abundance. Thereafter, during uplift a decrease in at-formation-depth temperatures necessitates lower equilibrium $\log_{10}({}^{a}Ca^{2+}/{}^{a}Mg^{2+})$ values and subsequently dedolomitization (dolomite dissolution and calcite precipitation) occurs.

C) Ionic strength\solution composition.— We evaluate calcite-dolomite equilibrium for a range of *I* and in both monovalent (NaCl) and divalent (Na_2SO_4) background electrolytes (fig. 11). An increase in the background *I* (either NaCl or Na_2SO_4) up to ~2.5 mol/kgw drives additional dissolution of calcite and dolomite so increasing $[Ca^{2+}]$ and $[Mg^{2+}]$. At $I > 2.5$ mol/kgw, values of $[Ca^{2+}]$ and $[Mg^{2+}]$ decrease as less calcite and dolomite dissolve.

Both ${}^{a}Ca^{2+}$ and ${}^{a}Mg^{2+}$ increase linearly throughout the range of ionic strengths and background electrolytes evaluated. The linearity is due to calcite-dolomite equilibrium buffering $\log_{10}({}^{a}Ca^{2+}/{}^{a}Mg^{2+})$ to a constant value. The increase in activities reflects 1) variations in $[Ca^{2+}]$ and $[Mg^{2+}]$ due to dissolution and 2) activity coefficients for Ca^{2+} and Mg^{2+} are not constant and change with *I* which, in particular, leads to ${}^{a}Ca^{2+}$ and ${}^{a}Mg^{2+}$ increasing with *I* above 2.5 mol/kgw. Moreover, variations in $[Ca^{2+}]$ and $[Mg^{2+}]$ also reflect that activity coefficients for Ca^{2+} and Mg^{2+} are not identical in the Pitzer model which is primarily a result of different Pauling ionic radii; 72pm for Mg^{2+} and 100pm for Ca^{2+} (Ulfsbo and others, 2015).

We find support for the interpretation that $\log_{10}({}^{a}Ca^{2+}/{}^{a}Mg^{2+})$ values at calcite-dolomite equilibrium are largely insensitive to both *I* and solution composition. Baker and Kastner (1981), also referencing the experimental data of Rosenberg and Holland (1964), observe the calcite-dolomite equilibrium $[Ca^{2+}]/[Mg^{2+}]$ value increases with *I* though we suggest this is consistent with a constant $\log_{10}({}^{a}Ca^{2+}/{}^{a}Mg^{2+})$ value (fig. 11). Noting identical *I* values, when comparing brines in the Edwards group and the Smackover Fm. Hyeong and Capuano (2001) attributed substantially different $\log_{10}({}^{a}Ca^{2+}/{}^{a}Mg^{2+})$ values to variations in dolomite order. Moreover, Hyeong and Capuano (2001) observe different TDS profiles for both the Chocolate/Halls Bayou (from 33g/L to 132g/L) and West Columbia (from 61g/L to 99g/L) fields yet note similar $\log_{10}({}^{a}Ca^{2+}/{}^{a}Mg^{2+})$-temperature profiles suggesting no influence from *I*.

We modify the reference model J21 to additionally include *I* as a fixed effect such that the Maier-Kelly formula of (only) the fixed effect terms is;

$$\log_{10}\left(\frac{{}^{a}Ca^{2+}}{{}^{a}Mg^{2+}}\right) = a + bT + \frac{c}{T} + I \tag{25}$$

This model (J22) determines there to be a 0.007 log unit decrease in $\log_{10}({}^{a}Ca^{2+}/{}^{a}Mg^{2+})$ values per 1 mol/kgw increase in *I*. AIC finds some support (model J22; -3600) for this model in comparison to the reference model (model J21; -3595). The minimal AIC difference confirms the negligible thermodynamic effect of *I* on $\log_{10}({}^{a}Ca^{2+}/{}^{a}Mg^{2+})$ at calcite-dolomite equilibrium and therefore model J22 is not a reference model. Baker and Kastner (1981) note slower rates of dolomitization at lower *I* therefore the slight decrease in $\log_{10}({}^{a}Ca^{2+}/{}^{a}Mg^{2+})$ with increasing *I* may reflect a kinetic effect inhibiting attainment of equilibrium. Alternatively Kaczmarek and Sibley (2011) observe variations in the dolomite ordering/composition depending on the initial solution composition suggesting the dolomite phase in equilibrium with the solution reflects the *I*.

D) Error.—There is a component of random measurement error which is assumed to be normally distributed and incorporated into a formulation of the mixed model by the error term, ε, and thus is of little further interest. Systematic errors are of more concern and there are several potential sources.

Errors in the geothermal model for calculating at-formation-depth temperatures could increase $\log_{10}({}^{a}Ca^{2+}/{}^{a}Mg^{2+})$ scatter. However extensive ground truthing benchmarked this study's geothermal model at a local scale (fig. 8) and as the majority of PWGD and SMUH samples come from similar areas (producing basins, fig. 6) at the continental scale we interpret the calculated at-formation-depth temperatures for the majority of PWGD samples to be reliable.

There is no weighting in the model for samples taken earlier in the production history which may reflect compositions closer to the unperturbed groundwater composition. The injection of water to stimulate hydrocarbon production (waterflooding) from sources other than recycled water from the formation of interest - such as oceans, rivers or separate aquifers - may result in a calcite-dolomite disequilibrium. Similarly injection of CO_2 or other gases/liquids for reservoir stimulation may result in calcite-dolomite disequilibrium and effect the solubility of other minerals such as chlorite. Han and others (2010) document

changes to the fluid composition and the saturation indices of calcite (SI = 0.80 → 0.62) and dolomite (SI = 2.55 → 2.44) as production shifts from the waterflooding to the CO_2 injection production phases in the Cisco and Canyon formations of the Scurry Area Canyon Reef Operations Committee (SACROC) Unit in the Midland basin, Texas. It is unclear how much variation in $\log_{10}({}^{a}Ca^{2+}/{}^{a}Mg^{2+})$ could be attributed to production influences, though Engle and Blondes (2014) offer a solution that could potentially be used to filter samples through the use of principal component analysis.

Another potential error source relates to the evaluation of activities by PHREEQC-Pitzer. We suggest that at least between 43 – 150°C PHREEQC-Pitzer produces reliable $\log_{10}({}^{a}Ca^{2+}/{}^{a}Mg^{2+})$ values similar to those determined by the Hyeong and Capuano (2001) SOLMINEQ88-Pitzer analysis (supplementary figure 1).

E) Composition of the dolomite and calcite phase.— Modelling the solubility of LMC (0 – 300°C) we find a minimal effect on equilibrium $\log_{10}({}^{a}Ca^{2+}/{}^{a}Mg^{2+})$ values (fig. 5b). In comparison to the value of $pK_{sp°\text{-cal}}$, the $pK_{sp°\text{-cal}(4\%MgCO_3)}$ for a LMC phase consisting of 4% $MgCO_3$ (upper bound of LMC) that results from ideal mixing between calcite and magnesite (eq 17; table 2) is +0.018 log unit higher. A +0.018 log unit increase in the value of $pK_{sp°\text{-cal}(4\%MgCO_3)}$ results in an increase of +0.036 log unit in the equilibrium $\log_{10}({}^{a}Ca^{2+}/{}^{a}Mg^{2+})$ value (eq 8) and by extension an identical increase in any estimated value for $pK_{sp°-dol}$. For reference, 0.036 log unit is an order of magnitude smaller than the uncertainty associated with the reference model J21 ($pK_{sp°-dol}$ = -17.27±0.35). This suggests that slight variations in the Mg-composition of the equilibrium calcite phase are unlikely to significantly inhibit the determination of K_{sp-dol}.

A more realistic non-ideal Mg-calcite model would result in increases in both the estimated solubility of the Mg-calcite phase and, by extension, the equilibrium $\log_{10}({}^{a}Ca^{2+}/{}^{a}Mg^{2+})$ value. The determination of the thermodynamic properties of non-ideal Mg-calcite across a wide range of temperatures is desirable (though complex). However, at 73°C $K_{sp°-cal} \equiv K_{sp°-mag} \equiv K_{sp°\text{-cal}(4\%MgCO_3)}$ and non-ideal behaviour should approach a minimum (fig. 5b). Moreover, at temperatures 50°C ≤ T ≤ 100°C endmember solubilities are similar and at low (T < 73°C) and high (T > 73°C) temperatures, for a pure calcite end-member assumption, the calculated $pK_{sp°-dol}$ values would be slight under- and over-estimates respectively. As the 25th and 75th percentiles of the at-formation-depth temperatures are 40°C and 79°C respectively (supplementary table. 5) it seems reasonable to determine $K_{sp°-dol}$ assuming a pure calcite end-member.

Were Ca substitution into dolomite ideal, for a 2% $CaCO_3$ dolomite the reference model (model J23) $pK_{sp°-dol}$ would change from -17.27 to -17.10 which translates to a substantial identical change (-0.17) in the calcite-dolomite equilibrium $\log_{10}({}^{a}Ca^{2+}/{}^{a}Mg^{2+})$ values (fig. 5b). The effect on equilibrium $\log_{10}({}^{a}Ca^{2+}/{}^{a}Mg^{2+})$ values is clearly 1) substantially larger in magnitude than that associated with Mg substitution into calcite and 2) on the same scale estimated for substitutional order in dolomite.

Local effects summary.— Whilst acknowledging the potential minor contributions to $\log_{10}({}^{a}Ca^{2+}/{}^{a}Mg^{2+})$ values from sources reviewed above (and sources presently unknown), we suggest the equilibrium dolomite composition is the most significant cause of

variations in $\log_{10}({}^{a}Ca^{2+}/{}^{a}Mg^{2+})$ values. The future challenges for this interpretation are reconciling and correlating the frequency distributions and petrogenesis of natural dolomite compositions (Sperber and others, 1984) with $\log_{10}({}^{a}Ca^{2+}/{}^{a}Mg^{2+})$ values.

Mixed Model Global Level Analysis

The reference model (model J21) $\log_{10}({}^{a}Ca^{2+}/{}^{a}Mg^{2+})$-temperature profile appears broadly consistent with prior K_{sp-dol} models (fig. 5b). Here we contextualise our results relative to prior studies and discuss derived thermodynamic parameters. In this section we also consider the limitations of mixed models and uncertainty estimates.

Literature Comparison.— The study of Bénézeth and others (2018) represents the most recent experimental study that utilizes the widest experimental range of temperatures (53 – 253°C) and approaches K_{sp-dol} from conditions of both under- and super-saturation. At reference state conditions (25°C) the $pK_{sp°-dol}$ value of -17.27±0.35 from the reference model (model J23) is comparable to the -17.19±0.3 of Bénézeth and others (2018). However, at temperatures > 50°C the models diverge (fig. 5a) until at 200ºC the Bénézeth and others (2018) model has a pK_{sp-dol} of -24.02 which is much lower than both the reference model and also the ordered dolomite phase of Helgeson and others (1978), which have pK_{sp-dol} values of -23.26 and -23.71 respectively at 200ºC. As the divergence becomes more significant at higher temperatures where dolomite solubility is lower (though achieved quicker) we suggest the accurate measurement of these equilibrium solutions with lower $[Ca^{2+}]$, $[Mg^{2+}]$ and $[CO_3^{2-}]$ values maybe more prone to error. Moreover, Bénézeth and others (2018) do not leverage the benefits in terms of accurately calculating activities in solution through the use of a thermodynamic program. Möller and De Lucia (2020) re-evaluate the Bénézeth and others (2018) dataset using PHREEQC and determine the pK_{sp-dol} at 200ºC to be either -24.7 (llnl.dat) or -25.5 (pitzer.dat) which, they argue, reflects buffering by Mg-surface phases. In summary the calcite-dolomite equilibrium $\log_{10}({}^{a}Ca^{2+}/{}^{a}Mg^{2+})$ values generated by the Bénézeth and others (2018) model appear to be spurious in comparison to other profiles (fig. 5a) and a poor fit for the PWGD $\log_{10}({}^{a}Ca^{2+}/{}^{a}Mg^{2+})$ distribution. Furthermore the plausible re-evaluation by Möller and De Lucia (2020) results in an even more insoluble K_{sp-dol} model suggesting additional reliability issues.

As previously discussed, the consistency between the various global groundwater observations/K_{sp-dol} models including this study suggests a commonality of calcite-dolomite equilibrium in groundwaters. By extension we suggest this increases the reliability of K_{sp-dol} models generated using the groundwater approach.

Partial pooling issues.— The partial-pooling approach which we have advocated for as an optimal compromise between the complete- and no-pooling extremes has an inherent flaw. Mixed modelling weights groups based on sample sizes, with greater confidence in group-level effects for groups with larger numbers of samples. This has two significant effects which we exemplify using Test Area A and the Hastings field (a representative field within Test Area A);

1) The population average (global-level intercept and gradient) is heavily influenced by larger groups. As increasing amounts of high $\log_{10}({}^{a}Ca^{2+}/{}^{a}Mg^{2+})$ data is added to a

mixed model the global-level $\log_{10}({}^{a}Ca^{2+}/{}^{a}Mg^{2+})$ intercept increases. This is most notable when comparing the F1 (n = 21) and G1 (n = 117) models (fig. 9d). Model F1 contains Frio Fm. samples only from Test Area A that typically have low $\log_{10}({}^{a}Ca^{2+}/{}^{a}Mg^{2+})$ values (model F1; $\log_{10}({}^{a}Ca^{2+}/{}^{a}Mg^{2+})$ = -0.01 at 25°C). As previously discussed Frio Fm. samples outside of Test Area A often have high $\log_{10}({}^{a}Ca^{2+}/{}^{a}Mg^{2+})$ values and the model of all Frio Fm. samples (model G1) has a $\log_{10}({}^{a}Ca^{2+}/{}^{a}Mg^{2+})$ value of 0.48 log unit at 25°C which is significantly higher than model F1.

2) A more significant issue is that RI values for small groups that are significantly different to the rest of the population will tend closer towards the global-level intercept as the population size increases. Samples from the Hastings field (n = 4; T = 73 – 76°C) are all from the Frio Fm. and have $\log_{10}({}^{a}Ca^{2+}/{}^{a}Mg^{2+})$ values consistent with other fields in Test Area A (fig. 9d). The Test Area A model (model F1), Frio Fm. model (model G1), and the reference model (model J21) contain progressively larger number of samples in addition to those from the Hastings field/Test Area A. The group-level RI values for the Hastings field increase as the overall model population size increases with RI values of 0.00, 0.21, and 0.23 for F1, G1 and J21 models respectively (fig. 9d). The reference model (model J21) RI value for the Hastings field is one of the lowest values for all fields in the PWGD (RI = -1.98; 2149th lowest RI value out of 2167 fields) though the difference to the global-intercept is only 0.07. Ranked RI values are interpreted to be useful as a comparative tool, highlighting potentially significant variations away from the population average, though we urge caution using RI values to construct models for individual groups as the significance of the variation can be minimised. Future work could implement a Bayesian framework that better preserves information for small sample size groups.

Mixed model uncertainty.— Bénézeth and others (2018) determine an uncertainty (3σ/99.7% confidence interval) for their K_{sp-dol} model ($pK_{sp^\circ-dol}$ = -17.19±0.3) through combining experimental uncertainties. Whilst this method may indicate the uncertainty ascribed to an individual measurement of K_{sp-dol}, it reflects neither the uncertainty determined by the statistical model used to perform the Maier-Kelly regression nor the uncertainty of any extrapolation.

The lowest experimental temperature used by Bénézeth and others (2018) is 53°C, yet the uncertainty for $pK_{sp^\circ-dol}$ at 25°C is reported as ±0.3 without any apparent evaluation of the uncertainty associated with extrapolation outside of the experimental range. We model the Bénézeth and others (2018) dataset, specifically the activities given in Bénézeth and others (2018) and not those later determined by Möller and De Lucia (2020), using a 3-term linear model (N1) with uncertainty evaluated using 2σ/95% confidence intervals (identical to reference model J21). At 25°C the $pK_{sp^\circ-dol}$ for model N1 is -17.18±0.53 whilst at 100°C, and generally for values within the experimental range, the pK_{sp-dol} is -19.50±0.15 (fig. 5a). Clearly the extrapolated uncertainty to reference state conditions is significantly greater than that given by Bénézeth and others (2018) and were the uncertainty evaluated at the 3σ/99.7% confidence interval level the uncertainty estimate would be even larger. We suggest that the $pK_{sp^\circ-dol}$ determined here using groundwater data can broadly be considered to be at least no less uncertain than that derived by prior experimental data.

Thermodynamic properties of reference dolomite model.— For the three-term Maier-Kelly formula (eq 19) the *a*, *b* and *c* coefficients can be converted into the ΔG_r°, ΔH_r° and $\Delta C_{p,\mathrm{r}}^\circ$ thermodynamic properties of dolomite as follows (Bénézeth and others, 2018);

$$\Delta G_r^\circ = -R\ln(10)\,(aT + bT^2 + c) \tag{26}$$

$$\Delta H_r^\circ = R\,T\,\ln(10)\,(bT^2 - c) \tag{27}$$

$$\Delta C_{p,\mathrm{r}}^\circ = 2R\,T\,\ln(10)\,b \tag{28}$$

For model J23 the coefficients *a*, *b*, and *c* have values of 1.47545×10^{1}, -6.24959×10^{-2}, and -3.99350×10^{3} respectively, which equate to values of ΔG_f°, ΔH_r°, and $C_{p,\mathrm{r}}^\circ$ of -2161.34 ± 8.26 kJ mol^{-1}, -2329.61 ± 0.51 kJ mol^{-1}, and 82.04 ± 12.17 J mol^{-1}K^{-1} respectively. These values of ΔG_r° and ΔH_r° are broadly comparable to prior estimations (supplementary table 2); ΔG_r° ranges from -2147.82 ± 2.20 kJ mol^{-1}(Rock and others, 2001) to -2171.75 kJ mol^{-1} (Blasco and others, 2018) whilst ΔH_r° ranges from -2315.89 kJ mol^{-1} (Morrow and others, 1994) to -2332 ± 3 kJ mol^{-1} (Chai and Navrotsky, 1993). However, the $C_{p,\mathrm{r}}^\circ$ value is substantially lower than the literature estimates that range from 154.2 ± 2 J mol^{-1}K^{-1} (Bénézeth and others, 2018) to 157.74 J mol^{-1}K^{-1} (Johnson and others, 1992).

A single inaccurate thermodynamic property, in particular the $C_{p,\mathrm{r}}^\circ$, does not render other parameters to be in error. Following the method of Bénézeth and others (2018) $C_{p,\mathrm{r}}^\circ$ can be fixed to a constant value and the model refitted; for a $C_{p,\mathrm{r}}^\circ$ value of 157.51 J mol^{-1}K^{-1} (Robie and Hemingway, 1995) we set the *b* coefficient to a value of -0.06919. This refitted model (model J24) determines the *a* and *c* coefficients to be 1.93×10^{1} and -4.75×10^{3} respectively; these values equate to minor shifts in the values of ΔG_r° and ΔH_r° to -2161.4 ± 0.66 kJ mol^{-1} and -2332.67 ± 0.34 respectively. Moreover between 25 – 150°C there is a minimal difference (fig. 5a) between the reference model J23 and model J24, with the greatest divergence primarily occurring at temperatures > 230°C where PWGD data is limited (fig. 9a). The minor difference between these models is because $C_{p,r}^\circ$, unlike ΔG_r° and ΔH_r°, is extremely sensitive to the $\log_{10}({}^{a}\mathrm{Ca}^{2+}/{}^{a}\mathrm{Mg}^{2+})$ - temperature gradient. The use of single field data, some of which show steep increases of $\log_{10}({}^{a}\mathrm{Ca}^{2+}/{}^{a}\mathrm{Mg}^{2+})$ with temperature, may be able to more accurately evaluate $C_{p,r}^\circ$ though the inclusion criteria requires careful justification to avoid a selection bias.

CONCLUSIONS

This regression analysis of the PWGD reconstructs at-formation-depth temperatures for each sample (n=11,480) using a new geothermal model that combines subsurface geothermal gradients and mean annual land surface temperature measurements. After screening to ensure quality, the $\log_{10}({}^{a}\mathrm{Ca}^{2+}/{}^{a}\mathrm{Mg}^{2+})$ of each sample was evaluated using PHREEQC with the Pitzer database.

- Ground truthing at-formation-depth temperatures and $\log_{10}({}^{a}Ca^{2+}/{}^{a}Mg^{2+})$ values to areas of the Texas Gulf Coast basin (Test Area A) and Mississippi Salt Dome basin (Test Area B) we find both are consistent with prior studies suggesting both the new geothermal model and PWGD dataset are reliable data sources.
- The $\log_{10}({}^{a}Ca^{2+}/{}^{a}Mg^{2+})$-temperature relationship of the majority (90%) of subsurface waters in the US are interpreted to be indicative of calcite-dolomite equilibrium, suggesting this is likely also true globally.
- Equilibria with bulk calcite and dolomite mineral compositions, rather than Mg-calcite surface phases or other conceivable mechanisms (e.g. albitization), is thought to be the primary control on $\log_{10}({}^{a}Ca^{2+}/{}^{a}Mg^{2+})$ values. Deviations in $\log_{10}({}^{a}Ca^{2+}/{}^{a}Mg^{2+})$ values are interpreted to primarily reflect variations in the composition of the bulk equilibrium dolomite phase.

For the subset of PWGD samples (90%; n=10,343/11,480) with $\log_{10}({}^{a}Ca^{2+}/{}^{a}Mg^{2+})$ values intermediate with respect to the SUPCRT92-filter and interpreted to most likely be at calcite-dolomite equilibrium mixed models were generated including the reference models J21 and J23. These mixed models report 1) fixed effect coefficients, which describe the $\log_{10}({}^{a}Ca^{2+}/{}^{a}Mg^{2+})$ (model J21) and K_{sp-dol} (model J23) intercept and temperature dependence for the global average dolomite composition and 2) group-level RI values that describe the deviation away from the global average. RI values may offer a novel route for evaluating the stoichiometry of subsurface dolomites. Both the observed $\log_{10}({}^{a}Ca^{2+}/{}^{a}Mg^{2+})$ values and the derived K_{sp-dol} models reported here compare well with prior experimentally derived data and groundwater observations.

Supplementary information: There two supplementary figures and 7 supplementary tables. Supplementary table 7 is an excel workbook comprised of the group RI results for the reference models J21 and J23. A minimum working example of the workflow (amongst other archival results) can be found at the following GitHub repository: https://github.com/hammytheham/AJS_Robertson_2022 . The new geothermal model, which has been modified to generate local data, can be found at www.co2-gasp.com .

Acknowledgements: We are grateful for advice from Dan Mirron and Dmitri Kulik. Thank you also to the two anonymous reviewers for constructive feedback. This study was funded by Woodside Petroleum, Wintershall Petroleum and Tullow Oil.

References

Agemar, T., Schellschmidt, R. and Schulz, R., 2012. Subsurface temperature distribution in Germany. *Geothermics*, *44*, pp.65-77.

Aines, R.D., Wolery, T.J., Bourcier, W.L., Wolfe, T. and Hausmann, C., 2011. Fresh water generation from aquifer-pressured carbon storage: feasibility of treating saline formation waters: *Energy Procedia*, v. *4*, p. 2269-2276.

Althoff, P.L., 1977. Structural refinements of dolomite and a magnesian calcite and implications for dolomite formation in the marine environment: *American Mineralogist*, v. *62*(7-8), p. 772-783.

Al-Helal, A.B., Whitaker, F.F. and Xiao, Y., 2012. Reactive transport modeling of brine reflux: dolomitization, anhydrite precipitation, and porosity evolution. *Journal of Sedimentary Research*, *82*(3), pp.196-215.

Ambrose, W.A., Grigsby, J.D., Hardage, B.A., Langford, R.P., Jirik, L.A., Levey, R.A., Collins, R.E., Sippel, M., Howard, W.E. and Vidal, J., 1992. *Secondary gas recovery: targeted technology applications for infield reserve growth in fluvial reservoirs in the Frio Formation, Seeligson field, South Texas. The University of Texas at Austin, Bureau of Economic Geology*. Topical Report GRI-92/0244, Gas Research Institute, Chicago, Illinois.

Anderson, G.M. and Crerar, D.A., 1993. *Thermodynamics in geochemistry: the equilibrium model*. Oxford University Press on Demand.

André, L., Audigane, P., Azaroual, M. and Menjoz, A., 2007. Numerical modeling of fluid-rock chemical interactions at the supercritical CO2-liquid interface during CO2 injection into a carbonate reservoir, the Dogger aquifer (Paris Basin, France): *Energy Conversion and Management*, v. *48*(6), p. 1782-1797.

Antao, S.M., Mulder, W.H., Hassan, I., Crichton, W.A. and Parise, J.B., 2004. Cation disorder in dolomite, CaMg (CO3) 2, and its influence on the aragonite+ magnesite↔ dolomite reaction boundary: *American Mineralogist*, v. *89*(7), p. 1142-1147.

Baker, P.A. and Kastner, M., 1981. Constraints on the formation of sedimentary dolomite: *Science*, v. *213*(4504), p. 214-216.

Barin, I., 1989. Thermochemical data of pure substances. New York, *VCH Publishers*.

Barin, I., 1995. Thermochemical data of pure substances Third Edition. New York, *VCH Publishers*.

Barnes, I. and Back, W. (1964) Dolomite solubility in ground water: *U.S. Geological Survey Prof. Paper 475-D, v.* 160, p. 179–180.

Bates, D., Maechler, M., Bolker, B. and Walker, S., 2014. lme4: Linear mixed-effects models using Eigen and S4: R package version 1.1-7, p. 1-23.

Bechtel, B., 2015. A new global climatology of annual land surface temperature: *Remote Sensing*, v. *7*(3), p. 2850-2870.

Beckman, J.D. and Williamson, A.K., 1990. *Salt-dome locations in the Gulf Coastal Plain, south-central United States* (Vol. 90, No. 4060). US Geological Survey.

Bell, B.A., Morgan, G.B., Schoeneberger, J.A., Loudermilk, B.L., Kromrey, J.D. and Ferron, J.M., 2010, April. Dancing the sample size limbo with mixed models: How low can you go: *SAS Global Forum,* v. 4, p. 11-14.

Bénézeth, P., Berninger, U.N., Bovet, N., Schott, J. and Oelkers, E.H., 2018. Experimental determination of the solubility product of dolomite at 50–253 °C: *Geochimica et Cosmochimica Acta*, v. *224*, p. 262-275.

Benjakul, R., Hollis, C., Robertson, H.A., Sonnenthal, E.L. and Whitaker, F.F., 2020. Understanding controls on hydrothermal dolomitisation: insights from 3D reactive transport modelling of geothermal convection: *Solid Earth*, *11*(6), pp.2439-2461.

Bischoff, W.D., Bertram, M.A., Mackenzie, F.T. and Bishop, F.C., 1993. Diagenetic stabilization pathways of magnesian calcites: *Carbonates and Evaporites*, v. *8*(1), p. 82-89.

Blackwell, D., Richards, M., Frone, Z., Batir, J., Ruzo, A., Dingwall, R. and Williams, M., 2011. *Temperature-at-depth maps for the conterminous US and geothermal resource estimates* (GRC Transactions 35. GRC1029452). Southern Methodist University Geothermal Laboratory, Dallas, TX (United States).

Blanc, P., Lassin, A., Piantone, P., Azaroual, M., Jacquemet, N., Fabbri, A. and Gaucher, E.C., 2012. Thermoddem: A geochemical database focused on low temperature water/rock interactions and waste materials. *Applied geochemistry*, *27*(10), pp.2107-2116.

Blasco, M., Gimeno, M.J. and Auqué, L.F., 2017. *Comparison of different thermodynamic databases used in a geothermometrical modelling calculation*: *Procedia Earth and Planetary Science*, v. 17, p. 120–123.

Blasco, M., Gimeno, M.J. and Auqué, L.F., 2018. Low temperature geothermal systems in carbonate-evaporitic rocks: Mineral equilibria assumptions and geothermometrical calculations. Insights from the Arnedillo thermal waters (Spain): *Science of The Total Environment*, v. *615*, p. 526-539.

Blondes, M.S., Gans, K.D., Rowan, E.L., Thordsen, J.J., Reidy, M.E., Engle, M.A., Kharaka, Y.K. and Thomas, B., 2016. US Geological Survey National Produced Waters Geochemical Database v2. 2 (PROVISIONAL) Documentation. *USGS Energy Resources Program: Produced Waters, USGS*, *16*.

Bradley, W.F., Burst, J.F. and Graf, D.L., 1953. Crystal chemistry and differential thermal effects of dolomite: *American Mineralogist: Journal of Earth and Planetary Materials*, v. *38*(3-4), p. 207-217.

Bragg, W.L. and Williams, E.J., 1934. The effect of thermal agitation on atomic arrangement in alloys: *Proceedings of the Royal Society of London. Series A, Containing Papers of a Mathematical and Physical Character*, v. *145*(855), p. 699-730.

Bucher, K. and Grapes, R., 2011. Metamorphism of dolomites and limestones. In *Petrogenesis of Metamorphic Rocks* (pp. 225-255). Springer, Berlin, Heidelberg.
Bulmer, M.G., 1979. *Principles of statistics*. Courier Corporation.

Burnham, K.P. and Anderson, D.R., 2002. A practical information-theoretic approach. *Model selection and multimodel inference, 2nd ed. Springer, New York*, *2*.

Busenberg, E. and Plummer, N., 1982. The kinetics of dissolution of dolomite in CO2-H2O systems at 1.5 to 65oC and 0 to 1 atm PCO2: *American Journal of Science*, v. *282*(1), p. 45-78.

Carpenter, A.B., and Trout, M.L., 1978. Geochemistry of bromide-rich brines of the Dead Sea and Southern Arkansas. Oklahoma Geol. Surv., Circ.; USA; DA., v. 79, p. 78-88.

Chai, L. and Navrotsky, A., 1993. Thermochemistry of carbonate-pyroxene equilibria: *Contributions to Mineralogy and Petrology*, v. *114*(2), p. 139-147.

Chai, L., Navrotsky, A. and Reeder, R.J., 1995. Energetics of calcium-rich dolomite: *Geochimica et Cosmochimica Acta*, v. *59*(5), p. 939-944.

Chaikin, P.M., Lubensky, T.C. and Witten, T.A., 1995. *Principles of condensed matter physics* (Vol. 1). Cambridge: Cambridge university press.

Chernosky, J.V. and Berman, R.G., 1989. Experimental reversal of the equilibrium: clinochlore+ 2 magnesite= 3 forsterite+ spinel+ 2 CO 2+ 4 H 2 O and revised thermodynamic properties for magnesite: *American Journal of Science*, v. *289*(3), p. 249-266.
Chiodini, G., Frondini, F. and Marini, L., 1995. Theoretical geothermometers and PCO2 indicators for aqueous solutions coming from hydrothermal systems of medium-low temperature hosted in carbonate-evaporite rocks. Application to the thermal springs of the Etruscan Swell, Italy: *Applied Geochemistry*, v. *10*(3), p. 337-346.

Chou, L.E.I., Garrels, R.M. and Wollast, R., 1989. Comparative study of the kinetics and mechanisms of dissolution of carbonate minerals: *Chemical geology*, v. *78*(3-4), p. 269-282.

Daniilidis, A. and Herber, R., 2017. Salt intrusions providing a new geothermal exploration target for higher energy recovery at shallower depths. *Energy*, *118*, pp.658-670.

Deelman, J.C., 2003. *Low-temperature formation of dolomite and magnesite*. Eindhoven: Compact disc publications.

Derkani, M.H., Fletcher, A.J., Fedorov, M., Abdallah, W., Sauerer, B., Anderson, J. and Zhang, Z.J., 2019. Mechanisms of surface charge modification of carbonates in aqueous electrolyte solutions: *Colloids and Interfaces*, v. *3*(4), p. 62.

Dickson, J.A.D., 1995. Paleozoic Mg calcite preserved: Implications for the Carboniferous ocean: *Geology*, v. *23*(6), p. 535-538.

Dutton, A.R., 1987. Origin of brine in the San Andres Formation, evaporite confining system, Texas Panhandle and eastern New Mexico. *Geological Society of America Bulletin*, *99*(1), pp.103-112.

Engle, M.A. and Blondes, M.S., 2014. Linking compositional data analysis with thermodynamic geochemical modeling: oilfield brines from the Permian Basin, USA: *Journal of Geochemical Exploration*, v. *141*, p. 61-70.

Fang, Y. and Xu, H., 2018. Study of an Ordovician Carbonate with Alternating Dolomite–Calcite Laminations and Its Implication For Catalytic Effects of Microbes On the Formation of Sedimentary Dolomite. *Journal of Sedimentary Research*, *88*(6), pp.679-695.

Fang, Y. and Xu, H., 2019. A new approach to quantify the ordering state of protodolomite using XRD, TEM, and Z-contrast imaging: *Journal of Sedimentary Research*, v. *89*(6), p. 537-551.

Rosner, B., 2015. *Fundamentals of biostatistics*. Nelson Education.

Gamsjäger, H., Königsberger, E. and Preis, W., 2000. Lippmann diagrams: theory and application to carbonate systems: *Aquatic Geochemistry*, v. *6*(2), p. 119-132.

Garrels, R.M. and Drever, R.M., 1952. Mechanism of limestone replacement at low temperatures and pressures: *Geological Society of America Bulletin*, v. *63*(4), p. 325-380.

Garrels, R.M., Thompson, M.E. and Siever, R., 1960. Stability of some carbonates at 25 degrees C and one atmosphere total pressure: *American Journal of Science*, v. *258*(6), p. 402-418.

Gautelier, M., Schott, J. and Oelkers, E.H., 2007. An experimental study of dolomite dissolution rates at 80 C as a function of chemical affinity and solution composition: *Chemical Geology*, v. *242*(3-4), p. 509-517.

Gelman, A. and Hill, J., 2006. *Data analysis using regression and multilevel/hierarchical models*. Cambridge university press.

Goldsmith, J.R. and Heard, H.C., 1961. Subsolidus phase relations in the system CaCO3-MgCO3: *The Journal of Geology*, v. *69*(1), p. 45-74.

Goldsmith, J.R., 1983. Phase relations of rhombohedral carbonates: *Reviews in Mineralogy and Geochemistry*, v. *11*(1), p. 49-76.

Gomez-Rivas, E., Corbella, M., Martín-Martín, J.D., Stafford, S.L., Teixell, A., Bons, P.D., Griera, A. and Cardellach, E., 2014. Reactivity of dolomitizing fluids and Mg source evaluation of fault-controlled dolomitization at the Benicassim outcrop analogue (Maestrat Basin, E Spain): *Marine and Petroleum Geology*, v. *55*, p. 26-42.

Graf, D.L. and Goldsmith, J.R., 1956. Some hydrothermal syntheses of dolomite and protodolomite: *The Journal of Geology*, v. *64*(2), p. 173-186.

Goldsmith, J.R. and Graf, D.L., 1958. Structural and compositional variations in some natural dolomites. The Journal of Geology, 66(6), pp.678-693.

Gregg, J.M., Howard, S.A. and Mazzullo, S.J., 1992. Early diagenetic recrystallization of Holocene (< 3000 years old) peritidal dolomites, Ambergris Cay, Belize: *Sedimentology*, v. *39*(1), p. 143-160.

Gregg, J.M., Bish, D.L., Kaczmarek, S.E. and Machel, H.G., 2015. Mineralogy, nucleation and growth of dolomite in the laboratory and sedimentary environment: a review: *Sedimentology*, v. *62*(6), p. 1749-1769.

Gresens, R.L., 1981a. The aqueous solubility product of solid solutions: 1. Stoichiometric saturation; partial and total solubility product: *Chemical Geology*, v. *32*(1-4), p. 59-72.

Gresens, R.L., 1981b. The aqueous solubility product of solid solutions: 2. Extension to binary solutions with stoichiometric coefficients greater than unity; analogy with vapor pressure of a binary liquid solution: *Chemical Geology*, v. *32*(1-4), p. 73-86.

Grove, T.L., 1982. Use of exsolution lamellae in lunar clinopyroxenes as cooling rate speedometers: an experimental calibration: *American Mineralogist*, v. *67*(3-4), p. 251-268.

Halla, V.F. and Van Tassel, R., 1965. Auflosungserscheinungen bei erdalkalikarbonaten I. (Dissolution phenomena of alkaline earth aquacarbonates): *Radex-Rundschau*, v. *4*, p. 595-599.

Han, W.S., McPherson, B.J., Lichtner, P.C. and Wang, F.P., 2010. Evaluation of trapping mechanisms in geologic CO2 sequestration: Case study of SACROC northern platform, a 35-year CO2 injection site: *American Journal of Science*, v. *310*(4), p. 282-324.

Harrison, W.E., Luza, K.V., Prater M.L., and Cheung P.K., 1983. Geothermal resource assessment in Oklahoma, Okla: *Geol. Surv. Spec. Publ*., v. 83 (1), p. 42.

Hefter, G.T. and Tomkins, R.P. eds., 2003. *The experimental determination of solubilities*. John Wiley & Sons.

Helgeson, H.C., Delany, J.M., Nesbitt, H.W., and Bird, D.K., 1978. Summary and critique of the thermodynamic properties of rock-forming minerals: *American Journal of Science*, v. 287-A, p. 1–229.

Hemingway, B.S. and Robie, R.A., 1994. *Enthalpy and Gibbs energy of formation of dolomite, CaMg (CO 3) 2, at 298.15 K from HCl solution calorimetry* (No. 94-575). US Geological Survey.

Hirani, J., Bastesen, E., Boyce, A., Corlett, H., Gawthorpe, R., Hollis, C., John, C.M., Robertson, H., Rotevatn, A. and Whitaker, F., 2018. Controls on the formation of stratabound dolostone bodies, Hammam Faraun Fault block, Gulf of Suez: *Sedimentology*, v. *65*(6), p. 1973-2002.

Hitchon, B. and Brulotte, M., 1994. Culling criteria for "standard" formation water analyses: *Applied Geochemistry*, v. *9*(6), p. 637-645.

Holland, H.D., Kirsipu, T.V., Huebner, J.S. and Oxburgh, U.M., 1964. On some aspects of the chemical evolution of cave waters: *The Journal of Geology*, v. *72*(1), p. 36-67.

Holland, T.J.B. and Powell, R., 1990. An enlarged and updated internally consistent thermodynamic dataset with uncertainties and correlations: the system K2O–Na2O–CaO–MgO–MnO–FeO–Fe2O3–Al2O3–TiO2–SiO2–C–H2–O2: *Journal of metamorphic Geology*, v. *8*(1), p. 89-124.

Holland, T.J.B. and Powell, R., 1998. An internally consistent thermodynamic data set for phases of petrological interest: *Journal of metamorphic Geology*, v. *16*(3), p. 309-343.

Hox, J.J., Moerbeek, M. and Van de Schoot, R., 2017. *Multilevel analysis: Techniques and applications.* Routledge.

Hsu, K.J., 1963. Solubility of dolomite and composition of Florida ground waters: *Journal of Hydrology*, v. *1*(4), p. 288-310.

Huang, Y. and Fairchild, I.J., 2001. Partitioning of Sr2+ and Mg2+ into calcite under karst-analogue experimental conditions: *Geochimica et Cosmochimica Acta*, v. *65*(1), p. 47-62.

Hyeong, K. and Capuano, R.M., 2001. Ca/Mg of brines in Miocene/Oligocene clastic sediments of the Texas Gulf Coast: buffering by calcite/disordered dolomite equilibria: *Geochimica et Cosmochimica Acta*, v. *65*(18), p. 3065-3080.

Inbar, N., Rosenthal, E., Magri, F., Alraggad, M., Möller, P., Flexer, A., Guttman, J. and Siebert, C., 2019. Faulting patterns in the Lower Yarmouk Gorge potentially influence groundwater flow paths: *Hydrology and Earth System Sciences*, v. *23*, p. 763-771.

Johnson, J.W., Oelkers, E.H. and Helgeson, H.C., 1992. SUPCRT92: A software package for calculating the standard molal thermodynamic properties of minerals, gases, aqueous species, and reactions from 1 to 5000 bar and 0 to 1000°C: *Computers & Geosciences*, v. *18*(7), p. 899-947.

Kaczmarek, S.E. and Sibley, D.F., 2007. A comparison of nanometer-scale growth and dissolution features on natural and synthetic dolomite crystals: implications for the origin of dolomite: *Journal of Sedimentary Research*, v. *77*(5), p. 424-432.

Kaczmarek, S.E. and Sibley, D.F., 2011. On the evolution of dolomite stoichiometry and cation order during high-temperature synthesis experiments: an alternative model for the geochemical evolution of natural dolomites. *Sedimentary Geology*, 240(1-2), pp.30-40.

Kaczmarek, S.E. and Thornton, B.P., 2017. The effect of temperature on stoichiometry, cation ordering, and reaction rate in high-temperature dolomitization experiments. *Chemical Geology*, *468*, pp.32-41.

Karpov, I.K., Kiselev, A.I. and Letnikov, F.A., 1971. Chemical thermodynamics in petrology and geochemistry: *Irkutsk, Akademia Nauka*, p. 385.

Kell-Duivestein, I.J., Baldermann, A., Mavromatis, V. and Dietzel, M., 2019. Controls of temperature, alkalinity and calcium carbonate reactant on the evolution of dolomite and magnesite stoichiometry and dolomite cation ordering degree-An experimental approach. *Chemical Geology*, *529*, p.119292.

Khalaf, F.I., 2007. Occurrences and genesis of calcrete and dolocrete in the Mio-Pleistocene fluviatile sequence in Kuwait, northeast Arabian Peninsula: *Sedimentary Geology*, v. *199*(3-4), p. 129-139.

Khalifa, M.K. and Abed, A.M., 2010. Lithostratigraphy and Microfacies Analysis of the Ajlun Group (Cenomanian to Turonian) in Wadi Sirhan Basin, SE Jordan. *Jordan Journal of Earth and Environmental Sciences*, v. *3*(1), p. 1-16.

Kharaka, Y.K., Maest, A.S., Carothers, W.W., Law, L.M., Lamothe, P.J. and Fries, T.L., 1987. Geochemistry of metal-rich brines from central Mississippi Salt Dome basin, USA: *Applied Geochemistry*, v. *2*(5-6), p. 543-561.

Knacke, O., Kubaschewski, O and Hesselmann, K., 1991. *Thermochemical properties of inorganic substances*. Berlin, New York, Springer-Verlag.

Königsberger, E. and Gamsjäger, H., 1992. Solid-solute phase equilibria in aqueous solution: VII. A re-interpretation of magnesian calcite stabilities: *Geochimica et cosmochimica acta*, v. *56*(11), p. 4095-4098.

Kramer, J.R., 1959. Correction of some earlier data on calcite and dolomite in sea water: *Journal of Sedimentary Research (SEPM)*, v. *29*(3), p. 465-467.

Land, L.S. 1980. The isotopic and trace element geochemistry of dolomite: the state of the art: *Society of Economic Paleontologists and Mineralogists Special Publication*, No. 28, p. 87-110.

Land, L.S. and Prezbindowski, D.R., 1981. The origin and evolution of saline formation water, Lower Cretaceous carbonates, south-central Texas, USA: *Journal of Hydrology*, v. *54*(1-3), p. 51-74.

Land, L.S., 1984. Frio Sandstone Diagenesis, Texas Gulf Coast: A Regional Isotopic Study: Part 1. Concepts and Principles: *AAPG Special Volumes*, p. 47-62.

Land, L.S., 1985. The origin of massive dolomite: *Journal of Geological Education*, v. *33*(2), p. 112-125.

Land, L.S., 1998. Failure to Precipitate Dolomite at 25 ºC from Dilute Solution Despite 1000-Fold Oversaturation after 32 Years: *Aquatic Geochemistry*, v. *4*(3-4), p. 361-368.

Langmuir, D., ms, 1965. Stability of carbonates in the system MgO-CO_2- H_2O. PhD thesis. Harvard University.

Langmuir, D., 1971. The geochemistry of some carbonate ground waters in central Pennsylvania. *Geochimica et Cosmochimica Acta*, *35*(10), pp.1023-1045.

Laya J.C., Teoh C.P. , Whitaker F.F., Manche C., Kaczmarek S., Tucker M.E., Gabellone, T., Hasiuk, F., 2021. Dolomitization of a Miocene-Pliocene progradational carbonate

platform by mesohaline brine: testing the reflux model on Bonaire Island: *Marine and Petroleum Geology* (in press as of 30th Dec)

Lippmann, F., 1977. The solubility products of complex minerals, mixed crystals, and three-layer clay minerals: *Neues Jahrbuch für Mineralogie Abhandlungen*, v. 130, p. 243-263.

Lippmann, F., 1980. Phase diagrams depicting aqueous solubility of binary mineral systems. *Neues Jahrbuch für Mineralogie Abhandlungen*, v.139 (1), p. 1-25.

Loucks, R.G., Richmann, D.L. and Milliken, K.L., 1980. Factors controlling porosity and permeability in geopressured Frio sandstone reservoirs, General Crude Oil/Department of Energy Pleasant Bayou test wells, Brazoria County, Texas. In *Proceedings of the Fourth Geopressured Geothermal Energy Conference*, v. 1, p. 46-82.

Loucks, R.G., Dodge, M.M. and Galloway, W.E., 1984. Regional controls on diagenesis and reservoir quality in lower Tertiary sandstones along the Texas Gulf Coast: Part 1. Concepts and principles: AAPG Special Volumes, v. 59, p. 14-45.

Lumsden, D.N. and Chimahusky, J.S., 1980. Relationship between dolomite nonstoichiometry and carbonate facies parameters: *Society of Economic Paleontologists and Mineralogists Special Publication*, No. 28, p. 123-137.

Luth, R.W., 2001. Experimental determination of the reaction aragonite+ magnesite= dolomite at 5 to 9 GPa: *Contributions to Mineralogy and Petrology*, v. *141*(2), p. 222-232.

Maier, C.G. and Kelley, K.K., 1932. An equation for the representation of high-temperature heat content data1: *Journal of the American chemical society*, v. *54*(8), p. 3243-3246.

Manche, C.J. and Kaczmarek, S.E., 2019. Evaluating reflux dolomitization using a novel high-resolution record of dolomite stoichiometry: A case study from the Cretaceous of central Texas, USA. *Geology*, *47*(6), pp.586-590

McNaught, A.D., 1997. *Compendium of chemical terminology* (Vol. 1669). Oxford: Blackwell Science.

Miron, G.D., Wagner, T., Kulik, D.A. and Lothenbach, B., 2017. An internally consistent thermodynamic dataset for aqueous species in the system Ca-Mg-Na-K-Al-Si-OHC-Cl to 800 ˚C and 5 kbar: *American Journal of Science*, v. *317*(7), p. 755-806.

Miser, D.E., Swinnea, J.S. and Steinfink, H., 1987. TEM observations and X-ray crystal-structure refinement of a twinned dolomite with a modulated microstructure: *American Mineralogist*, v. *72*(1-2), p. 188-193.

Möller, P., 1973. Determination of the composition of surface layers of calcite in solutions containing Mg2+: *Journal of Inorganic and Nuclear Chemistry*, v. *35*(2), p. 395-401.

Möller, P. and Sastri, C.S., 1974. Estimation of the number of surface layers of calcite involved in Ca-45Ca isotopic exchange with solution: *Zeitschrift für Physikalische Chemie*, v. *89*(1-4), p. 80-87.

Möller, P. and De Lucia, M., 2020. The impact of Mg2+ ions on equilibration of Mg-Ca carbonates in groundwater and brines: *Geochemistry*, v. 80(2), p.125611.

Morton, R.A. and Land, L.S., 1987. Regional variations in formation water chemistry, Frio Fm. (Oligocene), Texas Gulf Coast: *AAPG bulletin*, v. *71*(2), p.191-206.

Morrow, D. W., Gorham, B. L., and Wong, J. N., 1994, Dolomite-calcite equilibrium at 220 to 240oC at saturation vapour pressure: experimental data: Geochimica et Cosmochimica Acta, v. 58, n. 1, p. 169–177

Nakagawa, S., Johnson, P.C. and Schielzeth, H., 2017. The coefficient of determination R 2 and intra-class correlation coefficient from generalized linear mixed-effects models revisited and expanded: *Journal of the Royal Society Interface*, v. *14*(134), p. 20170213.

Naumov, G.B., Ryzhenko, B.N. and Khodakovsky, I.L., 1974. Handbook of thermodynamic data. *Transl. into ENGLISH of the publ." Handbook of Thermodyanic Data" Moscow, Atomizdat., 1971*.

Navrotsky, A. and Loucks, D., 1977. Calculation of subsolidus phase relations in carbonates and pyroxenes: *Physics and Chemistry of Minerals*, v. *1*(1), p. 109-127.

Navrotsky, A. and Capobianco, C., 1987. Enthalpies of formation of dolomite and of magnesian calcites: *American Mineralogist*, v. *72*(7-8), p. 782-787.

Navrotsky, A., Dooley, D., Reeder, R. and Brady, P., 1999. Calorimetric studies of the energetics of order-disorder in the system Mg_{1-x} Fe_xCa $(CO_3)_2$: *American Mineralogist*, v. *84*(10), p.1622-1626.

Nordeng, S.H. and Sibley, D.F., 1994. Dolomite stoichiometry and Ostwald's step rule: *Geochimica et Cosmochimica Acta*, v. *58*(1), p. 191-196.

Parkhurst, D.L. and Appelo, C.A.J., 1999. User's guide to PHREEQC (Version 2): A computer program for speciation, batch-reaction, one-dimensional transport, and inverse geochemical calculations: *Water-resources investigations report*, v. *99*(4259), p. 312.

Pina, C.M., Pimentel, C. and Crespo, Á., 2020. Dolomite cation order in the geological record: *Chemical Geology*, v. 547, p.119667.

Plummer, L.N. and Mackenzie, F.T., 1974. Predicting mineral solubility from rate data; application to the dissolution of magnesian calcites: *American Journal of Science*, v. *274*(1), p. 61-83.

Plummer, L.N. and Busenberg, E., 1982. The solubilities of calcite, aragonite and vaterite in CO_2-H_2O solutions between 0 and 90°C, and an evaluation of the aqueous model for the system $CaCO_3$-CO_2-H_2O: *Geochimica et cosmochimica acta*, v. *46*(6), p. 1011-1040.

Plummer, L.N., Parkhurst, D.L., Fleming, G.W. and Dunkle, S., 1988. PHRQPITZ, a computer program incorporating Pitzer's equations for calculation of geochemical reactions in brines. *US Geological Survey Water Resources Investigation Report*, *88*, p.4153.

Pokrovsky, O.S. and Schott, J., 2001. Kinetics and mechanism of dolomite dissolution in neutral to alkaline solutions revisited: *American Journal of Science*, v. *301*(7), p. 597-626.

Pokrovsky, O.S., Golubev, S.V., Schott, J. and Castillo, A., 2009. Calcite, dolomite and magnesite dissolution kinetics in aqueous solutions at acid to circumneutral pH, 25 to 150 °C and 1 to 55 atm pCO_2: New constraints on CO_2 sequestration in sedimentary basins: *Chemical geology*, v. *265*(1-2), p. 20-32.

Prédali, J.J. and Cases, J.M., 1973. Zeta potential of magnesian carbonates in inorganic electrolytes: *Journal of Colloid and Interface Science*, v. *45*(3), p. 449-458.

Radke, B.M. and Mathis, R.L., 1980. On the formation and occurrence of saddle dolomite: *Journal of Sedimentary Research*, v. *50*(4), p. 1149-1168.

Ray, S., ms, 2016. National evaluation for development and exploration potential of mineral commodities in produced waters. PhD thesis. The University of Texas at El Paso.

Reeder, R.J. and Wenk, H.R., 1983. Structure refinements of some thermally disordered dolomites: *American Mineralogist*, v. *68*(7-8), p. 769-776.

Reeder, R.J., 1992. Carbonates; growth and alteration microstructures: *Reviews in Mineralogy and Geochemistry*, v. *27*(1), p. 380-424.

Reeder, R.J., 2000. Constraints on cation order in calcium-rich sedimentary dolomite: *Aquatic Geochemistry*, v. *6*(2), p. 213-226.

Robie, R.A., Hemingway, B.S. and Fisher, J.R., 1978. *Thermodynamic properties of minerals and related substances at 298. 15 k and 1 bar (10/sup 5/pascals) pressure and at higher temperatures* (No. USGS-BULL-1452). Technical Report, Geological Survey, Washington, DC (USA).

Robie, R.A. and Hemingway, B.S., 1995. *Thermodynamic properties of minerals and related substances at 298.15 K and 1 bar (105 Pascals) pressure and at higher temperatures.* (Vol. 2131). US Government Printing Office.

Rock, P.A., Mandell, G.K., Casey, W.H. and Walling, E.M., 2001. Gibbs energy of formation of dolomite from electrochemical cell measurements and theoretical calculations: *American Journal of Science*, v. *301*(2), p. 103-111.

Rodriguez-Blanco, J.D., Shaw, S. and Benning, L.G., 2015. A route for the direct crystallization of dolomite: *American Mineralogist*, v. *100*(5-6), p. 1172-1181.

Rosenberg, P.E. and Holland, H.D., 1964. Calcite-dolomite-magnesite stability relations in solutions at elevated temperatures: *Science*, v. *145*(3633), p. 700-701.

Shen, Z., Konishi, H., Brown, P.E. and Xu, H., 2013. STEM investigation of exsolution lamellae and "c" reflections in Ca-rich dolomite from the Platteville Formation, western Wisconsin: *American Mineralogist*, v. *98*(4), p.760-766.

Sherman, L.A. and Barak, P., 2000. Solubility and dissolution kinetics of dolomite in Ca–Mg–HCO_3/CO_3 solutions at 25°C and 0.1 MPa carbon dioxide: *Soil Science Society of America Journal*, v. *64*(6), p. 1959-1968.

Shock, E.L. and Helgeson, H.C., 1988. Calculation of the thermodynamic and transport properties of aqueous species at high pressures and temperatures: Correlation algorithms for ionic species and equation of state predictions to 5 kb and 1000°C: *Geochimica et Cosmochimica Acta*, v. *52*(8), p. 2009-2036.

Shock, E.L., Sassani, D.C., Willis, M. and Sverjensky, D.A., 1997. Inorganic species in geologic fluids: correlations among standard molal thermodynamic properties of aqueous ions and hydroxide complexes: *Geochimica et Cosmochimica Acta*, v. *61*(5), p. 907-950.

Shope, E.N., Reber, T.J., Stutz, G.R., Aguirre, G.A., Jordan, T.E. and Tester, J.W., 2012, February. Geothermal resource assessment: A detailed approach to low-grade resources in the states of New York and Pennsylvania. In *Proceedings, Thirty-Seventh Workshop on Geothermal Reservoir Engineering* (p. 885-893). Stanford, California: Stanford University.

Siebert, C., Möller, P., Geyer, S., Kraushaar, S., Dulski, P., Guttman, J., Subah, A. and Rödiger, T., 2014. Thermal waters in the Lower Yarmouk Gorge and their relation to surrounding aquifers: *Geochemistry*, v. *74*(3), p. 425-441.

Sinclair, D.J., 2011. Two mathematical models of Mg and Sr partitioning into solution during incongruent calcite dissolution: implications for dripwater and speleothem studies: *Chemical Geology*, v. *283*(3-4), p. 119-133.

Sinclair, D.J., Banner, J.L., Taylor, F.W., Partin, J., Jenson, J., Mylroie, J., Goddard, E., Quinn, T., Jocson, J. and Miklavič, B., 2012. Magnesium and strontium systematics in tropical speleothems from the Western Pacific: *Chemical Geology*, v. *294*, p. 1-17.

Sperber, C.M., Wilkinson, B.H. and Peacor, D.R., 1984. Rock composition, dolomite stoichiometry, and rock/water reactions in dolomitic carbonate rocks: *The Journal of Geology*, v. *92*(6), p. 609-622.

Spötl, C. and Pitman, J.K., 1998. Saddle (baroque) dolomite in carbonates and sandstones: a reappraisal of a burial-diagenetic concept: *Carbonate Cementation in Sandstones: Distribution Patterns and Geochemical Evolution*, v. *26*, p. 437-460.

Stoessell, R.K., Klimentidis, R.E. and Prezbindowski, D.R., 1987. Dedolomitization in Na-Ca-Cl brines from 100° to 200° C at 300 bars: *Geochimica et Cosmochimica Acta*, v. *51*(4), p. 847-855.

Stout, J.W. and Robie, R.A., 1963. Heat capacity from 11 to 300 K., entropy, and heat of formation of dolomite: *The Journal of Physical Chemistry*, v. *67*(11), p. 2248-2252.

Strand, S., Høgnesen, E.J. and Austad, T., 2006. Wettability alteration of carbonates—Effects of potential determining ions (Ca^{2+} and SO_4^{2-}) and temperature: *Colloids and Surfaces A: Physicochemical and Engineering Aspects*, v. *275*(1-3), p. 1-10.

Team, R.C., 2000. R language definition. *Vienna, Austria: R foundation for statistical computing*.

Tesmer, M., Moeller, P., Wieland, S., Jahnke, C., Voigt, H. and Pekdeger, A., 2007. Deep reaching fluid flow in the North East German Basin: origin and processes of groundwater salinization: *Hydrogeology Journal*, v. *15*(7), p. 1291-1306.

Thieling, S.C. and Moody, J.S., 1997. Atlas of shallow Mississippi salt domes.

Thorstenson, D.C. and Plummer, L.N., 1977. Equilibrium criteria for two-component solids reacting with fixed composition in an aqueous phase; example, the magnesian calcites: *American Journal of Science*, v. *277*(9), p. 1203-1223.

Ulfsbo, A., Abbas, Z. and Turner, D.R., 2015. Activity coefficients of a simplified seawater electrolyte at varying salinity (5–40) and temperature (0 and 25° C) using Monte Carlo simulations: *Marine Chemistry*, v. *171*, p. 78-86.

Underwood, T., Erastova, V. and Greenwell, H.C., 2016. Ion adsorption at clay-mineral surfaces: the Hofmeister series for hydrated smectite minerals. Clays and Clay Minerals, 64(4), pp.472-487.

Usdowski, H.E., 1967. *Die Genese von Dolomit in Sedimenten* (Vol. 4). Springer.

Usdowski, E., 1989. Synthesis of dolomite and magnesite at 60 °C in the system Ca^{2+}-Mg^{2+}-Co_3^{2-}-$C1_2^{2-}$-H_2O: Naturwissenschaften (NW), v. *76*(8), p. 374-375.

Usdowski, E., 1994. Synthesis of dolomite and geochemical implications. In *Dolomites: A Volume in Honour of Dolomieu* (Vol. 21, pp. 345-360). Oxford UK, Blackwell Scientific Publications.

Van Tendeloo, G., Wenk, H.R. and Gronsky, R., 1985. Modulated structures in calcian dolomite: A study by electron microscopy: *Physics and Chemistry of Minerals*, v. *12*(6), p. 333-341.

Vespasiano, G., Apollaro, C., Muto, F., Dotsika, E., De Rosa, R. and Marini, L., 2014. Chemical and isotopic characteristics of the warm and cold waters of the Luigiane Spa near Guardia Piemontese (Calabria, Italy) in a complex faulted geological framework: *Applied Geochemistry*, v. *41*, p. 73-88.

Wagman, D.D., Evans, W.H., Parker, V.B., Schumm, R.H. and Halow, I., 1982. *The NBS tables of chemical thermodynamic properties. Selected values for inorganic and C1 and C2 organic substances in SI units*. National Standard Reference Data System.

Warren, J., 2000. Dolomite: occurrence, evolution and economically important associations: *Earth-Science Reviews*, v. *52*(1-3), p. 1-81.

Westfall, P.H., 2014. Kurtosis as peakedness, 1905–2014. RIP. *The American Statistician*, *68*(3), pp.191-195.

Whitaker, F.F. and Xiao, Y., 2010. Reactive transport modeling of early burial dolomitization of carbonate platforms by geothermal convection: *AAPG bulletin*, *94*(6), pp.889-917.

Wolery, T.J., Jackson, K.J., Bourcier, W.L., Bruton, C.J., Viani, B.E., Knauss, K.G. and Delany, J.M., 1990. Current status of the EQ3/6 software package for geochemical modelling: ACS Symposium Series, v. 416 (Chapter 8), p. 104-116.

Wright, K., Cygan, R.T. and Slater, B., 2002. Impurities and nonstoichiometry in the bulk and on the (1014) surface of dolomite: *Geochimica et cosmochimica acta*, v. *66*(14), p. 2541-2546.

Xu, T., 2008. *TOUGHREACT testing in high ionic strength brine sandstone systems* (No. LBNL--1051E). Ernest Orlando Lawrence Berkeley National Laboratory.

Yanat'eva, O.K., 1952. Solubility of dolomite in water salt solutions: *Izvestiya Sektora FkhA Akademii Nauk SSSR*, v. *20*, p. 252-268.

Zhang, S., Yang, L., DePaolo, D.J. and Steefel, C.I., 2015. Chemical affinity and pH effects on chlorite dissolution kinetics under geological CO2 sequestration related conditions. *Chemical Geology*, *396*, pp.208-217.

Figure captions

Fig. 1 a) Calcite can be described by both the hexagonal unit cell (17.06Å in height) and the rhombohedral unit cell (superimposed in black lines). Perpendicular to the c-axis are alternating planes of Ca^{2+} cations and CO_3^{2-} groups. b) Dolomite hexagonal unit cell (16.01Å in height) with rhombohedral unit cell superimposed. Cation ordering results in the alternating layers of Ca^{2+} and Mg^{2+} cations. Reproduced with permission from Gregg and others (2015).

Fig. 2 Temperature dependency of the dolomite order parameter (*s*) as defined in equation (12) for a dolomite with a critical temperature (T_c) of 1473K equating to a synthetic, ideal dolomite (Goldsmith and Heard, 1961). There are four solutions (Chaikin et al., 1995); (1) $s = 0$ at and above T_c, (2) $s = \pm\sqrt{\frac{3(T_c - T)}{T}}$ for the asymptotic approach to T_c, (3) $s = 1$ at T = 0K, (4) $s = \tanh(T_c/T)$ for the asymptotic approach to T = 0K. For the Bragg-Williams model well-ordered dolomite ($s \geq 0.96$) is the most stable state at conditions ≤ 500°C. Dashed line for Helgeson and others (1978) represents their estimation of naturally ordered ($s = 0.7$) dolomite. Gregg and others (1992) determine $0.7 < s < 0.9$ for Holocene dolomites. Dashed line for Hyeong and Capuano (2001) represents their estimate for a partially ordered ($s = 0.4$) dolomite. Modified from Helgeson and others (1978).

Fig. 3 Relative frequencies of dolomite stoichiometry for; a) Pliocene Bonaire dolomite (n=72; samples with > 90% dolomite) (Laya and others, 2021), b) Phanerozoic dolomites from North America (n=55) (Sperber and others, 1984), c) Global dolomites based on samples (n=654) from a wide variety of localities and ages compiled by Sperber and others, (1984); Triassic of north-western Germany (n=48), Phanerozoic of North America (n=345), Tertiary of Libya (n=139), Upper Jurassic of Germany (n=76), Upper Permian of Germany (n=43), Upper Devonian of Belgium (n=3).

Fig. 4 a) The re-evaluation by Thorstenson and Plummer (1977) of data from Plummer and Mackenzie (1974) was notably critiqued by Gresens (1981a) for producing too great a range in equilibrium $\log_{10}({}^{a}Ca^{2+}/{}^{a}Mg^{2+})$ values. The inclusion of this data by Möller and De Lucia (2020) led to their erroneous interpretation that the Bénézeth and others (2018) data is comparable to that of Möller (1973). Redrawn from Möller and De Lucia (2020). b) Solution $[Ca^{2+}]$ and $[Mg^{2+}]$ as a function of the square root of time during the dissolution of HMC algal calcite (Plummer and Mackenzie, 1974). $[Ca^{2+}]$ and $[Mg^{2+}]$ are non-linear in stage one suggesting congruent dissolution. In stage two both are linear suggesting release to the solution is controlled by diffusion through a product layer. In stage three $[Mg^{2+}]$ is linear but obeys a parabolic rate law and the non-linear decrease in $[Ca^{2+}]$ indicates a transition towards formation of a more Mg-rich incongruent phase than that which precipitates during stage two (~ pure calcite).

Fig. 5 a) Blue lines and symbols represent K_{sp-dol} estimations and $\log_{10}({}^{a}Ca^{2+}/{}^{a}Mg^{2+})$ observations from groundwater studies. Mustard yellow markers denote a determination of

K_{sp-dol} only though dolomite precipitation (Möller (1973) included here). Red markers represent approaches from dolomite dissolution. Green lines and symbols represent approaches from both dolomite precipitation and dissolution. Black symbols are derived through a thermodynamic indirect approach (see supplementary table 2). Shaded area reflects calculated 95% confidence intervals. b) Equilibrium $\log_{10}({}^{a}Ca^{2+}/{}^{a}Mg^{2+})$ for solutions buffered by (ideal solid solution model) $LMC_{(4\%MgCO_3)}$ and calcian $dolomite_{(2\%CaCO_3)/(4\%CaCO_3)}$ (and SUPCRT92 calcite and J23 dolomite). This study's reference model (J21) of $\log_{10}({}^{a}Ca^{2+}/{}^{a}Mg^{2+})$ values between the SUPCRT92-filter is solid purple with the model (K1) of values not subject to the SUPCRT92-filter (n=11,480) in dashed green. The model (J24) utilizing a fixed β_1 coefficient of -0.06919 is in dashdot purple.

Fig. 6 a) This study's geothermal gradient interpolation (0.1x0.1° Lat/Long resolution) using the SMUH dataset (Blackwell and others, 2011). b) Number of SMUH samples per US county (for counties with ≥ 1 sample). Large counties in historically prolific oil producing states have the highest number of temperature measurements, with a maximum n = 3,739 for Crockett county, Texas. c) The SMUH interpolation (Blackwell and others, 2011) for heat flow which utilizes the same data as this study's interpolation of geothermal gradients, which are most similar in areas with a high spatial resolution of temperature measurements. d) Number of filtered PWGD samples (n=11,480) per US county (for counties with ≥ 1 sample). Large counties in historically prolific oil producing states have the highest number of temperature measurements, with a maximum n = 519 for Fremont county, Wyoming. e) Mean annual land surface temperatures (Bechtel, 2015) interpolated at 0.1x0.1° Lat/Long resolution. All maps, aside from C, are WGS 84.

Fig. 7 a) Map showing Test Areas A and B (black boxes) in the south-eastern USA, and the locations of Frio formation samples (crosses). For both b) and c) circles mark salt dome locations from Beckman and Williamson (1990) and Thieling and Moody (1997). Colours represent this study's geothermal gradients (fig. 6a). Open triangles are fields contained in the PWGD. Filled triangles are fields for which data has previously been published (Kharaka and others, 1987; Hyeong and Capuano, 2001). Some fields located outside of the bounding boxes are included in the analysis after sample locations are rounded to the nearest 0.1° Lat/Long. b) Location of fields in Test Area A (W94°48' – W96°00'/N28°48' – N29°30'). c) Location of fields in Test Area B (W88°12' – W90°00'/N31°30' – N32°12'). Unfilled squares (Soso and Raleigh fields) represent fields included in both the literature and PWGD datasets. All maps are WGS 84.

Fig. 8 a) Comparison of temperatures measured at-formation-depth observed by Hyeong and Capuano, (2001) and those predicted for PWGD samples in Test Area A by this study's methodology. A geothermal gradient representing the average geothermal gradient (SMUH data – mean 33°C/km; range 29-35°C/km shaded grey) and the average surface temperature (MAST data - mean 16°C; range 15-16°C) calculated for the PWGD samples in Test Area A shows a reasonable fit to the measured temperatures. Samples from the shallower (651-921m) Miocene sediments have measured temperatures significantly above the upper range of geothermal gradients calculated for Test Area A, emphasizing the limitations of linear

geothermal gradients. b) Comparison of temperatures at-formation-depth measured by Kharaka and others (1987) and those predicted for PWGD samples in Test Area B. A geothermal gradient representing the average geothermal gradient (SMUH data – mean 27°C/km; range 22-34°C/km shaded grey) and the average surface temperature (MAST data - mean 13°C; range 12-14°C) calculated for the PWGD samples in Test Area B shows a reasonable fit to the measured temperatures.

Fig. 9 All plots include the reference model J21 (95% confidence intervals shaded light grey), this study's mixed model A4 of the Hyeong and Capuano (2001) dataset (95% confidence intervals shaded dark grey) and the SUPCRT92 ordered dolomite-calcite & disordered dolomite-calcite equilibria. Model results shown are the global-level results except for where '{ }' are used which indicates a group-level result. Literature datasets; L & P (1981) – Land and Prezbindowski (1981), K (1987) – Kharaka and others (1987), H & C (2001) – Hyeong and Capuano (2001), M & D (2020) – Moller and DeLucia (2020). a) The Hyeong and Capuano (2001) linear model A1 is near identical to the linear model A2 (confidence intervals shaded blue) of the Hyeong and Capuano (2001) dataset recalculated using PHREEQC-Pitzer. For this dataset the three-term Maier-Kelly regression (model A3) produces a spurious extrapolation outside the experimental range. The (random intercept) mixed model A4 calculates a unique intercept $\log_{10}({}^{a}Ca^{2+}/{}^{a}Mg^{2+})$ for each group whilst the $\log_{10}({}^{a}Ca^{2+}/{}^{a}Mg^{2+})$-temperature gradient is constant for all groups. For the (random slope) mixed model A5 the gradient for each group can also vary. b) There are significant differences between the linear models of the Chocolate/Halls Bayou (model B1) and West Columbia (model C1) fields, and the model A4 group-level results for these fields. c) For the small Miocene Fm. dataset (n=6) the transition from the linear model E1 to the model A4 group-level results is pronounced. The Frio Fm. (n=45; Hyeong and Capuano (2001) dataset) linear model D1 is relatively similar to the model A4 group-level result. d) The model F1 of PWGD samples contained within Test Area A (n=21) shows a similar profile to the model A4 of the Hyeong and Capuano (2001) dataset, with typically low $\log_{10}({}^{a}Ca^{2+}/{}^{a}Mg^{2+})$ values, whilst Frio Fm. samples elsewhere (model G1) are clearly different. Note also that the model G1 and J21 profiles for the Hastings field have no overlap with the observed $\log_{10}({}^{a}Ca^{2+}/{}^{a}Mg^{2+})$ values. e) Samples from Kharaka and others (1987) (n=16) (model H1), including the Reedy (n=5) and Soso (n=4) samples, and in general samples from Test Area B (n=204) (model I1) have higher $\log_{10}({}^{a}Ca^{2+}/{}^{a}Mg^{2+})$ values than those present in Test Area A (model F1) being closer to the reference model J21. f) Yarmouk gorge dataset from Möller and De Lucia (2020) with models including all samples (model L1; n=42) and excluding samples with temperatures <25°C (model M1; n=36). Also shown (dotted box) is the area represented in figs a, b and c.

Fig. 10 a) 2D Histogram for all (n=11,480) PWGD samples with bin dimensions 10°C x 0.05 $\log_{10}({}^{a}Ca^{2+}/{}^{a}Mg^{2+})$ b) modal, c) mean, d) kurtosis and e) skewness values for each lithology based on 10°C bin. Modal and mean values for temperatures >120°C are not shown as these samples represent <2.6% of the PWGD data (n=302) and, like kurtosis and skewness values for temperature range (see text), this data is relatively uninformative as

there is a high degree of scatter. Kurtosis and skewness values for whole populations are recorded in the legends. f) Standard deviation. g) Cumulative sum of samples. h) Limestone frequency distribution for 60-70°C showing unimodal positive skew. i) Sandstone frequency distribution for 80-90°C showing a bimodal distribution.

Fig. 11 Comparison of calcite-dolomite (model J23) equilibrium $^{a}Ca^{2+}$, $^{a}Mg^{2+}$ and $\log_{10}(^{a}Ca^{2+}/^{a}Mg^{2+})$ calculated using PHREEQC-Pitzer with background electrolytes (NaCl and Na_2SO_4) and common ions ($CaSO_4$) of varying compositions and concentrations at 25°C. For an equivalent ionic strength, a divalent background electrolyte (Na_2SO_4) in comparison to a monovalent background electrolyte (NaCl) generates a greater amount of dissolution of both calcite and dolomite and lower overall $^{a}Ca^{2+}$ and $^{a}Mg^{2+}$ due to the greater overall strength of ion-ion interactions. Whilst activities change and $^{a}Ca^{2+}$ is always higher than $^{a}Mg^{2+}$ the difference ($\log_{10}(^{a}Ca^{2+}/^{a}Mg^{2+})$) between these two values remains constant.

Supplementary figure 1. Comparison of the $\log_{10}(^{a}Ca^{2+}/^{a}Mg^{2+})$ values for the Hyeong and Capuano (2001) dataset calculated by Hyeong and Capuano (2001) (using SOLMINEQ88-Pitzer) and by this study (using PHREEQC-Pitzer). For clarity and, to demonstrate no temperature dependence, we present calculated $\log_{10}(^{a}Ca^{2+}/^{a}Mg^{2+})$ values with reference to both the sample ID and temperature.

Supplementary figure 2. Measured temperatures and sample depths from Tesmer and others (2007). The representative geothermal gradient for Germany is derived from Agemar and others (2012) and a ±10°C/km uncertainty is shaded grey for reference.

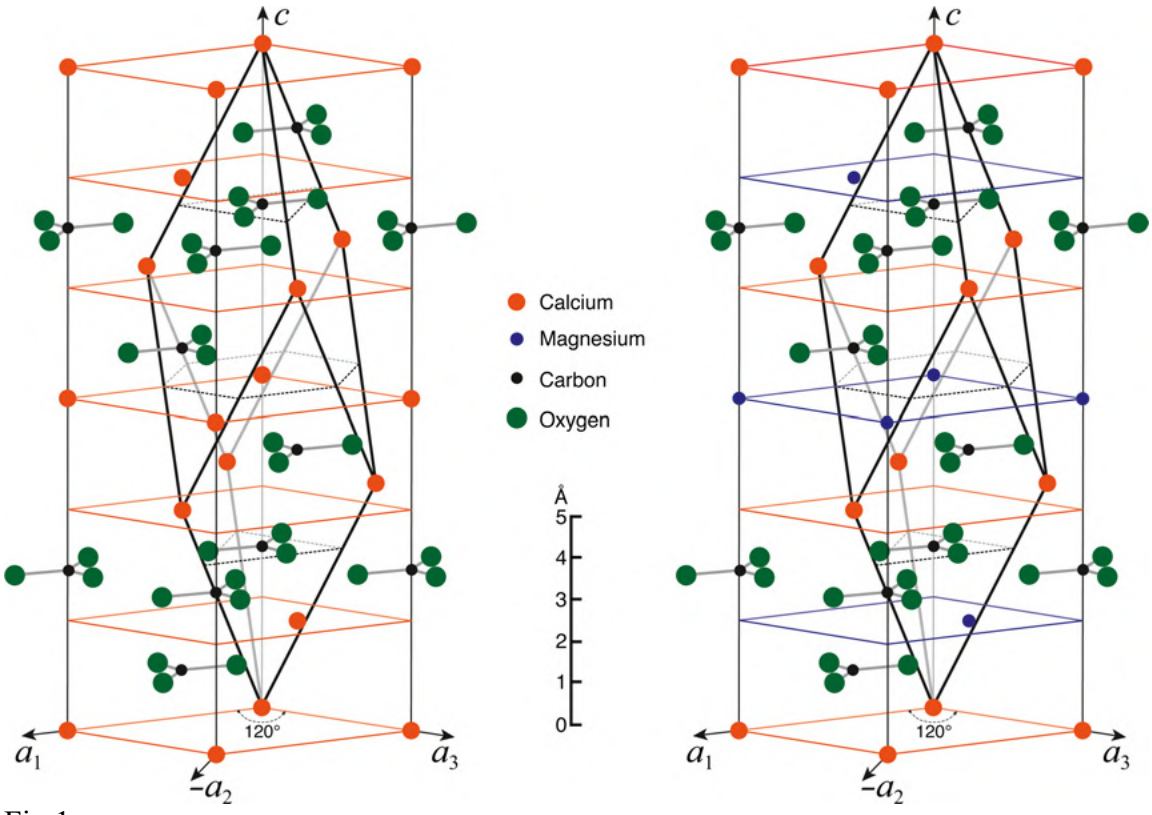
c
Calcium
Magnesium
Carbon
Oxygen
Å
5
4
3
2
1
0
120°
a_1
a_3
$-a_2$
c
120°
a_1
a_3
$-a_2$

Fig.1

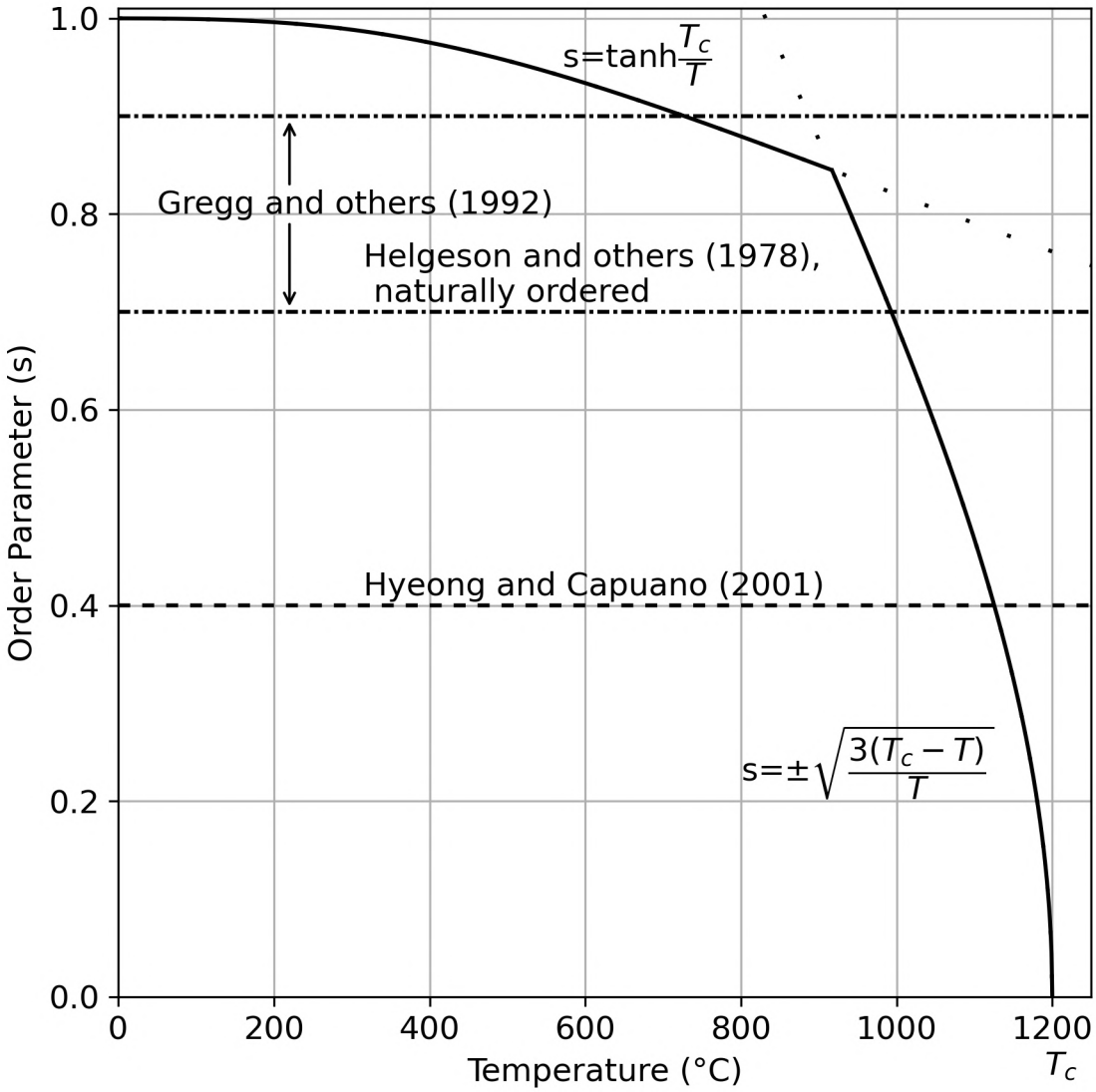
1.0
0.8
0.6
0.4
0.2
0.0
Order Parameter (s)
0
200
400
600
800
1000
1200
Temperature (°C)
T_c
s=tanh$\frac{T_c}{T}$
Gregg and others (1992)
Helgeson and others (1978),
naturally ordered
Hyeong and Capuano (2001)
s=±$\sqrt{\frac{3(T_c-T)}{T}}$

Fig.2

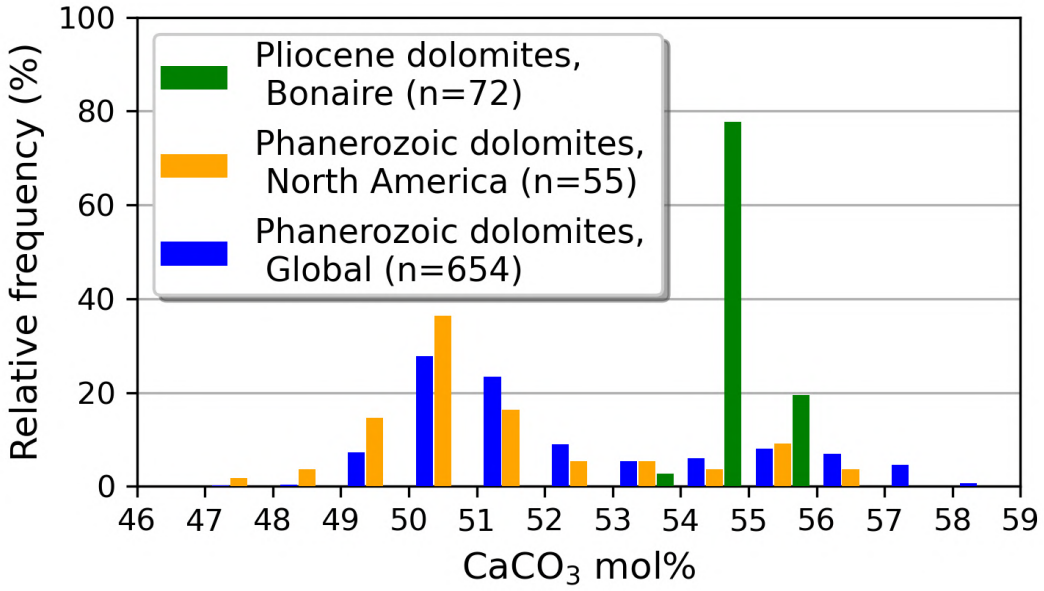
Pliocene dolomites, Bonaire (n=72)
Phanerozoic dolomites, North America (n=55)
Phanerozoic dolomites, Global (n=654)
Relative frequency (%)
100
80
60
40
20
0
46
47
48
49
50
51
52
53
54
55
56
57
58
59
CaCO3 mol%

Fig. 3

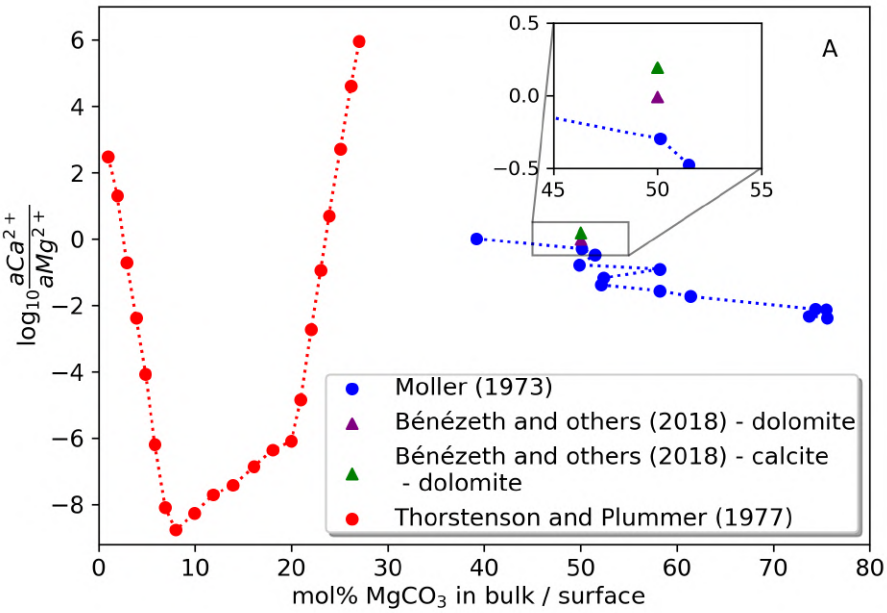
A
Moller (1973)
Bénézeth and others (2018) - dolomite
Bénézeth and others (2018) - calcite - dolomite
Thorstenson and Plummer (1977)
mol% MgCO3 in bulk / surface

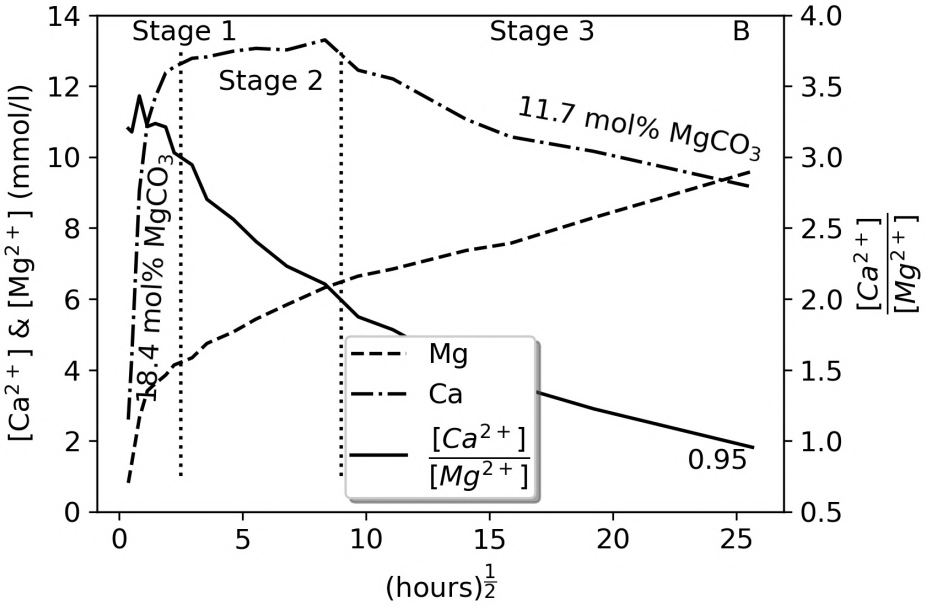
Stage 1
Stage 2
Stage 3
B
11.7 mol% MgCO3
18.4 mol% MgCO3
Mg
Ca
0.95
(hours)1/2

Fig.4A and 4B

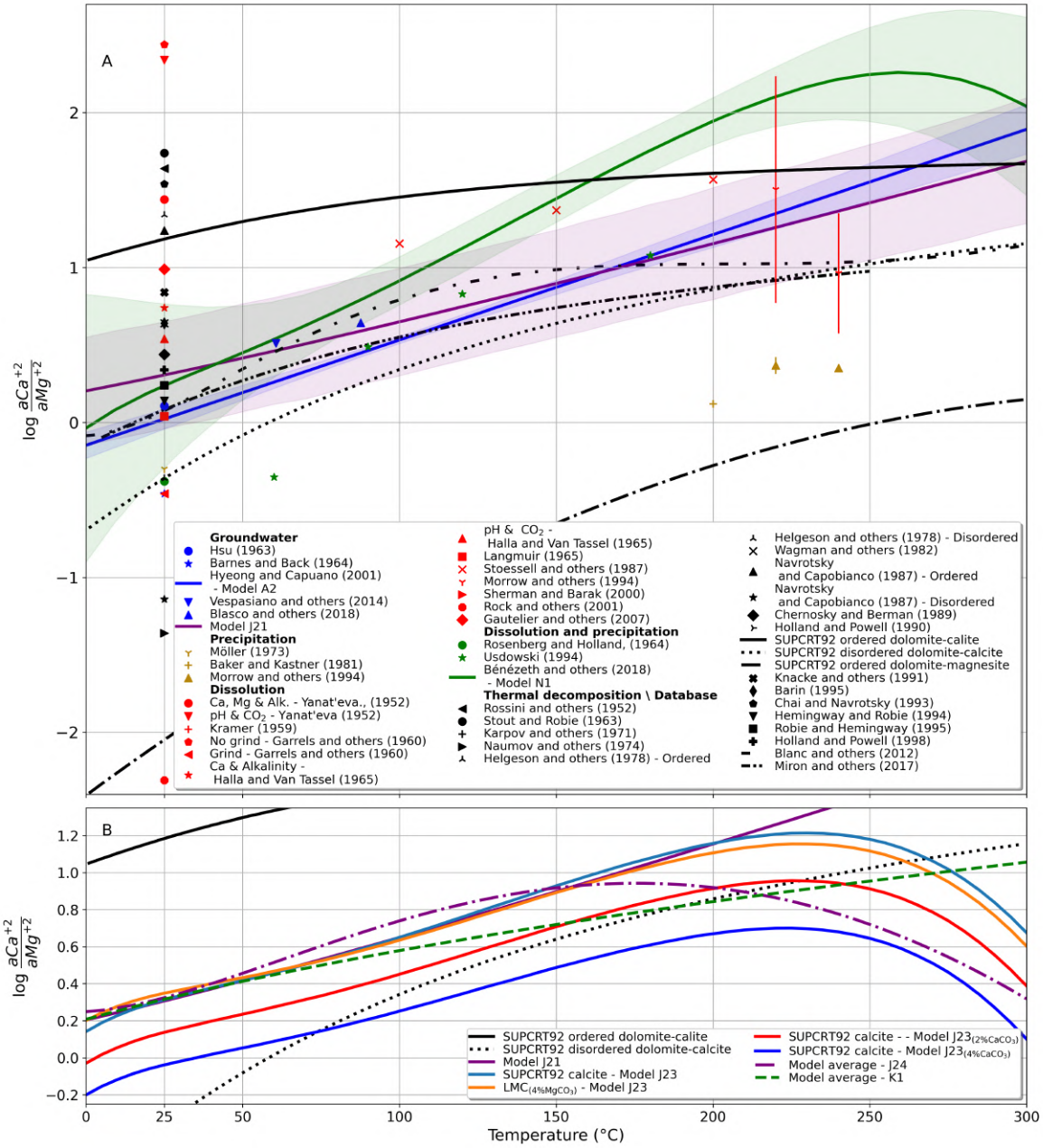
A
B
log $\frac{aCa^{+2}}{aMg^{+2}}$
Temperature (°C)
Groundwater
Hsu (1963)
Barnes and Back (1964)
Hyeong and Capuano (2001) - Model A2
Vespasiano and others (2014)
Blasco and others (2018)
Model J21
Precipitation
Möller (1973)
Baker and Kastner (1981)
Morrow and others (1994)
Dissolution
Ca, Mg & Alk. - Yanat'eva., (1952)
pH & CO_2 - Yanat'eva (1952)
Kramer (1959)
No grind - Garrels and others (1960)
Grind - Garrels and others (1960)
Ca & Alkalinity - Halla and Van Tassel (1965)
pH & CO_2 - Halla and Van Tassel (1965)
Langmuir (1965)
Stoessell and others (1987)
Morrow and others (1994)
Sherman and Barak (2000)
Rock and others (2001)
Gautelier and others (2007)
Dissolution and precipitation
Rosenberg and Holland, (1964)
Usdowski (1994)
Bénézeth and others (2018) - Model N1
Thermal decomposition \ Database
Rossini and others (1952)
Stout and Robie (1963)
Karpov and others (1971)
Naumov and others (1974)
Helgeson and others (1978) - Ordered
Helgeson and others (1978) - Disordered
Wagman and others (1982)
Navrotsky and Capobianco (1987) - Ordered
Navrotsky and Capobianco (1987) - Disordered
Chernosky and Berman (1989)
Holland and Powell (1990)
SUPCRT92 ordered dolomite-calite
SUPCRT92 disordered dolomite-calcite
SUPCRT92 ordered dolomite-magnesite
Knacke and others (1991)
Barin (1995)
Chai and Navrotsky (1993)
Hemingway and Robie (1994)
Robie and Hemingway (1995)
Holland and Powell (1998)
Blanc and others (2012)
Miron and others (2017)
SUPCRT92 ordered dolomite-calite
SUPCRT92 disordered dolomite-calcite
Model J21
SUPCRT92 calcite - Model J23
$LMC_{(4\%MgCO_3)}$ - Model J23
SUPCRT92 calcite - - Model $J23_{(2\%CaCO_3)}$
SUPCRT92 calcite - Model $J23_{(4\%CaCO_3)}$
Model average - J24
Model average - K1

Fig.5

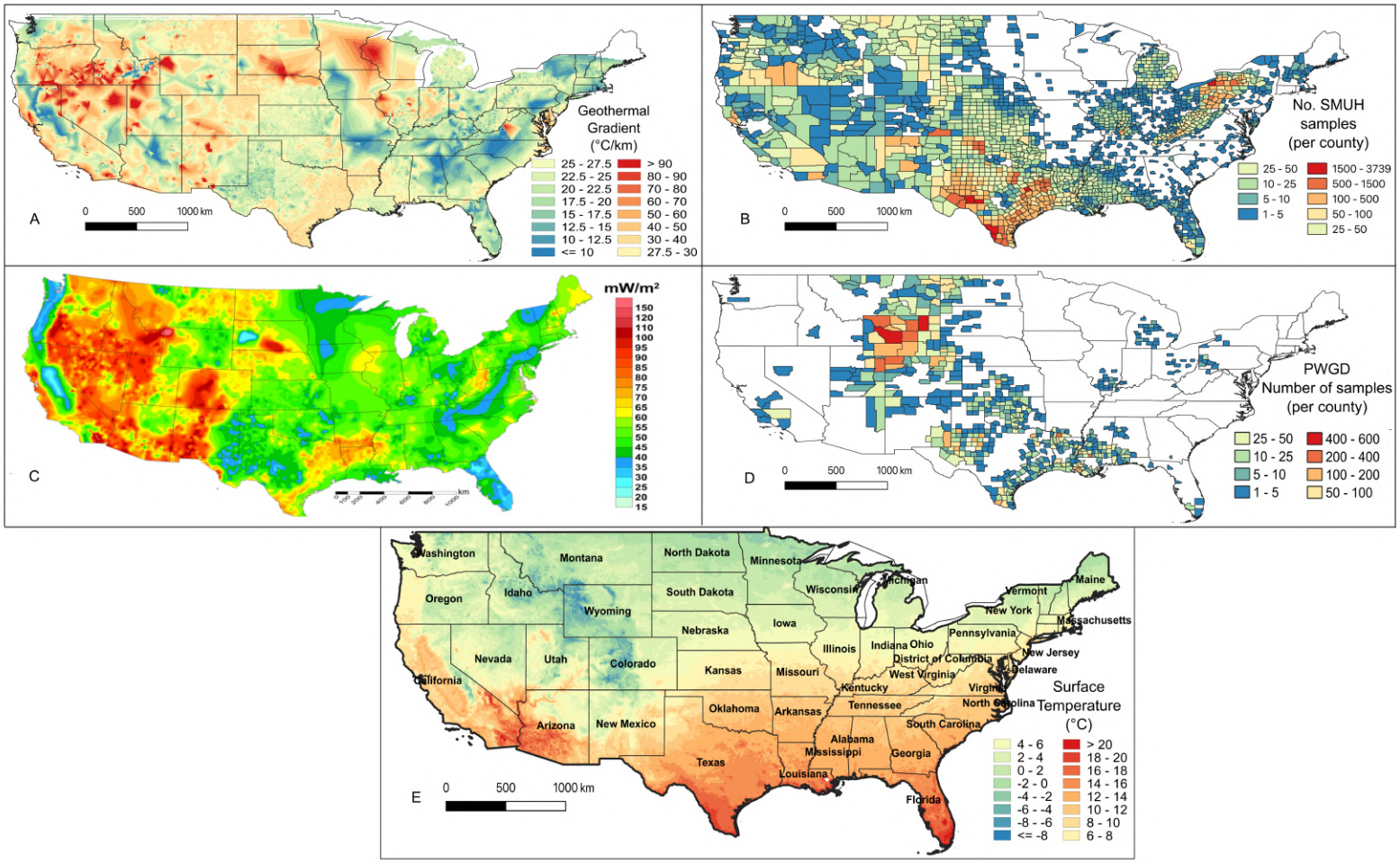
A
Geothermal Gradient (°C/km)
25 - 27.5
22.5 - 25
20 - 22.5
17.5 - 20
15 - 17.5
12.5 - 15
10 - 12.5
<= 10
> 90
80 - 90
70 - 80
60 - 70
50 - 60
40 - 50
30 - 40
27.5 - 30
0 500 1000 km
B
No. SMUH samples (per county)
25 - 50
10 - 25
5 - 10
1 - 5
1500 - 3739
500 - 1500
100 - 500
50 - 100
25 - 50
0 500 1000 km
C
mW/m²
150
120
110
100
95
90
85
80
75
70
65
60
55
50
45
40
35
30
25
20
15
D
PWGD Number of samples (per county)
25 - 50
10 - 25
5 - 10
1 - 5
400 - 600
200 - 400
100 - 200
50 - 100
0 500 1000 km
E
Washington
Oregon
California
Idaho
Nevada
Montana
Wyoming
Utah
Arizona
Colorado
New Mexico
North Dakota
South Dakota
Nebraska
Kansas
Oklahoma
Texas
Minnesota
Iowa
Missouri
Arkansas
Louisiana
Wisconsin
Illinois
Michigan
Indiana
Ohio
Kentucky
Tennessee
Mississippi
Alabama
Georgia
Florida
South Carolina
North Carolina
Virginia
West Virginia
Pennsylvania
New York
Vermont
Maine
Massachusetts
New Jersey
Delaware
District of Columbia
Surface Temperature (°C)
4 - 6
2 - 4
0 - 2
-2 - 0
-4 - -2
-6 - -4
-8 - -6
<= -8
> 20
18 - 20
16 - 18
14 - 16
12 - 14
10 - 12
8 - 10
6 - 8
0 500 1000 km

Fig. 6

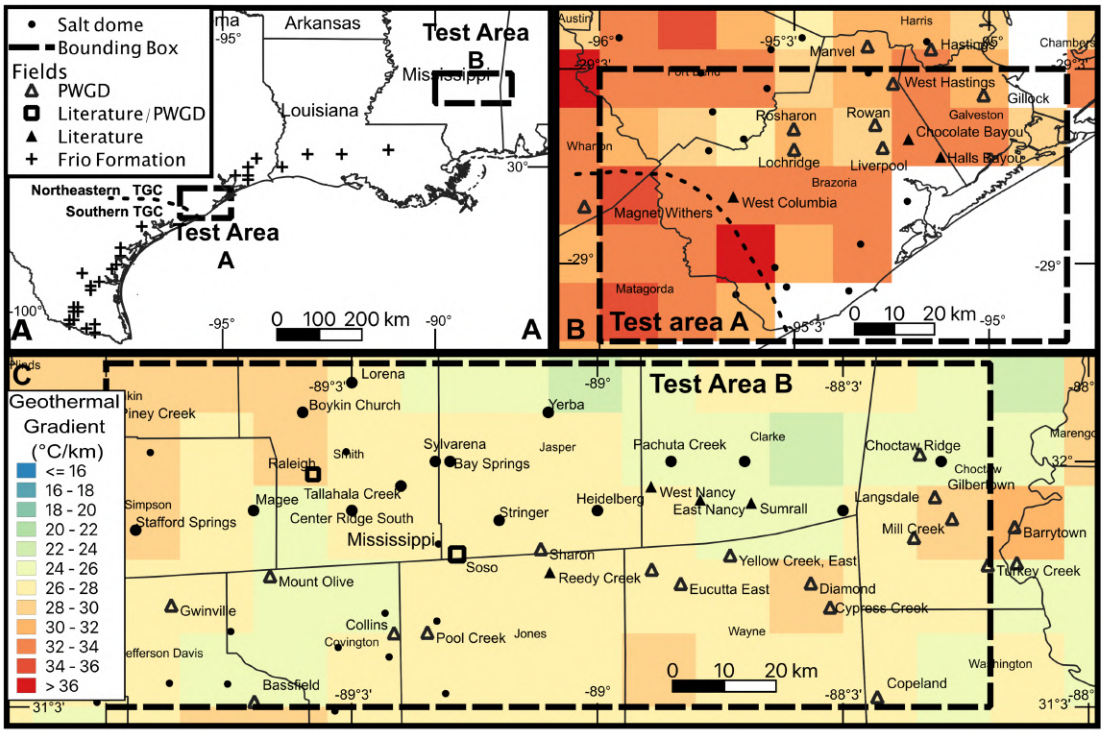
Salt dome
Bounding Box
Fields
PWGD
Literature / PWGD
Literature
Frio Formation
Arkansas
Louisiana
Test Area B
Test Area A
Northeastern TGC
Southern TGC
0 100 200 km
A
B
Test area A
0 10 20 km
Geothermal Gradient (°C/km)
<= 16
16 - 18
18 - 20
20 - 22
22 - 24
24 - 26
26 - 28
28 - 30
30 - 32
32 - 34
34 - 36
> 36
Mississippi
0 10 20 km

Fig.7

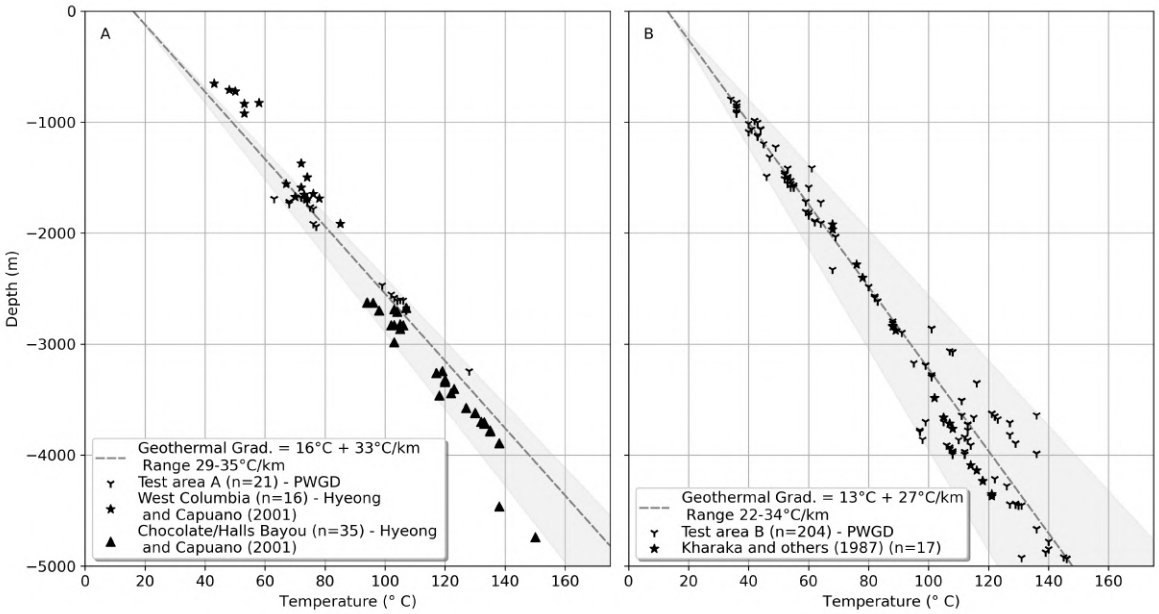
A
B
Depth (m)
0
−1000
−2000
−3000
−4000
−5000
0
20
40
60
80
100
120
140
160
Temperature (° C)
Geothermal Grad. = 16°C + 33°C/km
Range 29-35°C/km
Test area A (n=21) - PWGD
West Columbia (n=16) - Hyeong and Capuano (2001)
Chocolate/Halls Bayou (n=35) - Hyeong and Capuano (2001)
Geothermal Grad. = 13°C + 27°C/km
Range 22-34°C/km
Test area B (n=204) - PWGD
Kharaka and others (1987) (n=17)

Fig.8A and B

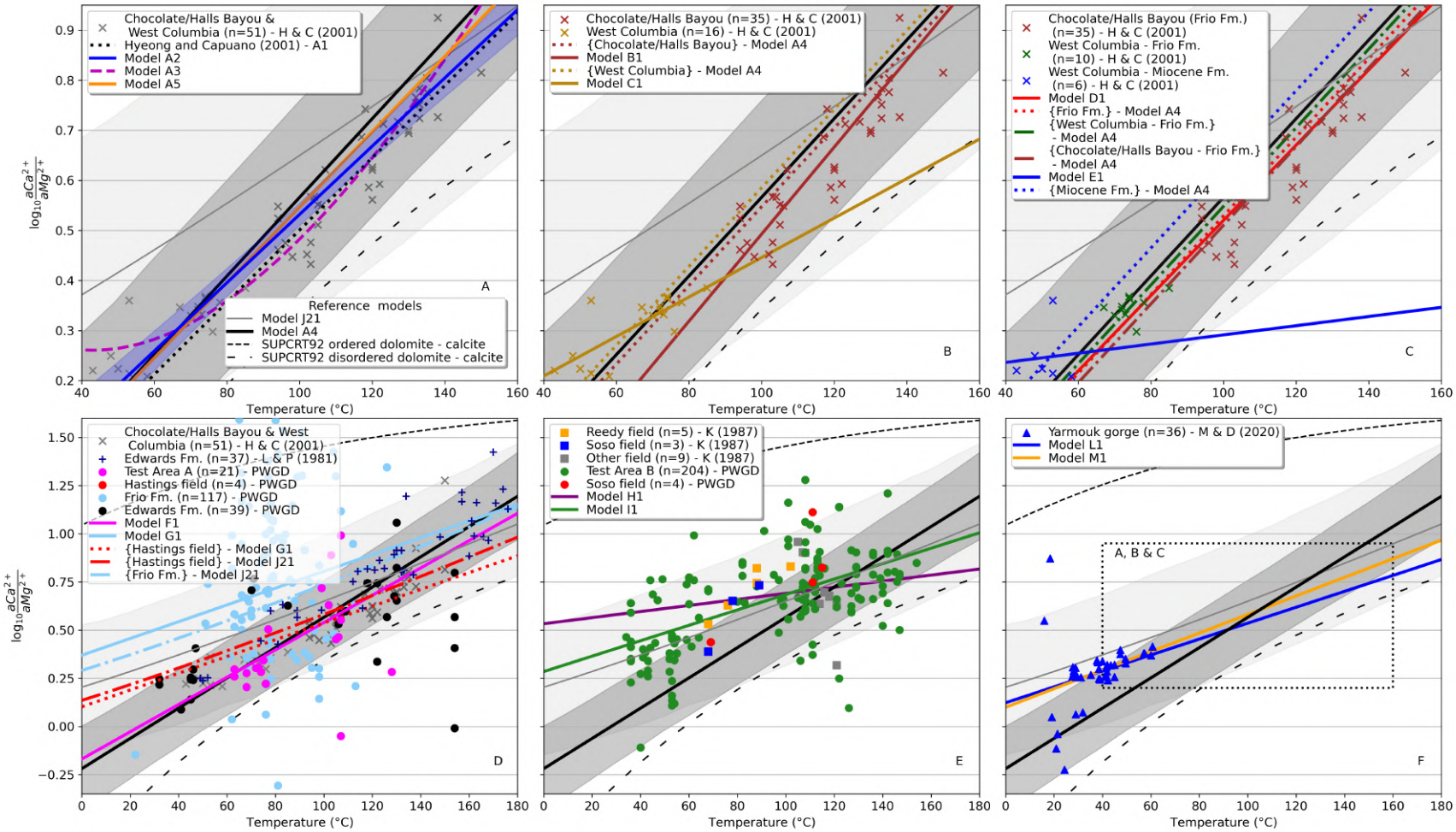
Chocolate/Halls Bayou & West Columbia (n=51) - H & C (2001)
Hyeong and Capuano (2001) - A1
Model A2
Model A3
Model A5
Reference models
Model J21
Model A4
SUPCRT92 ordered dolomite - calcite
SUPCRT92 disordered dolomite - calcite
A
Chocolate/Halls Bayou (n=35) - H & C (2001)
West Columbia (n=16) - H & C (2001)
{Chocolate/Halls Bayou} - Model A4
Model B1
{West Columbia} - Model A4
Model C1
B
Chocolate/Halls Bayou (Frio Fm.) (n=35) - H & C (2001)
West Columbia - Frio Fm. (n=10) - H & C (2001)
West Columbia - Miocene Fm. (n=6) - H & C (2001)
Model D1
{Frio Fm.} - Model A4
{West Columbia - Frio Fm.} - Model A4
{Chocolate/Halls Bayou - Frio Fm.} - Model A4
Model E1
{Miocene Fm.} - Model A4
C
Chocolate/Halls Bayou & West Columbia (n=51) - H & C (2001)
Edwards Fm. (n=37) - L & P (1981)
Test Area A (n=21) - PWGD
Hastings field (n=4) - PWGD
Frio Fm. (n=117) - PWGD
Edwards Fm. (n=39) - PWGD
Model F1
Model G1
{Hastings field} - Model G1
{Hastings field} - Model J21
{Frio Fm.} - Model J21
D
Reedy field (n=5) - K (1987)
Soso field (n=3) - K (1987)
Other field (n=9) - K (1987)
Test Area B (n=204) - PWGD
Soso field (n=4) - PWGD
Model H1
Model I1
E
Yarmouk gorge (n=36) - M & D (2020)
Model L1
Model M1
A, B & C
F
Temperature (°C)
$\log_{10}\frac{aCa^{2+}}{aMg^{2+}}$

Fig. 9

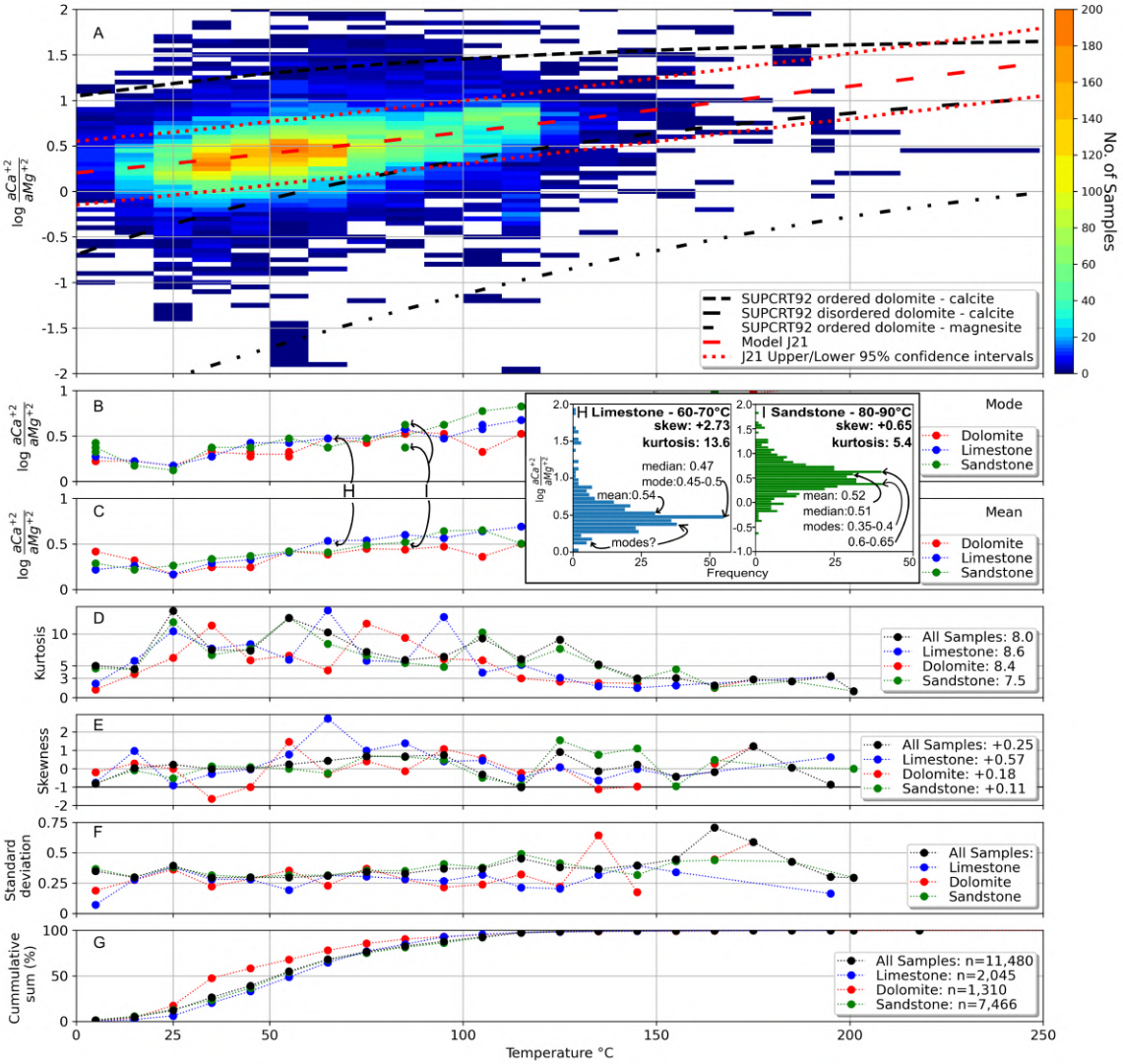
A
B
C
D
E
F
G
No. of Samples
SUPCRT92 ordered dolomite - calcite
SUPCRT92 disordered dolomite - calcite
SUPCRT92 ordered dolomite - magnesite
Model J21
J21 Upper/Lower 95% confidence intervals
H Limestone - 60-70°C
skew: +2.73
kurtosis: 13.6
median: 0.47
mode:0.45-0.5
mean:0.54
modes?
I Sandstone - 80-90°C
skew: +0.65
kurtosis: 5.4
mean: 0.52
median:0.51
modes: 0.35-0.4
0.6-0.65
Frequency
Mode
Mean
Dolomite
Limestone
Sandstone
Kurtosis
All Samples: 8.0
Limestone: 8.6
Dolomite: 8.4
Sandstone: 7.5
Skewness
All Samples: +0.25
Limestone: +0.57
Dolomite: +0.18
Sandstone: +0.11
Standard deviation
All Samples:
Limestone
Dolomite
Sandstone
Cummulative sum (%)
All Samples: n=11,480
Limestone: n=2,045
Dolomite: n=1,310
Sandstone: n=7,466
Temperature °C

Fig. 10

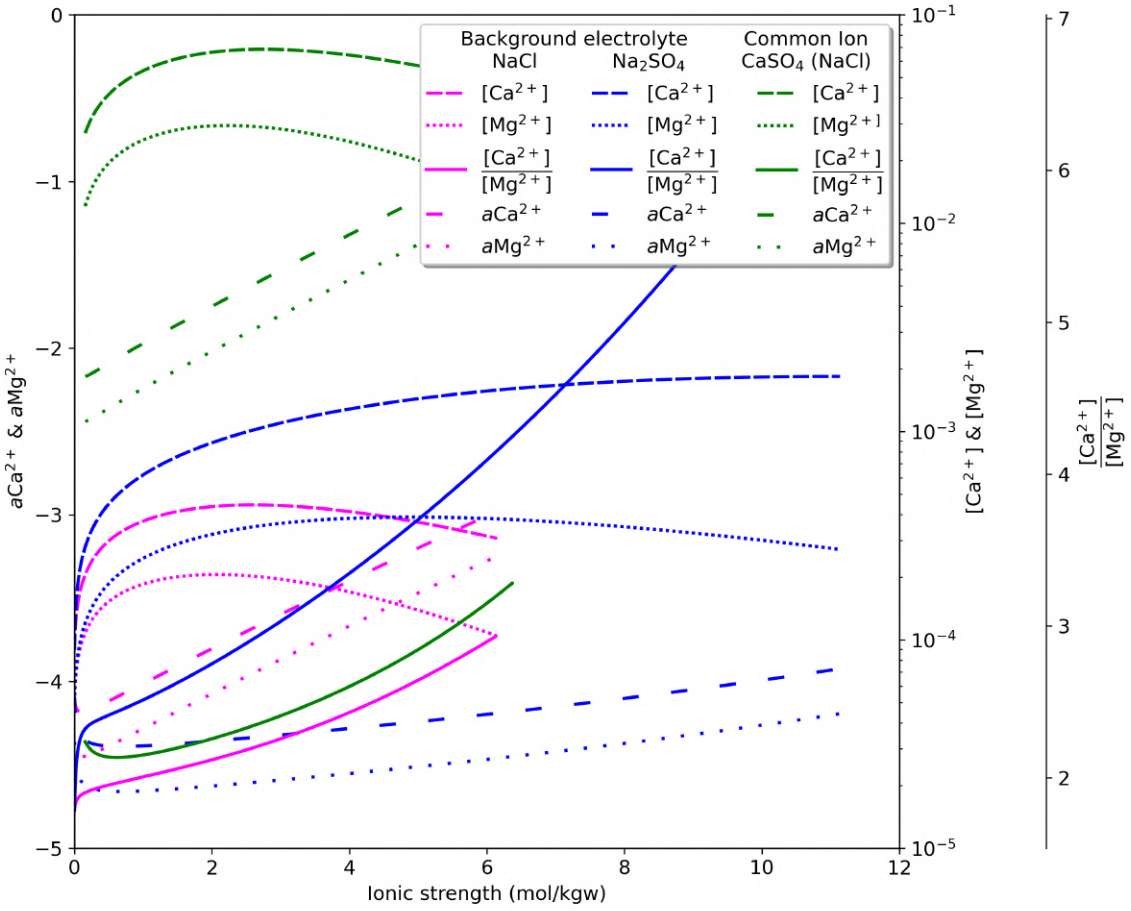
Background electrolyte
NaCl
Na_2SO_4
Common Ion
$CaSO_4$ (NaCl)
$[Ca^{2+}]$
$[Mg^{2+}]$
$\frac{[Ca^{2+}]}{[Mg^{2+}]}$
aCa^{2+}
aMg^{2+}
aCa^{2+} & aMg^{2+}
$[Ca^{2+}]$ & $[Mg^{2+}]$
$\frac{[Ca^{2+}]}{[Mg^{2+}]}$
Ionic strength (mol/kgw)

Fig. 11

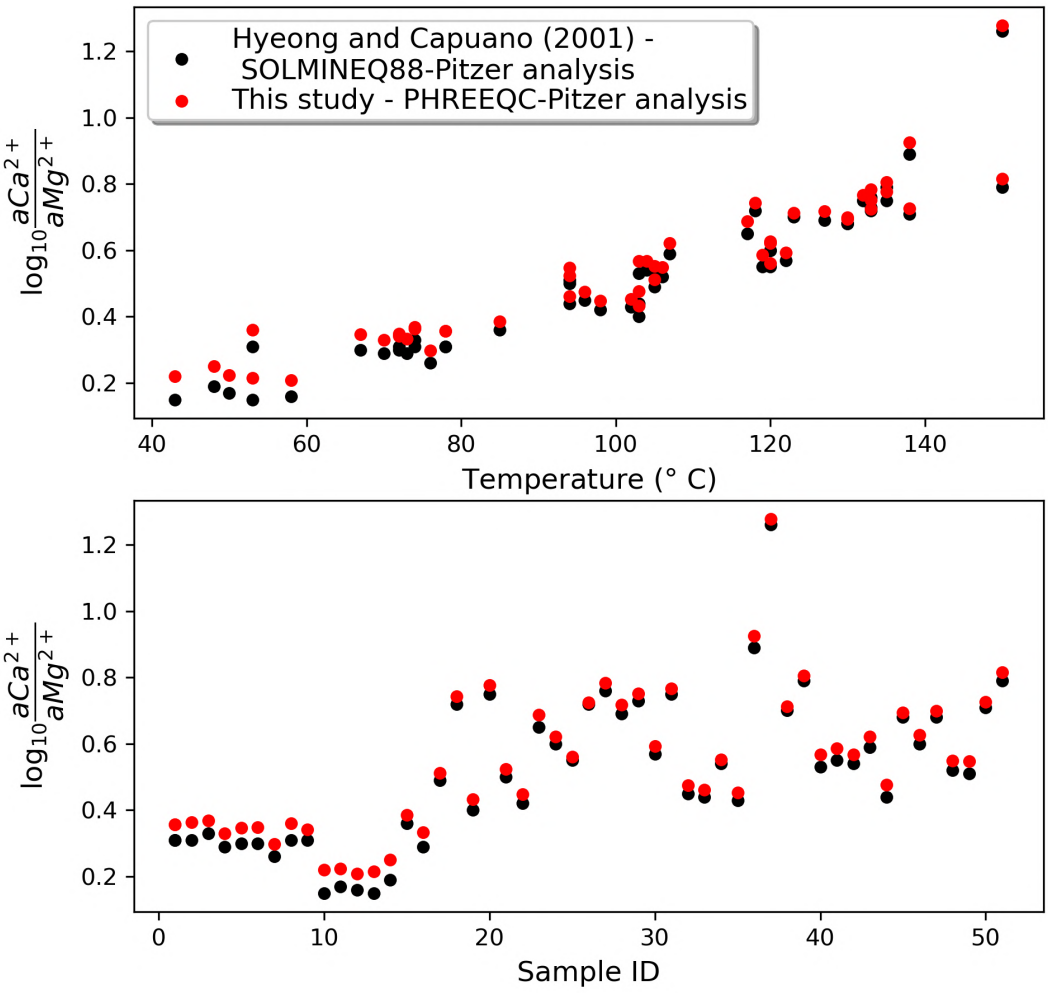

Fig. Supplementary 1

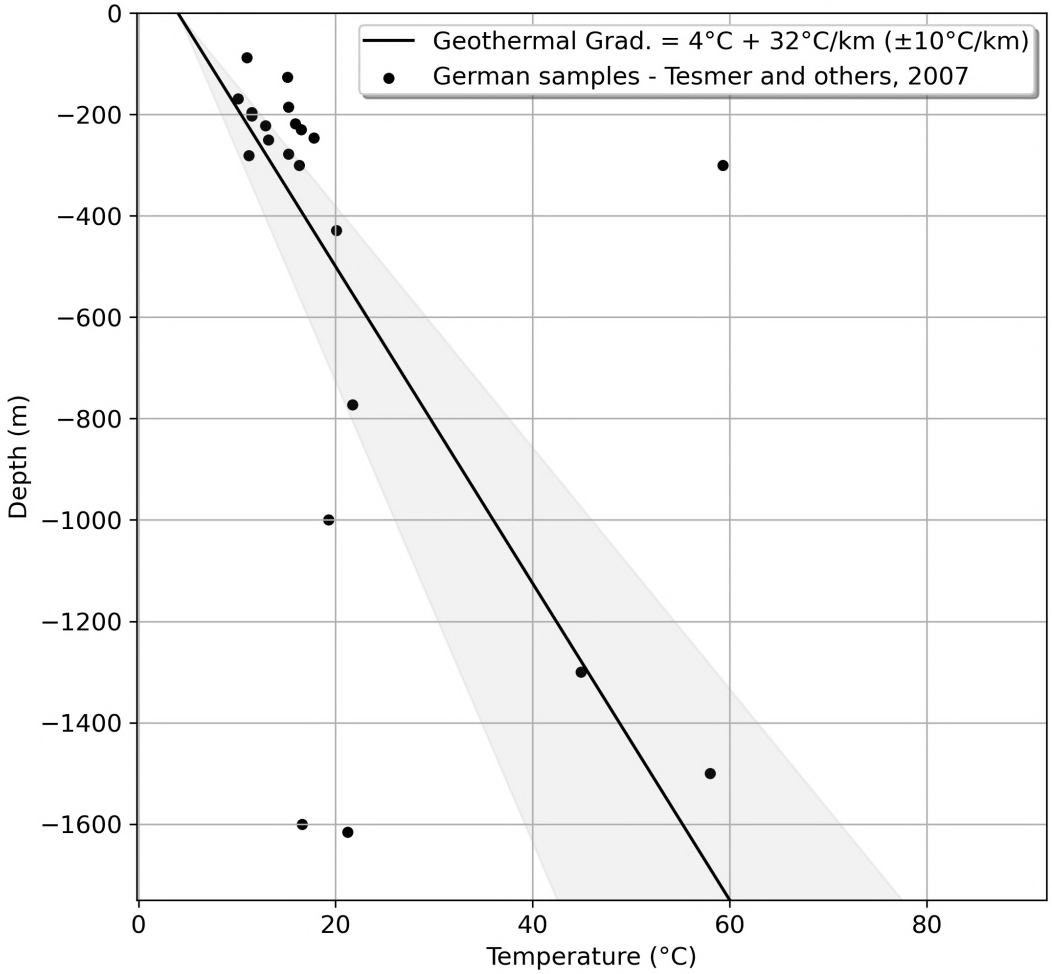

Fig. Supplementary 2

Table 1. Reference thermodynamic data for aqueous ions from Plummer and Busenberg (1982), Shock and Helgeson (1988), SUPCRT92-Johnson and others, (1992), Shock and others (1997). a, b and c are Maier-Kelly coefficients.

	Calcite	Magnesite	Mg^{2+}	Ca^{2+}	CO_3^{2-}
$\Delta_f G^\circ_{298.15}$ kJ mol^{-1}	-1129	-92.47	-453.98	-552.79	-527.98
$S^\circ_{298.15}$ J mol^{-1} K^{-1}	-92.47	-65.69	-138.10	-56.48	-50.00
$\Delta_f H^\circ_{298.15}$ kJ mol^{-1}	-1207	-1111	-465.96	-543.08	-675.24
$C^\circ_{p\ 298.15}$ J mol^{-1} K^{-1}	82.01	75.73	-21.76	-30.96	-289.53
pK_{sp}	-8.480	-8.035	-	-	-
a (10^0)	24.980	19.731	-	-	-
b (10^3)	5.240	12.539	-	-	-
c (10^{-5})	-6.200	-4.748	-	-	-

M#	Dataset - Model	Size	Type	Random	MK	$pK_{sp^{\circ}-dol}$	AIC
A1	H&C - Literature model	51	L	-	2	-16.92	-
A2	H&C	51	L	-	2	-16.98±0.07	-107.1
A3	H&C	51	M	Fi,Fo	3	-17.25±0.23	-107.4
A4	H&C	51	M	Fi,Fo	2	-16.98±0.20	-84.4
A5	H&C	51	M^1	Fi,Fo	2	-16.94±0.21	-77.1
B1	H&C - C/H Bayou	35	L	-	2	-16.80±0.18	-
C1	H&C - W.Columbia	16	L	-	2	-17.11±0.08	-
D1	H&C - Frio Fm.	45	L	-	2	-16.92±0.09	-
E1	H&C - Miocene Fm.	6	L	-	2	-17.18±0.41	-
F1	PWGD – Test Area A	21	M	Fi	2	-16.97±0.94	-
G1	PWGD – Frio Fm.	117	M	Fi	2	-17.44±0.84	-
H1	Kharaka and others (1987)	16	L	-	2	-17.52±0.40	-
I1	PWGD – Test Area B	204	M	Fi,Fo	2	-17.34±0.39	-
J1	PWGD	10,343	L	-	3	-17.24±0.02	-1455
J2	PWGD – no interval	10,343	M	D	3	-17.24±0.25	-2754
J3	PWGD – 10m	10,343	M	D	3	-17.24±0.31	-2846
J4	PWGD – 50m	10,343	M	D	3	-17.25±0.34	-3034
J5	PWGD – 100m	10,343	M	D	3	-17.25±0.34	-3086
J6	PWGD – 200m	10,343	M	D	3	-17.25±0.35	-3138
J7	PWGD – 300m	10,343	M	D	3	-17.25±0.36	-3197
J8	PWGD – 400m	10,343	M	D	3	-17.25±0.36	-3147
J9	PWGD – 500m	10,343	M	D	3	-17.25±0.36	-3153
J10	PWGD	10,343	M	Fi	3	-17.24±0.39	-2828
J11	PWGD	10,343	M	B	3	-17.26±0.44	-1815
J12	PWGD	10,343	M	Fo	3	-17.26±0.40	-2640
J13	PWGD	10,343	M	L	3	-17.23±0.45	-1524
J14	PWGD	10,343	M	P	3	-17.24±0.45	-1482
J15	PWGD	10,343	M	S	3	-17.24±0.44	-1501
J16	PWGD	10,343	M	D,Fi	3	-17.25±0.36	-3262
J17	PWGD	10,343	M	D,Fi,Fo	3	-17.26±0.34	-3534
J18	PWGD	10,343	M	D,Fi,Fo,B	3	-17.27±0.35	-3591
J19	PWGD	10,343	M	D,Fi,Fo,B,L	3	-17.27±0.35	-3590
J20	PWGD	10,343	M	D,Fi,Fo,B,L,P	3	-17.27±0.35	-3594
J21	**PWGD**	**10,343**	**M**	**D,Fi,Fo,B,L,P,S**	**3**	**-17.27±0.35**	**-3595**
J22	PWGD – ionic strength	10,343	M	D,Fi,Fo,B,L,P,S	4*	-17.28±0.35	-3600
J23	**PWGD – pK_{sp-dol}**	**10,343**	**M**	**D,Fi,Fo,B,L,P,S**	**3**	**-17.27±0.35**	**-3587**
J24	PWGD – pK_{sp-dol}	10,343	M	D,Fi,Fo,B,L,P,S	3^	-17.28±0.35	-3562
K1	PWGD	11,480	M	D,Fi,Fo,B,L,P	3	-17.28±0.51	-
K2	PWGD	11,480	M	D,Fi,Fo,B,L,P	3	-17.28±0.51	-
L1	Yarmouk; M&D (2020)	42	L	-	2	-17.19±0.08	-
M1	Yarmouk >25ºC; M&D (2020)	36	L	-	2	-17.17±0.04	-
N1	Bénézeth and others (2018)	28	L	-	3	-17.18±0.53	-

Table.2 Model (M#) summaries. Except for J23 & J24, models regress $\log_{10}({}^{a}Ca^{2+}/{}^{a}Mg^{2+})$ with temperature. H&C – Hyeong and Capuano (2001). M&D – Möller and DeLucia (2020). Type: L –linear model; M – mixed model (random intercept); M^1 – mixed model (random slope). Random effects: Fi – field; Fo – formation; D – depth; B – basin; L – lithology; P – time-period; S – time-series. MK: Number

of Maier-Kelly (fixed effect) terms. *J22 uses ionic strength as fourth fixed effect term. ^J24 β_1 term is fixed to -0.06919.

Supplementary Table 1. For selected samples and constants from table 5 of Hsu (1963); a comparison of $K_{sp°-dol}$ values calculated by Hsu (1963) and that recalculated in this study using SUPCRT92 (Johnson and others, 1992). The use of SUPCRT92 $K_{sp°-cal}$ increases the calculated $K_{sp°-dol}$ by 0.38 log units compared to that calculated with the Garrells and Drever (1952) constant. This shifts the $K_{sp°-dol}$ value from -16.69 (Hsu, 1963) to -17.07.

Eq (1) $K_{sp°-dol} = [Ca^{2+}]\,[\gamma Ca^{2+}]\,[Mg^{2+}]\,[\gamma Mg^{2+}]\,(CO_3^{2-})^2$ (from eq (4) Hsu, 1963). Hsu (1963) determines this $K_{sp°-dol}$ value to demonstrate the effect of loss of CO_2 during sampling, which produces a more soluble (larger) estimate for $K_{sp°-dol}$, and the advantage of assuming calcite-dolomite equilibrium.
Eq (2) $K_{sp°-dol}=[Mg^{2+}]\,[Ca^{2+}]\,K_{sp°-cal}^{\ 2}$ ($K_{sp°-cal}= 5.1\times10^{-9}$) (from eq (8) Hsu, 1963). Hsu (1963) determines $K_{sp°-dol}$ using the $K_{sp°-cal}$ value from Garrells and Drever (1952) of 5.1×10^{-9}.
Eq (3) $K_{sp°-dol}=[Mg^{2+}]\,[Ca^{2+}]\,K_{sp°-cal}^{\ 2}$ ($K_{sp°-cal} = 3.311\times10^{-9}$) This studies calculation of the Hsu (1963) dataset using the $K_{sp°-cal}$ value from Plummer and Busenberg (1982) as implemented in SUPCRT92 (table 1; Johnson and others, 1992).

		Sample		Hsu., (1963) average
		57-28	57-111	
Hsu (1963) observed	$Ca^{2+}\times10^{-3}$	5.5	3.35	
	$Mg^{2+}\times10^{-3}$	3.69	2.95	
	$CO_3^{2-}\times10^{-6}$	1.05	3.0	
Hsu (1963) calculated	Mg:Ca			0.78
	Eq.1	1.6×10^{-15}	5.7×10^{-16}	
	Eq.2	1.9×10^{-17}	2.3×10^{-17}	2.0×10^{-17}
This study calculated	Eq.2 $pK_{sp°-dol}$	16.73	16.64	16.69
	Eq.3	7.77×10^{-18}	9.65×10^{-18}	8.55×10^{-18}
	Eq.3 $pK_{sp°-dol}$	17.11	17.02	17.07

Authors	Experimental conditions	Thermodynamic results	K_{sp-dol} source	$pK_{sp^\circ-dol}$
Solubility (experimental)				
Yanat'eva (1952) *	25°C, CO_2=0.1 MPa, Water, 100 days, dissolution	$\Delta_f G^\circ_{298.15} = -2161.29$ kJ mol^{-1}	(Ca,Mg & Alk.) Sherman and Barak (2000)[1] Sherman and Barak (2000)[2] (pH & CO_2) Sherman and Barak (2000)[1] Sherman and Barak (2000)[2] Bénézeth and others (2018)	 -17.8 -18.4 -18.5 -19.3 -18.37
Kramer (1959)	25°C, CO_2=atmospheric, artificial seawater, variable salinity, dissolution	$K_{sp^\circ-dol} = 1.5 \times 10^{-17}$ ¶	Sherman and Barak (2000)[1] & Bénézeth and others (2018) Sherman and Barak (2000)[2]	 -16.8 -17.2
Garrels and others (1960)	25°C, CO_2=0.1 MPa, Water, 18 hours, dissolution	$\Delta_f G^\circ_{298.15} = -2175.26$ kJ mol^{-1} from Garrels and others (1960) $\Delta_f G^\circ_{298.15} = -2173.08$ kJ mol^{-1} using Table.3 $\Delta_f G^\circ_{298.15} = -2161.7$ kJ mol^{-1} per Bénézeth and others (2018)	(No grind) Sherman and Barak (2000)[1] Sherman and Barak (2000)[2] Bénézeth and others (2018) (Grind) Sherman and Barak (2000) Bénézeth and others (2018)	 -19.3 -19.4 -19.34 -16.5 -16.44
Rosenberg and Holland (1964)	275-420°C, $CaCl_2$-$MgCl_2$ soln, precipitation & dissolution	$\log_{10}({}^aCa^{2+}/{}^aMg^{2+}) = \frac{-1000}{T(\mathrm{K})} + 2.98$	This study at 25°C	-16.58
Langmuir (1965) Langmuir	25°C, Water & $MgCl_2$ soln., dissolution	$\Delta_f H^\circ_{298.15} = -2320.69$ kJ mol^{-1}	Langmuir (1965)	-17.0

(1971)				
Halla and Van Tassel (1965)	21°C, CO_2=0.1 MPa, Water, 546 days, dissolution		(Ca & Alk.) Sherman and Barak (2000)[1] Sherman and Barak (2000)[2] (pH &CO_2) Sherman and Barak (2000)[1] Sherman and Barak (2000)[2] Bénézeth and others (2018)	 -17.0 -17.7 -16.6 -17.5 -17.76
Baker and Kastner (1981)†	200°C, $CaCl_2$-$MgCl_2$ soln., 2 weeks, precipitation	$-0.03 < \log_{10}({}^{a}Ca^{2+}/{}^{a}Mg^{2+}) < 0.26$	This study at 200°C (using $\log\frac{aCa^{2+}}{aMg^{2+}}$=0.12)	(-22.21± 0.14)
Stoessell and others (1987)	100-200°C, $CaCl_2$, 300 bars, 7-8 weeks, dissolution	$\log_{10}({}^{a}Ca^{2+}/{}^{a}Mg^{2+})$ 100°C : 1.16 150°C : 1.37 200°C : 1.57	This study at 100°C (using $\log_{10}({}^{a}Ca^{2+}/{}^{a}Mg^{2+})$=-0.35)	(-19.77)
Morrow and others (1994)†	220-240°C, CO_2 variable, $CaCl_2$-$MgCl_2$ soln., 300-600 hours, precipitation & dissolution	$0.4 < \log\frac{aCa^{2+}}{aMg^{2+}} < 0.9$	This study at 230°C (using $\log_{10}({}^{a}Ca^{2+}/{}^{a}Mg^{2+})$ =0.65)	(-24.06± 0.25)
Usdowski (1967), Usdowski (1989), Usdowski (1994)	60-180°C, $CaCl_2$-$MgCl_2$ soln., < 372 weeks, precipitation & dissolution	$\log_{10}({}^{a}Ca^{2+}/{}^{a}Mg^{2+})$ 60°C : -0.35 90°C : 0.49 120°C : 0.83 180°C : 1.08	This study at 60°C (using $\log_{10}({}^{a}Ca^{2+}/{}^{a}Mg^{2+})$ = - 0.35)	(-17.25)
Sherman and	25°C, CO_2=0.101		Sherman and Barak (2000)	-17.2±0.2

Barak (2000)	MPa, Ca-Mg-HCO_3/CO_3 soln., 672 days, dissolution			
Rock and others (2001)	25°C, Cd-Hg electrodes, $CaCl_2$-$MgCl_2$ soln., Electrochemical cell, dissolution	$\Delta_f G^\circ_{298.15} = -2147.82 \pm 2.20 \text{kJ mol}^{-1}$	This study at 25°C	-14.65± 0.39
Gautelier and others (2007)	80°C, HCL-$NaHCO_3$ soln., dissolution		Gautelier and others (2007) at 80°C	(-17.95± 0.1)
Bénézeth and others (2018)	53-253°C, CO_2=variable, NaCl soln. 72-1320 hours precipitation & dissolution	$\Delta_f G^\circ_{298.15} = -2160.9 \pm 2.0 \text{ kJ mol}^{-1}$ $S^\circ_{298.15} = 156.9 \pm 2.0 \text{ J mol}^{-1}$ $\Delta_f H^\circ_{298.15} = -2323.1 \pm 2.0 \text{ kJ mol}^{-1}$ $C^\circ_{p\ 298.15} = 154.2 \pm 2.0 \text{ J mol}^{-1} \text{ K}^{-1}$	Bénézeth and others (2018) Möller and De Lucia (2020)[1] Möller and De Lucia, (2020)[2] This study statistical reanalysis of activities determined by Bénézeth and others (2018)	-17.19±0.3 -17.8 -17.5 -17.18± 0.53
Debure and others (2021)	Calcite-dolomite equilibrium, NaCl soln., 25°C & 80°C, up to 517 days	$\log_{10}({}^a\text{Ca}^{2+}/{}^a\text{Mg}^{2+})$ 25°C : -0.35 80°C : 0.49		
Solubility (groundwater)				
Hsu (1963)	22-27°C (n=28)	Average $\frac{[\text{Ca}^{2+}]}{[\text{Mg}^{2+}]} = 0.78$	Hsu (1963) Sherman and Barak (2000) This study	-16.7 -17.1 -17.07
Barnes and	No temperature	$K_{sp^\circ - dol} = (2.5 \pm 0.5) \times 10^{-17}$	Sherman and Barak (2000)	-16.5

Back (1964)‡	reported (presumably 25°C) (n=87)	$K_{sp^\circ - dol} = 2.87 \times 10^{-17}$ $K_{sp^\circ - dol} = 2.89 \times 10^{-17}$	Bénézeth and others (2018) This study	-16.54 -16.60±0.09
Hyeong and Capuano (2001) $	43 - 150°C (n=51)	$\Delta_f G^\circ_{298.15} = -2159.15$ kJ mol^{-1} $\Delta_f H^\circ_{298.15} = -2318.77$ kJ mol^{-1} s = 0.4 per eqs (129&130) of Helgeson and others (1978)	Hyeong and Capuano (2001)	-16.92
Vespasiano and others (2014) $	60.6°C (chalcedony geothermometer) (n=33)	$\Delta_f G^\circ_{333.75} = -2166.96$ kJ mol^{-1} 22% ordered dolomite per eq (10.2) of Anderson and Crerar (1993)	This study at 61°C	(-18.13)
Blasco and others (2018) $	87°C (combination geothermometer) (n=5)	$\Delta_f G_{360.15} = -2171.75$ kJ mol^{-1} 18.4% ordered dolomite per eq (10.2) Anderson and Crerar (1993)	This study at 87°C	(-18.93)
This study ¢	1.7-254.9°C (n=10,343)	Model J23 $\Delta_f G^\circ_{298.15} = -2161.34 \pm 8.26$ kJ mol^{-1} $\Delta_f H^\circ_{298.15} = -2329.61 \pm 0.51$ kJ mol^{-1} $C^\circ_{p\ 298.15} = 82.04 \pm 12.17$ J mol^{-1} K^{-1} Model J24 $\Delta_f G^\circ_{298.15} = -2161.40 \pm 0.66$ kJ mol^{-1} $\Delta_f H^\circ_{298.15} = -2332.67 \pm 0.34$ kJ mol^{-1}	J24 – fixed $C^\circ_{p\ 298.15} = 157.51$ J mol^{-1} K^{-1}	-17.27±0.35 -17.28±0.35
Thermal decomposition				
Rossini and Rossini (1952)*		$\Delta_f G^\circ_{298.15} = -2169.3$ kJ mol^{-1}	Sherman and Barak (2000)	-18.6

Stout and Robie (1963)	Bomb calorimetry	$S^{\circ}_{298.15} = 155.18\ \text{J mol}^{-1}\ \text{K}^{-1}$ $C^{\circ}_{p\ 298.15} = 157.53\ \text{J mol}^{-1}\ \text{K}^{-1}$	Sherman and Barak (2000) Bénézeth and others (2018)	-18.7 -18.2
Karpov and others (1971) *		$\Delta_f G^{\circ}_{298.15} = -2170.0\ \text{kJ mol}^{-1}$	Sherman and Barak (2000)	-18.7
Naumov and others (1974) *		$\Delta_f G^{\circ}_{298.15} = -2151.9\ \text{kJ mol}^{-1}$§ $\Delta_f G^{\circ}_{298.15} = -2121.9\ \text{kJ mol}^{-1}$§	Sherman and Barak (2000)	-15.6
Helgeson and others (1978) SUPCRT92 – slop07.dat Johnson and others (1992)	Method of Navrotsky and Loucks (1977). Using data from Goldsmith and Heard (1961)	Disordered $\Delta_f G^{\circ}_{298.15} = -2157.49\ \text{kJ mol}^{-1}$ $\Delta_f H^{\circ}_{298.15} = -2316.70\ \text{kJ mol}^{-1}$ $S^{\circ}_{298.15} = 166.69\ \text{J mol}^{-1}$ $C^{\circ}_{p\ 298.15} = 157.74\ \text{J mol}^{-1}$ Ordered(Natural) ¥ $\Delta_f G^{\circ}_{298.15} = -2166.31\ \text{kJ mol}^{-1}$ $\Delta_f H^{\circ}_{298.15} = -2328.94\ \text{kJ mol}^{-1}$ $S^{\circ}_{298.15} = 155.18\ \text{J mol}^{-1}$ $C^{\circ}_{p\ 298.15} = 157.74\ \text{J mol}^{-1}$	This study Sherman and Barak (2000) ◆ Bénézeth and others (2018) This study	-16.60 -18.09 -18.15 -18.14
Wagman and others (1982)		$\Delta_f G^{\circ}_{298.15} = -2163.4\ \text{kJ mol}^{-1}$ $\Delta_f H^{\circ}_{298.15} = -2326.3\ \text{kJ mol}^{-1}$ $S^{\circ}_{298.15} = 155.18\ \text{J mol}^{-1}$ $C^{\circ}_{p\ 298.15} = 157.53\ \text{J mol}^{-1}$	Sherman and Barak (2000) This study	-17.6 -17.63
Navrotsky and Capobianco (1987) Morrow and others (1994)	HCl solution, 358K	Disordered $\Delta_f G^{\circ}_{298.15} = -2166.31\ \text{kJ mol}^{-1}$ $\Delta_f H^{\circ}_{298.15} = -2328.94\ \text{kJ mol}^{-1}$ Ordered $\Delta_f G^{\circ}_{298.15} = -2167.02\ \text{kJ mol}^{-1}$ $\Delta_f H^{\circ}_{298.15} = -2315.89\ \text{kJ mol}^{-1}$	This study This study Sherman and Barak, 2000	-15.82 -18.26 -18.2

Chernosky and Berman (1989)		$\Delta_f G^\circ_{298.15} = -2162.4$ kJ mol^{-1}	Sherman and Barak, 2000	-17.4
Knacke and others (1991) *		$\Delta_f H^\circ_{298.15} = -2327.9$ kJ mol^{-1}	Sherman and Barak, 2000	-17.8
Chai and Navrotsky (1993)	PbO-B_2O_3 melt, 973K	$\Delta_f H^\circ_{298.15} = -2332 \pm 3$ kJ mol^{-1}	Sherman and Barak (2000)	-18.5
Barin (1995)		$\Delta_f G^\circ_{298.15} = -2163.57$ kJ mol^{-1} $\Delta_f H^\circ_{298.15} = -2326.30$ kJ mol^{-1} $S^\circ_{298.15} = 155.23$ J mol^{-1} $C^\circ_{p\ 298.15} = 157.53$ J mol^{-1}	This study Sherman and Barak, 2000	-17.66 -17.6
Robie and others (1978) Hemingway and Robie (1994) Robie and Hemingway (1995)	300.15K, HCl soln.	$\Delta_f G^\circ_{298.15} = -2161.3 \pm 1.7$ kJ mol^{-1} $\Delta_f H^\circ_{298.15} = -2324.5 \pm 1.6$ kJ mol^{-1} $S^\circ_{298.15} = 155.2$ J mol^{-1} $C^\circ_{p\ 298.15} = 157.51$ J mol^{-1}K^{-1}	Robie and others (1978) & Hemingway and Robie (1994) 1) Sherman and Barak (2000) 2) Sherman and Barak (2000) Bénézeth and others (2018) This study	-17.09±0.37 -17.1 -17.2 -17.12 17.26± 0.3
Database				
Holland and Powell (1990)		$\Delta_f H^\circ_{298.15} = -2325.72$ kJ mol^{-1} $S^\circ_{298.15} = 155.2$ J mol^{-1} $C^\circ_{p\ 298.15} = 157.52$ J mol^{-1}K^{-1}	Sherman and Barak, 2000	-17.4
Holland and Powell (1998)		$\Delta_f G^\circ_{298.15} = -2161.51$ kJ mol^{-1} $\Delta_f H^\circ_{298.15} = -2324.56$ kJ mol^{-1} $S^\circ_{298.15} = 156.0$ J mol^{-1} $C^\circ_{p\ 298.15} = 157.28$ J mol^{-1}K^{-1}	This Study	-17.30
Blanc and others (2012) Thermoddem			Dolomite Ordered Dolomite Disordered Dolomite	-17.12 -17.90 -16.35

v.2017				
Miron and others (2017)			New aqueous model using Holland and Powell (1998) mineral data	-17.0

Supplementary Table 2 Literature reported standard state thermodynamic properties of dolomite and $pK_{sp^\circ-dol}$ values largely compiled from Sherman and Barak (2000) and Bénézeth and others (2018). Minor discrepancies between the two are due mostly to differing methods and reference thermodynamic data sets used during calculation from the sources. We report the original author $pK_{sp^\circ-dol}$, $pK_{sp^\circ-dol}$ values where they differ from those recalculated by Sherman and Barak (2000) or Bénézeth and others (2018), and any recalculations by this study (using reference data from table 1) that represent or entirely new values or significant refinements (change in $pK_{sp^\circ-dol} > 0.1$). Estimates for pK_{sp-dol} that are not at reference temperature (25°C) are reported in parentheses. Some entries, such as Robie and Hemingway (1995) and Johnson and others (1992), represent notable significant recalculations of original experimental data (Robie and others (1978) and Helgeson and others (1978) in this case respectively) and multiple studies are listed in the 'authors column' that synthesize and reflect the heritage of the more frequently referenced analyses; the $pK_{sp^\circ-dol}$ value for the most recent study is given in the $pK_{sp^\circ-dol}$ column. Sherman and Barak (2000) present multiple recalculations of $pK_{sp^\circ-dol}$ using different methods/data sources and these are reported here in the order they appear in the original source. Apart from Kramer (1959), unique in using a synthetic seawater composition, experimental solubility is determined using distilled/pure water ('Water') or a solution ('soln.') consisting of a specific electrolyte (e.g. $MgCl_2$).

*The original source for Yanat'eva (1952), Rossini and Rossini (1952), Karpov and others (1971), Naumov and others (1974), Knacke and others (1991) were not available and we report the data as sourced from Sherman and Barak (2000) and Bénézeth and others (2018).

¶The data for Kramer (1959) reported by Sherman and Barak (2000) and Bénézeth and others (2018) this study believes is in error, and instead $K_{sp^\circ-dol}=1.5\times10^{-17}$ is reported from the original source.

†Baker and Kastner (1981) and Morrow and others (1994) do not regress the high temperature experimental data to reference state conditions and instead report experimental ranges; a single average value determined by this study is used to represent the $pK_{sp^\circ-dol}$.

‡The value of $K_{sp^\circ-dol}= 2.89 \times 10^{-17}$ reported by Sherman and Barak (2000) appears to be a transcription error. Barnes and Back (1964) present a range ($K_{sp^\circ-dol} = 2\text{-}3 \times 10^{-17}$) over which they interpret $K_{sp^\circ-dol}$. The value $K_{sp^\circ-dol}=2.87 \times 10^{-17}$ represents the maximum ion activity product for dolomite as reported by Barnes and Back (1964) and corresponds to the $pK_{sp^\circ-dol}$ reported by Bénézeth and others (2018).

§There is likely a transcription error on the part of either Sherman and Barak (2000) ($\Delta_f G^\circ_{298.15} = -2151.9\ \mathrm{kJ\ mol^{-1}}$) or Bénézeth and others (2018) ($\Delta_f G^\circ_{298.15} = -2121.9\ \mathrm{kJ\ mol^{-1}}$).

♦ The $pK_{sp^\circ-dol}$ from Sherman and Barak (2000) uses the original Helgeson and others (1978) thermodynamic properties not reported here.

¢ Reported uncertainties associated with the thermodynamic properties are derived using the standard error otherwise uncertainties associated $pK_{sp^\circ-dol}$ values are computed using 95% confidence intervals.

$ There are two distinct (but related) methods of estimating ordering parameter; a) the standard Helgeson and others (1978) method as used by Hyeong and Capuano (2001) and easily relatable to crystallographic measurements and b) the Anderson and Crerar (1993) % of ordered dolomite method as used by Vespasiano and others (2014) and Blasco and others (2018). However the Anderson and Crerar (1993) method, though initially easier to calculate is not easily converted to *s* values (and is not attempted here as this study discounts the influence of natural dolomite order and favoring dolomite stoichiometry). Equilibrium $\log_{10}({}^{a}Ca^{2+}/{}^{a}Mg^{2+})$ values are higher for both Vespasiano and others (2014) and Blasco and others (2018) compared to Hyeong and Capuano (2001) which classically suggests the presence of a 'more ordered' or, as this study interprets, a more stoichiometric dolomite phase.

¥ - Most databases, such as slop07, have the same properties for the ordered and natural (i.e. just 'Dolomite') phases suggesting the natural (*s*=0.7) phase has fallen out of usage though Blanc and others (2012) preserved a natural dolomite phase which we presume is related to the Helgeson (1978) phase.

This study	Failing criteria (%)	Hitchon and Brulotte (1994)	Blondes and others (2016)	Possible causes/Reason for criteria
3.5>pH>11	26.8	5>pH >11	4.5>pH >10.5	Low pH due by acid wash treatment. High pH caused by cement wash or mud filtrate
Charge balance > ±15%	43.1	Charge balance >±15%	Charge balance >±15%	Poor quality analysis or transcription errors
Mg or Ca concentrations missing	22.4	Any of Ca, Mg, Cl or SO4, with either HCO3 or alkalinity, zero, missing, or reported as <or >value	N/A	Incomplete analysis, insufficient sample or very low concentration.
N/A	-	Mg>=Ca	Mg>Ca	Loss of CO^2 (and Ca^{2+} in solution) and precipitation of $CaCO_3$ due to delayed analysis. Low overall concentrations. Incorrect entry of Ca+Mg as equivalent Ca, as separate Ca and Mg values.
N/A	-	OH reported	N/A	Wash from cement. Poor analysis
N/A	-	CO_3 reported	N/A	Drilling mud contamination (without significant effect on pH). Poor sampling of separator or treater.
N/A	-	$(K/Na) \times 10^3$ >stratigraphic unit specific value	K>Cl or K>5×Na	Contamination by KCl mud
N/A	-	Fe >100mg/l	N/A	Contamination from corrosion products of well
No depth	29.9	N/A	N/A	Must be assignable to a specific depth
No aquifer lithology.	84.84	N/A	N/A	Lithologies such as 'other', 'conglomerate', coal (n=33) and anhydrite (n=18) are culled.
No Lat/Lon	7.1	N/A	N/A	Presence of Lat/Lon is required to estimate temperature at formation-depth.

Supplementary Table 3. Geochemical and geospatial/other rejection criteria used to filter the PWGD and the rejection criteria used by Hitchon and Brulotte (1994) and Blondes and others (2016). Of the entire database (n=165,960) 93% of all samples failed to meet the criteria specified in this study, leaving a final population of n=11,840. N/A is not applicable; this criteria is not used to discriminate against a sample's inclusion in the dataset.

Lithology	Description	Pre-SUPCRT (n=11,480)	Post-SUPCRT (n=10,343)
Sandstone	All sand and siltstone lithologies, including those with mention of subsidiary anhydrite and shale. No carbonate can be reported.	7466 (65.0%)	6675 (64.5%)
Dolomite	Dolomite lithologies including those with mention of subsidiary anhydrite, sandstone, siltstone, shale or chert. No limestone can be reported.	1310 (11.4%)	1176 (11.4%)
Limestone	Limestone lithologies including those with mention of subsidiary anhydrite, sandstone, siltstone, shale or chert. No dolomite can be reported.	2045 (17.8%)	1907 (18.4%)
Mixed Carbonate	Dolomite and limestone lithologies including those with mention of subsidiary anhydrite, sandstone, siltstone, shale or chert. Also includes 'carbonate', chalk and chert lithologies.	500 (4.4%)	439 (4.2%)
Shale	Shale lithology. Can mention only 1 other minor lithology e.g. anhydrite, chert	159 (1.4%)	146 (1.4%)

Supplementary Table 4. Classification of samples by lithology. Two datasets are presented; 1) the PWGD dataset (n=11,480) which is simulated using PHREEQC 2) the 90.89% of these samples (n=10,343) with $\log_{10}({}^{a}Ca^{2+}/{}^{a}Mg^{2+})$ ratios between SUPCRT92-ordered-calcite-dolomite & disordered-dolomite - calcite equilibriums (temperature-dependent) which were used in the principal regression analysis.

Supplementary Table 5: Summary statistics describing the PWGD dataset (n=11,480), including the mean value, 1 standard deviation (std), minimum (min) and maximum (max), together with percentiles P25, P50 and P75. Variables denoted by (1) are from the PWGD (Blondes and others, 2016). Geothermal gradients(2) are derived from the interpolation of SMUH dataset (Blackwell and others, 2011). Mean annual land surface temperatures at well sites(3) derive from a reprocessing of the MAST dataset for North America (Bechtel, 2015). Temperature at formation-depth(4) is calculated using the depth, geothermal gradient and the surface temperature. Because of the minimal amount of available pressure data and generally negligible effect on $\log_{10}({}^{a}Ca^{2+}/{}^{a}Mg^{2+})$, this data is excluded from the PHREEQC analysis. Activities and ionic strengths of fluids(5) calculated in this study using by PHREEQC with the Pitzer database are determined at formation-depth temperatures.

	count	mean	std	min	P25	P50	P75	max
Depth(1) (km)	11480	1.955	0.930	0.028	1.301	1.854	2.529	6.779
Geothermal gradient(2) (°C/km)	11480	27.81	6.1	11.0	23.6	27.3	32.0	87.5
Mean Annual Surface Temperature(3) (°C)	11480	7.6	6.4	-5.0	1.0	9.0	13.0	21.0
Temperature at formation-depth(4) (°C)	11480	61.9	29.3	1.7	39.6	57.6	79.0	254.9
Pressure(1) (psi)	188	3504	1417	456	2488	3480	4308	10929
Specific Gravity(1) (g/cm^3)	8233	1.1	0.1	1.0	1.0	1.0	1.1	1.5
Resistivity(1) (S/m)	9057	0.8	1.2	0.0	0.1	0.2	0.9	8.0
pH(1)	11480	7.05	1.1	3.5	6.4	7.1	7.9	11.0
Total dissolved solids(1) (mg/l)	11480	84200	92125	784	9025	42745	140876	409204
Charge Balance (%)(1)	11480	0.3	2.0	-14.9	0.0	0.0	0.0	14.7
Mg(1) (mg/l)	11480	886	1613	1	43	282	1123	26210
Ca(1) (mg/l)	11480	5353	9135	2	196	1280	6160	74200
Ionic Strength(5) (mol/kgw)	11480	2.05	2.57	0.02	0.18	0.85	3.05	13.81
aMg^{2+} (5)	11480	-2.46	1.23	-5.35	-3.39	-2.51	-1.70	2.17
aCa^{2+} (5)	11480	-2.04	1.25	-4.89	-2.94	-2.11	-1.19	2.24

Model	A1	A2	A3	A4	A5
Model Type (RE)	Linear	Linear	Mixed (2)	Mixed (2)	Mixed (2)
Samples	51	51	51	51	51
a (SE)	-2.20×10^{-1}	-2.01 (1.49×10^{-1})	-1.59×10^{1} (4.00)	-2.37 (2.44×10^{-1})	-2.26 (2.38×10^{-1})
t/p	-	-13.44, $<2.22\times10^{-16}$	-3.97, 1.04×10^{-1}	-9.69, 8.64×10^{-5}	-9.49, 2.00×10^{-1}
b (SE)	7.21	6.80×10^{-3} (3.97×10^{-4})	2.56×10^{-2} (5.36×10^{-3})	7.86×10^{-3} (6.66×10^{-4})	7.53×10^{-3} (6.06×10^{-4})
t/p	-	17.13, $<2.22\times10^{-16}$	4.77, 6.37×10^{-2}	11.80, 2.03×10^{-5}	12.42, 1.01×10^{-4}
c (SE)	-	-	2.56×10^{3} (7.41×10^{2})	-	-
t/p	-	-	3.45, 1.41×10^{-1}	-	-
^Field I.(G.)	-	-	0.00	3.57×10^{-2}	1.93×10^{-1} (4.63×10^{-4})
^Formation I.(G.)	-	-	2.76×10^{-2}	5.91×10^{-2}	8.64×10^{-2} (1.23×10^{-4})
Residual	-	-	7.21×10^{-2}	7.77×10^{-2}	7.76×10^{-2}
#ICC	-	-	-	0.441	-
*R^2 m/c & a	0.94	0.86	0.87/0.88	0.83/0.90	0.85/0.89
$pK_{sp^{\circ}-dol}$ 25°C	-16.92	-16.98	-17.25	-16.98	-16.94
†CI 25°C l/u (dif)	-	-16.92/-17.05 (0.13)	-17.48/-17.03 (0.45)	-17.15/-16.76 (0.39)	-17.15/-16.73 (0.42)
$pK_{sp^{\circ}-dol}$ 200°C	-23.32	-23.31	-23.69	-23.45	-23.40
CI 200°C l/u (dif)	-	-23.23/-23.40 (0.17)	-23.95/-23.43 (0.52)	-23.55/-23.15 (0.39)	-23.60/-23.19 (0.41)
AIC	-	-107.1	-107.4	-84.4	-77.1

Supplementary Table. 6. For each coefficient estimate (e.g. 'a'); (SE) represents the standard error associated with the estimate. For each coefficient the 't/p' represents; 't' – the t-test associated with the significance of the coefficient estimate and 'p' – the p-value for that t-test. # The intraclass correlation coefficient (ICC) reports the adjusted and conditional ICC. Both ICC values account for all sources of uncertainty but the conditional ICC differs from the adjusted ICC by incorporating the variance associated with the fixed effects; as is common practice we report only the adjusted value. At small sample sizes, using mixed models suffering from singularity in regression analysis, ICC sometimes fails to report. *Reported R^2 values are the marginal (m) and conditional (c) R^2 values for mixed models and the adjusted (a) R^2 for linear models. †The lower (l) and upper (u) confidence intervals (CI) are accompanied by a calculation of the difference between them (dif).^For each random effect usually only the $\log_{10}({}^{a}Ca^{2+}/{}^{a}Mg^{2+})$ intercept 'I.' is reported; these are termed random intercept models and the most common type of model used by this study. For random slope models both the intercept 'I.' and also the gradient for the increase in $\log_{10}({}^{a}Ca^{2+}/{}^{a}Mg^{2+})$ with temperature '(G.)' are reported. If a random effect is implemented it is reported; in some cases, e.g. Field for M2, a random effect has zero effect but is still reported as 0.00. For clarity and convenience the total number of random effects '(RE)' implemented is reported in the brackets for the Model Type. Unless otherwise stated models use a 2,3 or 4 term formulation of the Maier-Kelly regression formulae eq (25) with the total number of terms used reflected by the number of coefficients (a, b, c and d) reported. A1. Original Hyeong and Capuano (2001) model for Hyeong and

Capuano (2001) dataset. Activities calculated by SOLMNEQ88-Pitzer and fit to eq (28) (note equation is in celsius-see text). A2. Linear model of the Hyeong and Capuano (2001) dataset with activities calculated using PHREEQC-Pitzer. A3. Three term (fixed effect) mixed model of Hyeong and Capuano (2001) dataset. The model incorporates the field and formation attributes as random effects. This three-term model produces a clearly spurious fit (fig. 5a). A4. Two term (fixed effect) mixed model of Hyeong and Capuano (2001) dataset. A5. A random slope (all others are random intercept) mixed model of the Hyeong and Capuano (2001) dataset.

Model	B1	C1	D1	E1	F1
Model Type	Linear	Linear	Linear	Linear	Mixed (1)
Samples	35	16	45	6	21
a (SE)	-2.75 (3.56×10^{-1})	-1.03 (2.81×10^{-1})	-2.28 (1.96×10^{-1})	-5.06×10^{-2} (1.81)	-2.11 (1.55)
t/p	-7.73, 6.62×10^{-9}	-3.65, 2.65×10^{-3}	-11.65, 6.84×10^{-15}	-2.79×10^{-2}, 9.79×10^{-1}	-1.36, 0.21
b (SE)	8.69×10^{-3} (9.08×10^{-4})	3.94×10^{-3} (8.30×10^{-4})	7.51×10^{-3} (5.13×10^{-4})	9.17×10^{-4} (5.60×10^{-3})	7.09×10^{-3} (4.29×10^{-3})
t/p	9.57, 4.82×10^{-11}	4.75, 3.11×10^{-4}	14.65, 2.22×10^{-16}	1.64×10^{-1}, 8.78×10^{-1}	1.65, 1.37×10^{-1}
Field I.(G.)	-	-	-	-	8.02×10^{-2}
Formation I.(G.)	-	-	-	-	-
Residual	8.65×10^{-2}	4.05×10^{-2}	8.01×10^{-2}	6.40×10^{-2}	3.43×10^{-1}
ICC	-	-	-	-	-
R^2 m/c & a	0.74/0.73	0.62/0.59	0.83/0.83	6.66×10^{-3}/-0.24	0.13/0.18
$pK_{sp°—dol}$ 25 °C	-16.80	-17.11	-16.92	-17.18	-16.97
CI 25°C l/u (dif)	-16.63/-16.98 (0.35)	-17.04/17.19 (0.15)	-16.83/17.01 (0.18)	-16.73/-17.59 (0.82)	-16.03/-17.90 (1.87)
$pK_{sp°—dol}$ 200 °C	-23.46	-22.94	-23.37	-22.48	-23.35
CI 200°C l/u (dif)	-23.31/-23.61 (0.31)	-22.70/-23.18 (0.48)	-23.27/-23.47 (0.20)	-20.16/-24.80 (4.64)	-22.12/-24.57 (2.45)
AIC	-	-	-	-	-

B1. Model of the Chocolate/Halls Bayou subset from the Hyeong and Capuano (2001) dataset. C1. Model of the West Columbia subset from the Hyeong and Capuano (2001) dataset. D1. Model of the Frio Fm. subset from the Hyeong and Capuano (2001) dataset. E1. Model of the Miocene Fm. subset from the Hyeong and Capuano (2001) dataset. F1. Model of PWGD samples contained within Test Area A (all samples are from the Frio Fm.).

Model	G1	H1	I1
Model Type	Mixed (2)	Linear	Mixed (2)
Samples	117	16	204
a (SE)	-8.20×10^{-1} (1.01)	4.02×10^{-2} (9.24×10^{-1})	-8.09×10^{-1} (3.04×10^{-1})
t/p	-8.08×10^{-1}, 4.21×10^{-1}	4.35×10^{-2}, 9.66×10^{-1}	-2.66 (9.33×10^{-3})
b (SE)	4.36×10^{-3} (2.84×10^{-3})	1.75×10^{-3} (2.49×10^{-3})	4.00×10^{-3} (8.50×10^{-4})
t/p	1.54, 1.28×10^{-1}	7.05×10^{-1}, 4.92×10^{-1}	4.71, 9.26×10^{-6}
Field I.(G.)	2.63×10^{-1}	-	1.69×10^{-1}
Formation I.(G.)	-	-	1.31×10^{-1}
Residual	3.77×10^{-1}	1.80×10^{-1}	1.82×10^{-1}
ICC	0.328	-	0.579
R^2 m/c & a	0.02/0.34	-0.03	0.19/0.66
$pK_{sp°—dol}$ 25 °C	-17.44	-17.52	-17.34
CI 25°C l/u (dif)	-16.61/-18.27 (1.67)	-17.92/-17.12 (0.80)	-16.96/-17.73 (0.77)
$pK_{sp°—dol}$ 200 °C	-23.34	-22.97	-23.18
CI 200°C l/u (dif)	-22.35/-24.33 (1.98)	-22.41/-23.52 (1.11)	-22.76/-23.60 (0.84)
AIC	-	-	-

G1. Model of all Frio Fm. samples present in PWGD. H1. Model of the Kharaka and others (1987) dataset. I1. Model of all PWGD samples contained within Test Area B.

Model	J1	J2 – n=(8201)	J3 – 10m (n=6217)	J4 – 50m (n=4574)	J5 - 100m (n=3985)
Model Type	Linear	Mixed (1)	Mixed (1)	Mixed (1)	Mixed (1)
Samples	10343	10343	10343	10343	10343
a (SE)	-3.76 (4.87×10^{-1})	-3.64 (5.58×10^{-1})	-3.62 (5.97×10^{-1})	-3.65 (6.34×10^{-1})	-3.58 (6.48×10^{-1})
t/p	-7.71, 1.37×10^{-14}	-6.53, 6.93×10^{-11}	-6.07, 1.38×10^{-9}	-5.76, 9.14×10^{-9}	-5.52, 3.52×10^{-8}
b (SE)	8.90×10^{-3} (7.20×10^{-4})	8.72×10^{-3} (8.26×10^{-4})	8.61×10^{-3} (8.85×10^{-4})	8.63×10^{-3} (9.38×10^{-4})	8.52×10^{-3} (9.58×10^{-4})
t/p	1.24×10^{1}, $<2.22\times10^{-16}$	1.06×10^{1}, $<2.22\times10^{-16}$	9.74, $<2.22\times10^{-16}$	9.20, $<2.22\times10^{-16}$	8.89, $<2.22\times10^{-16}$
c (SE)	4.13×10^{2} (8.21×10^{1})	3.93×10^{2} (9.37×10^{1})	3.99×10^{2} (1.00×10^{2})	4.07×10^{2}, 1.07×10^{2}	3.96×10^{2} (1.09×10^{2})
t/p	5.03, 4.89×10^{-7}	4.19, 2.79×10^{-5}	3.98, 7.05×10^{-5}	3.82, 1.37×10^{-4}	3.63, 2.86×10^{-4}
Depth I.(G.)	-	1.91×10^{-1}	1.71×10^{-1}	1.62×10^{-1}	1.55×10^{-1}
Residual	2.25×10^{-1}	1.26×10^{-1}	1.57×10^{-1}	1.70×10^{-1}	1.76×10^{-1}
ICC	-	0.696	0.541	0.474	0.439
R^2 m/c & a	0.30/0.30	0.29/0.79	0.28/0.67	0.27/0.61	0.27/0.59
$pK_{sp^{\circ}-dol}$ 25 °C	-17.24	-17.24	-17.24	-17.25	-17.25
CI 25°C l/u (dif)	-17.23/-17.25 (0.02)	-16.99/-17.48 (0.50)	-16.94/-17.56 (0.62)	-16.91/-17.59 (0.67)	-16.90/-17.59 (0.68)
$pK_{sp^{\circ}-dol}$ 200 °C	-23.42	-23.41	-23.40	-23.39	-23.39
CI 200°C l/u (dif)	-23.37/-23.48 (0.11)	-23.16/-23.67 (0.51)	-23.08/-23.71 (0.63)	-23.05/-23.73 (0.68)	-23.03/-23.74 (0.71)
AIC	-1455.3	-2754.0	-2845.5	-3034.2	-3085.8

J1. Model of SUPCRT92-Filtered PWGD dataset. J2. Model of SUPCRT92-Filtered PWGD utilizing only the depth random effect. No clustering of samples into defined depth ranges. J3. Model of SUPCRT92-Filtered PWGD utilizing only the depth random effect. Samples are clustered into 10m interval depth groups. J4. Model of SUPCRT92-Filtered PWGD utilizing only the depth random effect. Samples are clustered are clustered into 50m interval depth groups. J5. Model of SUPCRT92-Filtered PWGD utilizing only the depth random effect. Samples are clustered into 100m interval depth groups. J6. Model of SUPCRT92-Filtered PWGD utilizing only the depth random effect. Samples are clustered into 200m interval depth groups.

Model	J6 - 200m (n=3544)	J7 - 300m (n=3296)	J8 - 400m (n=3175)	J9 - 500m (n=3040)
Model Type	Mixed (1)	Mixed (1)	Mixed (1)	Mixed (1)
Samples	10343	10343	10343	10343
a (SE)	-3.78 (6.64×10^{-1})	-3.64 (6.76×10^{-1})	-3.70 (6.80×10^{-1})	-3.61 (6.81×10^{-1})
t/p	-5.69, 1.35×10^{-8}	-5.38, 7.87×10^{-8}	-5.44, 5.66×10^{-8}	-5.30, 1.21×10^{-7}
b (SE)	8.81×10^{-3} (9.82×10^{-4})	8.57×10^{-3} (1.00×10^{-3})	8.66×10^{-3} (1.00×10^{-3})	8.53×10^{-3} (1.00×10^{-3})
t/p	8.98, $<2.22\times10^{-16}$	8.58, $<2.22\times10^{-16}$	8.62, $<2.22\times10^{-16}$	8.47, $<2.22\times10^{-16}$
c (SE)	4.29×10^{2} (1.12×10^{2})	4.09×10^{2} (1.14×10^{2})	4.19×10^{2} (1.14×10^{2})	4.05×10^{2} (1.15×10^{2})
t/p	3.84, 1.23×10^{-4}	3.59, 3.34×10^{-4}	3.66, 2.51×10^{-4}	3.53, 4.22×10^{-4}
Depth I.(G.)	1.52×10^{-1}	1.51×10^{-1}	1.49×10^{-1}	1.47×10^{-1}
Residual	1.78×10^{-1}	1.80×10^{-1}	1.82×10^{-1}	1.83×10^{-1}
ICC	0.418	0.411	0.400	0.393
R^2 m/c & a	0.27/0.57	0.26/0.57	0.26/0.56	0.26/0.55
$pK_{sp^{\circ}-dol}$ 25 °C	-17.25	-17.25	-17.25	-17.25
CI 25°C l/u (dif)	-16.89/-17.60 (0.70)	-16.90/-17.61 (0.71)	-16.89/-17.61 (0.72)	-16.89/-17.61 (0.72)
$pK_{sp^{\circ}-dol}$ 200 °C	-23.40	-23.38	-23.38	-23.38
CI 200°C l/u (dif)	-23.04/-23.75 (0.72)	-23.02/-23.74 (0.72)	-23.02/-23.74 (0.73)	-23.01/-23.75 (0.74)
AIC	-3137.9	-3196.5	-3147.0	-3152.6

J7. Model of SUPCRT92-Filtered PWGD dataset. Samples are clustered into 300m interval depth groups. J8. Model of SUPCRT92-Filtered PWGD dataset. Samples are clustered into 400m interval depth groups. J9. Model of SUPCRT92-Filtered PWGD dataset. Samples are clustered into 500m interval depth groups.

Model	J10	J11	J12	J13	J14
Model Type	Mixed (1)	Mixed (1)	Mixed (1)	Mixed (1)	Mixed (1)
Samples	10343	10343	10343	10343	10343
a (SE)	-2.98 (6.16×10^{-1})	-2.88 (5.07×10^{-1})	-1.89 (5.37×10^{-1})	-3.88 (4.89×10^{-1})	-3.68 (4.87×10^{-1})
t/p	-4.83, 1.43×10^{-6}	-5.68, 1.42×10^{-8}	-3.52, 4.32×10^{-4}	-7.94, 2.18×10^{-15}	-7.55, 4.82×10^{-14}
b (SE)	7.57×10^{-3} (9.14×10^{-4})	7.52×10^{-3} (7.49×10^{-4})	5.71×10^{-3} (7.95×10^{-4})	9.03×10^{-3} (7.21×10^{-4})	8.77×10^{-3} (7.21×10^{-4})
t/p	8.29, $<2.22\times10^{-16}$	1.00×10^{1}, $<2.22\times10^{-16}$	7.18, 7.40×10^{-13}	1.25×10^{1}, $<2.22\times10^{-16}$	1.22×10^{1}, $<2.22\times10^{-16}$
c (SE)	2.98×10^{2} (1.04×10^{2})	2.79×10^{2} (8.54×10^{1})	1.47×10^{2} (9.04×10^{1})	4.36×10^{2} (8.23×10^{1})	4.00×10^{2} (8.21×10^{1})
t/p	2.88, 4.02×10^{-3}	3.27, 1.09×10^{-3}	1.62, 1.04×10^{-1}	5.29, 1.23×10^{-7}	4.88, 1.09×10^{-6}
Basin I.(G.)	-	6.99×10^{-1}	-	-	-
Field I.(G.)	1.27×10^{-1}	-	-	-	-
Formation I.(G.)	-	-	1.29×10^{-1}	-	-
Lithology I.(G.)	-	-	-	3.48×10^{-2}	-
Series I.(G.)	-	-	-	-	-
Period I.(G.)	-	-	-	-	2.25×10^{-2}
Residual	1.95×10^{-1}	2.20×10^{-1}	2.03×10^{-1}	2.24×10^{-1}	2.25×10^{-1}
ICC	0.297	0.091	0.288	0.024	0.010
R^2 m/c & a	0.26/0.48	0.27/0.34	0.21/0.44	0.29/0.31	0.30/0.31
$pK_{sp^{\circ}-dol}$ 25 °C	-17.24	-17.26	-17.26	-17.23	-17.24
CI 25°C l/u (dif)	-16.86/-17.62 (0.77)	-16.83/-17.69 (0.87)	-16.86/-17.66 (0.80)	-16.79/-17.68 (0.89)	-16.79/-17.68 (0.89)
$pK_{sp^{\circ}-dol}$ 200 °C	-23.34	-23.37	-23.22	-23.41	-23.41
CI 200°C l/u (dif)	-22.95/-23.72 (0.77)	-22.94/-23.81 (0.87)	-22.82/-23.61 (0.79)	-22.97/-23.86 (0.89)	-22.97/-23.86 (0.89)
AIC	-2828.3	-1815.0	-2639.5	-1524.2	-1481.8

J10. Model of SUPCRT92-Filtered PWGD dataset. Only the field random effect is used. J11. Model of SUPCRT92-Filtered PWGD dataset. Only the basin random effect is used. J12. Model of SUPCRT92-Filtered PWGD dataset. Only the formation random effect is used J13. Model of SUPCRT92-Filtered PWGD dataset. Only the lithology random effect is used. J14. Model of SUPCRT92-Filtered PWGD dataset. Only the time-period random effect is used.

Model	J15	J16	J17	J18	J19
Model Type	Mixed (1)	Mixed (2)	Mixed (3)	Mixed (4)	Mixed (5)
Samples	10343	10343	10343	10343	10343
a (SE)	-3.59 (4.91×10^{-1})	-3.33 (6.88×10^{-1})	-2.31 (6.97×10^{-1})	-1.86 (7.19×10^{-1})	-1.89 (7.19×10^{-1})
t/p	-7.31, 2.87×10^{-13}	-4.85, 1.29×10^{-6}	-3.31, 9.49×10^{-4}	-2.59, 9.74×10^{-3}	-2.62, 8.79×10^{-3}
b (SE)	8.65×10^{-3} (7.25×10^{-4})	8.11×10^{-3} (1.02×10^{-3})	6.42×10^{-3} (1.03×10^{-3})	5.77×10^{-3} (1.06×10^{-3})	5.81×10^{-3} (1.06×10^{-3})
t/p	1.92×10^{1}, $<2.22\times10^{-16}$	7.97, 2.20×10^{-15}	6.21, 5.88×10^{-10}	5.43, 6.09×10^{-8}	5.47, 4.93×10^{-8}
c (SE)	3.85×10^{2} (8.27×10^{2})	3.59×10^{2} (1.16×10^{2})	2.07×10^{2} (1.17×10^{2})	1.33×10^{2} (1.21×10^{2})	1.37×10^{2} (1.21×10^{2})
t/p	4.65, 3.29×10^{-6}	3.10, 1.94×10^{-3}	1.76, 7.78×10^{-2}	1.10, 2.73×10^{-1}	1.13, 2.57×10^{-1}
Depth I.(G.)	-	1.21×10^{-1}	1.09×10^{-1}	1.09×10^{-1}	1.09×10^{-1}
Field I.(G.)	-	8.86×10^{-2}	6.90×10^{-2}	6.98×10^{-2}	6.97×10^{-2}
Formation I.(G.)	-	-	9.12×10^{-2}	7.70×10^{-2}	7.68×10^{-2}
Basin I.(G.)	-	-	-	6.14×10^{-2}	6.17×10^{-2}
Lithology I.(G.)	-	-	-	-	8.53×10^{-3}
Series I.(G.)	3.39×10^{-2}	-	-	-	-
Period I.(G.)	-	-	-	-	-
Residual	2.24×10^{-1}	1.80×10^{-1}	1.77×10^{-1}	1.77×10^{-1}	1.77×10^{-1}
ICC	0.022	0.409	0.445	0.459	0.459
R^2 m/c & a	0.30/0.31	0.26/0.56	0.23/0.57	0.22/0.58	0.22/0.58
$pK_{sp°—dol}$ 25 °C	-17.24	-17.25	-17.26	-17.27	-17.27
CI 25°C l/u (dif)	-16.80/-17.68 (0.87)	-16.89/-17.60 (0.71)	-16.92/-17.60 (0.68)	-16.92/-17.62 (0.69)	-16.92/-17.61 (0.70)
$pK_{sp°—dol}$ 200 °C	-23.41	-23.36	-23.26	-23.25	-23.25
CI 200°C l/u (dif)	-22.97/-23.86 (0.89)	-22.99/23.72 (0.72)	-22.91/-23.63 (0.72)	-22.90/-23.60 (0.71)	-22.89/-23.61 (0.72)
AIC	-1501.2	-3261.5	-3533.8	-3590.9	-3589.7

J15. Model of SUPCRT92-Filtered PWGD dataset. Only the time-series random effect is used. J16. Model of SUPCRT92-Filtered PWGD dataset. The depth (300m interval) and the field random effects are used. J17. Model of SUPCRT92-Filtered PWGD dataset. The depth (300m interval), field, and formation random effects are used. J18. Model of SUPCRT92-Filtered PWGD dataset. The depth (300m interval), field, formation, and basin random effects are used. J19. Model of SUPCRT92-Filtered PWGD dataset. The depth (300m interval), field, formation, basin and lithology random effects are used.

Model	J20	J21	J22	J23 - $pK_{sp^{\circ}-dol}$	J24 - $pK_{sp^{\circ}-dol}$
Model Type	Mixed (6)	Mixed (7)	Mixed (7)	Mixed (7)	Mixed (7)
Samples	10343	10343	10343	10343	10343
a (SE)	-1.94 (7.21×10^{-1})	-1.90790 (7.21×10^{-1})	-1.86 (7.21×10^{-1})	1.47545×10^{1} (7.22×10^{-1})	1.93×10^{1} (5.67×10^{-2})
t/p	-2.70, 7.07×10^{-3}	-2.65, 8.16×10^{-3}	-2.58, 9.84×10^{-3}	2.04×10^{1}, $<2.22\times10^{-16}$	339.6, $<2.22\times10^{-16}$
b (SE)	5.89×10^{-3} (1.06×10^{-3})	5.84297×10^{-3}(1.07×10^{-3})	5.85×10^{-3} (1.07×10^{-3})	-6.24959×10^{-2} (1.07×10^{-4})	-6.919×10^{-2} (fixed value)
t/p	5.53, 3.42×10^{-8}	5.49, 4.44×10^{-8}	5.49, 4.32×10^{-8}	-5.86×10^{1}, $<2.22\times10^{-16}$	-
c (SE)	1.47×10^{2} (1.21×10^{2})	1.40778×10^{2} (1.21×10^{2})	1.31×10^{2} (1.21×10^{2})	-3.99350×10^{3} (1.22×10^{2})	-4.75×10^{3} (1.75×10^{1})
t/p	1.21, 2.26×10^{-1}	1.16, 2.46×10^{-1}	1.08, 2.82×10^{-1}	-3.29×10^{1}, $<2.22\times10^{-16}$	270.7, $<2.22\times10^{-16}$
Ionic strength (SE)	-	-	-7.14×10^{-3} (1.49×10^{-3})	-	-
t/p	-	-	-4.79, 1.68×10^{-6}	-	-
Depth I.(G.)	1.09×10^{-1}	1.09×10^{-1}	1.10×10^{-1}	1.10×10^{-1}	1.12×10^{-1}
Basin I.(G.)	6.30×10^{-2}	6.35×10^{-2}	6.40×10^{-2}	6.47×10^{-2}	6.22×10^{-2}
Field I.(G.)	6.99×10^{-2}	7.01×10^{-2}	6.86×10^{-2}	6.94×10^{-2}	6.90×10^{-2}
Formation I.(G.)	7.65×10^{-2}	7.66×10^{-2}	7.67×10^{-2}	7.70×10^{-2}	7.66×10^{-2}
Lithology I.(G.)	8.86×10^{-3}	8.05×10^{-3}	9.80×10^{-3}	7.77×10^{-3}	9.33×10^{-3}
Series I.(G.)	-	1.70×10^{-2}	1.74×10^{-2}	1.70×10^{-2}	1.66×10^{-2}
Period I.(G.)	1.80×10^{-2}	1.38×10^{-2}	1.44×10^{-2}	1.36×10^{-2}	1.35×10^{-2}
Residual	1.77×10^{-1}	1.76×10^{-1}	1.76×10^{-1}	1.76×10^{-1}	1.76×10^{-1}
ICC	0.464	0.466	0.469	0.469	0.467
R^2 m/c & a	0.22/0.58	0.22/0.58	0.21/0.58	0.91/0.95	0.96/0.98
$pK_{sp^{\circ}-dol}$ 25°C	-17.27	-17.27	-17.28	-17.27	-17.28
CI 25°C l/u (dif)	-16.92/-17.61 (0.69)	-16.92/-17.62 (0.70)	-16.93/-17.62 (0.69)	-16.93/-17.62 (0.69)	(0.69)
$pK_{sp^{\circ}-dol}$ 200°C	-23.25	-23.25	-23.28	-23.26	-23.50
CI 200°C l/u (dif)	-22.90/-23.61 (0.72)	-22.89/-23.61 (0.72)	-22.92/-23.63 (0.71)	-22.90/-23.61 (0.71)	(0.69)
AIC	-3593.6	-3595.4	-3599.8	-3587.1	-3562.0

J20. Model of SUPCRT92-Filtered PWGD dataset. The depth (300m interval), field, formation, basin, lithology and time-period random effects are used. J21. Model of SUPCRT92-Filtered PWGD dataset. The depth (300m interval), field, formation, basin, lithology, time-period and time-series random effects are used. This is the reference model for the relationship between $\log_{10}({}^{a}Ca^{2+}/{}^{a}Mg^{2+})$-temperature for the PWGD. J22. Model of SUPCRT92-Filtered PWGD dataset with ionic strength included as a fixed effect. The same 7 random effects used in model J21 used here. J23. Model of $pK_{sp^{\circ}-dol}$ values calculated for SUPCRT92-Filtered PWGD dataset. Statistical goodness of fit functions (AIC, R^2) and t/p values are thought to be somewhat spurious due to the pre-modelling conversion to $pK_{sp^{\circ}-dol}$. The same 7 random effects used in model J22 used here. J24. Model of $pK_{sp^{\circ}-dol}$ values calculated for SUPCRT92-Filtered PWGD dataset where the b term is fixed to -0.06919. The same 7 random effects used in model J22 used here. There appears to be an unresolvable bug in how R calculates confidence intervals for offset models, with the width of the interval which appear to be

reliable but not the absolute values (which are significantly incorrect).

Model	K1	K2 - $pK_{sp°—dol}$	L1	M1	N1
Model Type	Mixed (6)	Mixed (6)	Linear	Linear	Linear
Samples	11480	11480	42	36	28
a (SE)	8.31×10^{-1} (9.07×10^{-1})	1.19×10^{1} (9.09×10^{-1})	-1.01 (7.07×10^{-1})	-1.22 (3.21×10^{-1})	-1.74×10^{1} (5.25)
t/p	9.17×10^{-1}, 3.59×10^{-1}	1.31×10^{1}, $<2.22\times10^{-16}$	-1.42, 1.63×10^{-1}	-3.79, 5.93×10^{-4}	3.33, 2.70×10^{-3}
b (SE)	1.18×10^{-3} (1.33×10^{-3})	-5.76×10^{-2} (1.33×10^{-3})	4.13×10^{-3} (2.28×10^{-3})	4.82×10^{-3} (1.03×10^{-3})	-6.88×10^{-2} (6.36×10^{-3})
t/p	8.88×10^{-1}, 3.75×10^{-1}	-4.34×10^{1}, $<2.22\times10^{-16}$	1.81, 7.73×10^{-2}	4.70, 4.23×10^{-5}	-1.08×10^{1}, 6.37×10^{-11}
c (SE)	-2.58×10^{2} (1.54×10^{2})	-3.58×10^{3} (1.54×10^{2})	-	-	-4.22×10^{3} (1.07×10^{3})
t/p	-1.68, 9.34×10^{-2}	-2.32×10^{1}, $<2.22\times10^{-16}$	-	-	-3.95, 5.66×10^{-4}
Depth I.(G.)	1.38×10^{-1}	1.39×10^{-1}	-	-	-
Field I.(G.)	1.30×10^{-1}	1.30×10^{-1}	-	-	-
Formation I.(G.)	1.00×10^{-1}	1.00×10^{-1}	-	-	-
Basin I.(G.)	8.29×10^{-2}	8.54×10^{-2}	-	-	-
Lithology I.(G.)	2.43×10^{-2}	2.39×10^{-2}	-	-	-
Period I.(G.)	1.30×10^{-1}	1.28×10^{-2}	-	-	-
Residual	2.56×10^{-1}	2.56×10^{-1}	1.65×10^{-1}	5.78×10^{-2}	0.29
ICC	0.449	0.452	-	-	-
R^2 m/c & a	0.08/0.49	0.84/0.91	0.05	0.38	0.99
$pK_{sp°—dol}$ 25°C	-17.28	-17.28	-17.19	-17.17	-17.18
CI 25°C l/u (dif)	-16.77/-17.78 (1.00)	-16.78/-17.79 (1.00)	-17.11/-17.26 (0.15)	-17.14/-17.22 (0.07)	-16.66/-17.71 (0.53)
$pK_{sp°—dol}$ 200 °C	-22.94	-22.94	-23.05	-23.16	-24.00
CI 200°C l/u (dif)	-22.43/-23.47 (1.04)	-22.42/-23.47 (1.05)	-22.30/-23.80 (0.72)	-22.83/-23.50 (-0.67)	-23.85/-24.15 (0.15)
AIC	-	-	-	-	-

K1. Model of PWGD database not filtered using the SUPCRT92-Filter. The model (and K2) are unable to reliably calculate the time series random effect term so it is omitted. K2. Model of $pK_{sp°—dol}$ values for the PWGD database with values not filtered using the SUPCRT92-Filter. L1. Model of Yarmouk gorge samples from Möller and De Lucia (2020) dataset; samples are taken from Siebert and others (2014) and Siebert and others (in prep). The p-value of this model is 7.73×10^{-2} (identical also to p value on the b-term). We do not report model p-values as they are only output for linear models. The p-values given(reported t/p) are those that describe the significance of model coefficients. M1. Model of Yarmouk gorge samples from Möller and De Lucia (2020) without samples <25°C. The p-value for this model is 4.23×10^{-5} (again identical to the to p value on the b-term). N1. Reanalysis of the Bénézeth and others (2018) dataset using activities calculated by Bénézeth and others (2018).